Mon. Not. R. Astron. Soc. **000**, 1–34 (2013) Printed 30 May 2013 (MN LATEX style file v2.2)

SPIDER VIII – Constraints on the Stellar Initial Mass Function of Early-type Galaxies from a Variety of Spectral Features.

F. La Barbera[1⋆], I. Ferreras[2⋆], A. Vazdekis[3,4], I.G. de la Rosa[3,4], R.R. de Carvalho[5], M. Trevisan[5], J. Falcón-Barroso[3,4], E. Ricciardelli[6]
[1] *INAF – Osservatorio Astronomico di Capodimonte, Napoli, Italy*
[2] *MSSL, University College London, Holmbury St Mary, Dorking, Surrey RH5 6NT, UK*
[3] *Instituto de Astrofísica de Canarias (IAC), E-38200 La Laguna, Tenerife, Spain*
[4] *Departamento de Astrofísica, Universidad de La Laguna, E-38205, Tenerife, Spain*
[5] *Instituto Nacional de Pesquisas Espaciais/MCT, S. J. dos Campos, Brazil*
[6] *Departament d'Astronomia i Astrofisica, Universitat de Valencia, C/Dr Moliner 50, E-46100, Burjassot, Valencia, Spain*

Accepted 2013 May 27. Received 2013 May 27; in original form 2013 February 27

ABSTRACT

We perform a spectroscopic study to constrain the stellar Initial Mass Function (IMF) by using a large sample of 24,781 early-type galaxies from the SDSS-based SPIDER survey. Clear evidence is found of a trend between IMF and central velocity dispersion (σ_0), evolving from a standard Kroupa/Chabrier IMF at $\sigma_0 \sim 100\,\mathrm{km\,s^{-1}}$ towards a more bottom-heavy IMF with increasing σ_0, becoming steeper than the Salpeter function at $\sigma_0 \gtrsim 220\,\mathrm{km\,s^{-1}}$. We analyze a variety of spectral indices, combining gravity-sensitive features, with age- and metallicity-sensitive indices, and we also consider the effect of non solar abundance variations. The indices, corrected to solar scale by means of semi-empirical correlations, are fitted simultaneously with the (nearly solar-scaled) extended MILES (MIUSCAT) stellar population models. Similar conclusions are reached when analyzing the spectra with a hybrid approach, combining constraints from direct spectral fitting in the optical with those from IMF-sensitive indices. Our analysis suggests that σ_0, rather than [α/Fe], drives the variation of the IMF. Although our analysis cannot discriminate between a single power law (unimodal) IMF and a low-mass ($\lesssim 0.5\,\mathrm{M_\odot}$) tapered (bimodal) IMF, robust constraints can be inferred for the fraction in low-mass stars at birth. This fraction (by mass) is found to increase from $\sim 20\%$ at $\sigma_0 \sim 100\,\mathrm{km\,s^{-1}}$, up to $\sim 80\%$ at $\sigma_0 \sim 300\,\mathrm{km\,s^{-1}}$. However, additional constraints can be provided with stellar mass-to-light (M/L) ratios: unimodal models predict M/L significantly larger than dynamical M/L, across the whole σ_0 range, whereas a bimodal IMF is compatible. Our results are robust against individual abundance variations. No significant variation is found in Na and Ca in addition to the expected change from the correlation between [α/Fe] and σ_0.

Key words: galaxies: stellar content – galaxies: fundamental parameters – galaxies: formation

1 INTRODUCTION

The formation of stars in a gas cloud is a problem of extraordinary physical complexity, remaining one of the major open problems in modern astrophysics. A way to constrain this fundamental issue is to examine the stellar Initial Mass Function (IMF), i.e. the distribution of the masses of stars at birth. The IMF has critical implications in the framework of galaxy formation and evolution, as it sets the overall mass-scale of galactic systems, controls the intensity of the stellar feedback processes and drives the chemical enrichment abundance patterns.

To date, the IMF can only be directly constrained from star number counts in the disk of the Galaxy. Current observations are consistent with a universal Kroupa/Chabrier-type IMF, i.e. a power-law behaviour at high mass ($> 1\,\mathrm{M_\odot}$)

⋆ E-mail: labarber@na.astro.it (FLB); i.ferreras@ucl.ac.uk (IF)

with a turn-off at lower masses (Kroupa 2001; Chabrier 2003), although with a significant uncertainty in the region at masses around a few tenths of $M_\odot$ (see Bastian et al. 2010, and references therein). However, the low-mass portion of the IMF is extremely important because the mass fraction in stars below $1\,M_\odot$ varies from $\sim 1/3$ for a Kroupa IMF up to $\sim 2/3$ for a Salpeter (1955) IMF, i.e. a large mass fraction of a stellar population is indeed expected in the form of low-mass stars.

An indirect method to study the IMF involves the use of dynamical modelling techniques to constrain the total and stellar mass-to-light ratios of a stellar system. These techniques have been applied to star clusters, favouring a Kroupa-like IMF (see, e.g., Bastian et al 2006). In early-type galaxies (hereafter ETGs), detailed dynamical modelling of the kinematic properties in a nearby sample revealed a systematic increase in the stellar M/L with galaxy mass (Cappellari et al. 2012a), a result confirmed over a 260-strong sample of ETGs from the ATLAS^{3D} survey (Cappellari et al. 2012c), where the trend is expected to evolve from a Kroupa IMF at low velocity dispersion ($\sigma \sim 80\,\mathrm{km\,s^{-1}}$) towards a Salpeter function at $\sigma \sim 260\,\mathrm{km\,s^{-1}}$. Independent dynamical studies have arrived at similar conclusions (see, e.g., Thomas et al. 2011; Wegner et al. 2012; Cappellari et al. 2012a; Dutton, Mendel & Simard 2012; Tortora et al. 2013). Strong gravitational lensing over galaxy scales can also be exploited to derive stellar M/L especially when the Einstein radius only extends over the central regions, where dark matter does not complicate the issue of transforming total into stellar M/L. Although strong lensing studies of low-mass spheroids rejected a Salpeter IMF (Ferreras et al. 2005, 2008, 2010), recent work covering a wider range of galaxy mass hinted at systematic variations towards higher stellar M/L with increasing mass (Auger et al. 2010; Treu et al. 2010; Barnabé et al. 2011). Hence, both lensing and dynamical studies require a scenario consistent with either a bottom- or a top-heavier IMF than Kroupa/Chabrier in massive ETGs. In fact, a stellar population can have large M/L because of a large fraction of either low-mass stars or remnants of massive stars, and neither dynamical nor lensing modelling is capable of distinguishing between the two (Cappellari et al. 2012a).

A unique opportunity to investigate more directly the IMF is offered by gravity-sensitive features in the integrated light of unresolved stellar populations, as originally proposed by Spinrad (1962). Some of the most discriminant features include the Na I doublet feature at $\lambda\lambda 8183, 8195$ Å (Faber & French 1980; Schiavon et al. 1997b, hereafter NaI8200), the Wing-Ford FeH band (Wing & Ford 1969; Schiavon et al. 1997a) at $9,900$ Å, prominent in the atmospheres of low-mass dwarves, as well as the Ca triplet lines at $\lambda \sim 8600$ Å(hereafter CaT; see, e.g., Diaz, Terlevich, Terlevich 1989; Cenarro et al. 2003), which are strong in giants, while barely detectable in dwarves. Several other features, mostly related to Na, Ca, and TiO lines, have been also identified in the literature, as potentially useful tools to constrain the dwarf/giant ratio (Conroy & van Dokkum 2012a, Spiniello et al. 2012, hereafter STK12, Smith, Lucey & Carter 2012). Another potentially useful tool is the analysis of (optical-NIR) broad-band colours (Vazdekis et al. 1996, 2012; Ricciardelli et al. 2012). In this respect, ETGs offer a unique opportunity to study the IMF, as they host homogeneous, old, stellar populations, with little amount of dust, allowing for a clean analysis of their stellar content. Nevertheless, this kind of analysis is far from being trivial. All dwarf/giant sensitive features represent a contribution at the level of a few percent to the total galaxy flux, and these features are also sensitive to age, metallicity, as well as abundance ratio of (several) chemical elements. Moreover, NIR features, like NaI8200 and CaT, fall in a spectral region often severely contaminated by sky emission and telluric absorption. These problems have hampered the use of gravity-sensitive features to investigate the IMF for a long time.

The first observational attempts to constrain the giant/dwarf ratio in the IMF were made by Cohen (1978) and Faber & French (1980), towards the centres of M31 and M32, using the NaI8200 feature. Later, Carter et al. (1986) extended the study to a sample of massive ETGs, and found that NaI8200 was enhanced, especially in massive galaxies, with strong radial gradients. These studies concluded in favour of an excess of dwarves (relative to giants) in the galaxy central regions. Opposite conclusions were drawn by Hardy & Couture (1988) and Delisle & Hardy (1992), based on NaI8200A, CaT, and the Wing-Ford band, who explained the radial variation and central strength of these features as a metallicity (rather than IMF) effect. All these early works were in fact plagued by many difficulties, in particular, small sample sizes, low signal-to-noise ratio and resolution of the spectra, or uncertainties in the available stellar population models. The recent availability of dedicated instrumentation and sophisticated reduction techniques has opened up new opportunities to exploit the constraining power of (NIR) IMF-sensitive features, by means of high-quality spectroscopy. Cenarro et al. (2003) proposed a trend towards an excess of low-mass stars in massive galaxies, from a study of the CaT region. More recently, van Dokkum & Conroy (2010, 2011) used the NaI8200A and Wing-Ford band to conclude that the IMF is bottom-heavier than a Kroupa/Chabrier distribution in a sample of eight massive ETGs in the Virgo and Coma clusters. This result has been confirmed, using (theoretical) stellar population models with varying element abundance ratios and a full spectral fitting analysis by Conroy & van Dokkum (2012a), and further extended to a set of 34 ETGs from the SAURON survey (Conroy & van Dokkum 2012b). At the same time, STK12 and Ferreras et al. (2013, hereafter FLD13) have gone beyond a simple test of universality for the IMF, analyzing large samples of ETGs drawn from the Sloan Digital Sky Survey (SDSS), focusing on Na and TiO spectral features. Remarkably, FLD13 relied on completely independent stellar population models with respect to Conroy & van Dokkum (2012a), using the MIUSCAT (Vazdekis et al. 2012; Ricciardelli et al. 2012) spectrally extended version of the stellar population synthesis models MILES (Vazdekis et al. 2010). Although all these studies favour a non-universal IMF, with more massive ETGs harbouring bottom-heavier distributions than Kroupa/Chabrier, the debate lingers on. In fact, a different picture has been proposed whereby the variation of spectral features with galaxy mass in ETGs is driven by a change of single element (mostly Na and Ca) abundance patterns, rather than an IMF variation (see, e.g., Worthey, Ingermann & Serven 2011, and refer-

ences therein). According to this interpretation, for instance, the NaI8200 (CaT) line strength would increase (decrease) with galaxy mass because of an over-(under-)abundance of Na (Ca) relative to Mg in more massive systems. As shown by Conroy & van Dokkum (2012a), a way out to break the degeneracy is by combining spectral features sensitive to IMF with those more sensitive to the abundance of single chemical species. To this effect one has to rely on theoretical models, rather than fully empirical stellar population libraries, to model the impact of variations in both IMF and abundance ratio, over a wide range of wavelength. Therefore, it is important to consider simultaneously a variety of spectral features from different chemical species.

In this paper, we follow this approach. We extend our previous work (FLD13), analyzing stacked spectra of $\sim 24,781$ nearby ($z \sim 0.07$) ETGs with exceptionally high S/N-ratio, spanning a wide range of central velocity dispersion, from 100 to 300 $\mathrm{km\,s^{-1}}$. As in FLD13, we mainly rely on extended MILES (MIUSCAT) state-of-the-art stellar population models for the analysis. The main novelties of the present contribution are the following: (i) we adopt a wide set of spectral indices (with respect to, e.g., STK12 and FLD13), fitting several TiO, Ca, and Na features simultaneously, to constrain the IMF; (ii) we combine age, metallicity, IMF- and abundance-sensitive features in the analysis; (iii) we use a semi-empirical technique to correct spectral indices to solar-scale, hence allowing for a clean comparison to the base (nearly solar-scaled) models and avoiding to rely completely on theoretical models; (iv) we adopt a wide set of fitting techniques, including a pure spectral index fitting approach, and a hybrid approach, where direct spectral fitting is combined to the constraints from IMF-sensitive indices (as in FLD13); (v) we allow for a wide range of star-formation histories, including one- and two-simple stellar populations (hereafter SSP), as well as exponentially declining star-formation models. All results presented in this work point consistently to a steepening of the IMF with velocity dispersion in ETGs.

The layout of the paper is as follows: Sec. 2 describes the sample of ETGs, drawn from the SDSS-based SPIDER survey. Sec. 2.2 details our stacking procedures. The stellar population models used to analyze the stacks are described in Sec. 3. Sec. 4 presents the spectral indices used in this work, showing their sensitivity to age, metallicity, and IMF. In Sec. 5, we explore the correlation of the targeted spectral indices with abundance ratio. The different fitting methods to interpret the spectra are described in Sec. 6, while results from different fits are discussed in Sec. 7. Sec. 8 shows the ability of the best-fit models, with a varying IMF, to match independent constraints, i.e. mass-to-light ratios and optical-NIR colours. A summary is given in Sec. 9.

2 DATA

2.1 Sample

The SPIDER[1] sample consists of 39,993 nearby (0.05<z<0.095) ETGs, selected from Data Release 6 of the Sloan Digital Sky Survey (SDSS-DR6; Adelman-McCarthy et al. 2008), as described in La Barbera et al. (2010a, hereafter Paper I). Galaxies are selected to have r-band Petrosian magnitude brighter than -20, corresponding to an absolute B-band magnitude of -19, where the separation between the two families of *bright* and *ordinary* ellipticals occurs (Capaccioli, Caon & D'Onofrio 1992; Graham & Guzmán 2003; Trevisan et al. 2012). The sample covers two orders of magnitude in dynamical mass, from 2×10^{10} to $10^{12} \mathrm{M}_{\odot}$ (de la Rosa et al. 2012). Following Bernardi et al. (2003b), we have defined ETGs as bulge-dominated systems (i.e. SDSS attribute $fracDev_r > 0.8$, where $fracDev_r$ measures the fraction of galaxy light better fitted by a de Vaucouleurs, rather than an exponential, law), featuring passive spectra within the SDSS fibres (SDSS attribute $eClass < 0$, where $eClass$ indicates the spectral type of a galaxy based on a principal component analysis). All galaxies have spectroscopy as well as central velocity dispersions, σ_0, available from SDSS, and we select those with no spectroscopic warning on (i.e. SDSS $zWarning$ attribute set to zero). The spectra, ranging from 3800 to 9200 Å, are retrieved from SDSS-DR7 (Abazajian et al. 2009), de-redshifted to a common rest-frame and corrected for foreground Galactic extinction (see Paper I). The resulting restframe spectral range varies from 3620–8760 Å, at lowest redshift ($z = 0.05$), to 3470–8400 Å at the upper redshift limit of the sample ($z = 0.095$). This spectral coverage gives us the opportunity to study several IMF-sensitive spectral features in ETGs (see Sec. 4), like the Na doublet at $\lambda \sim 8190$ Å (Schiavon et al. 1997a, hereafter Na8190), and the Calcium triplet (CaT) at $\lambda \sim 8600$ Å (see Cenarro et al. 2001 and references therein). Also, the superb quality of SDSS spectra, with a flux calibration accuracy at the 1% level [2], is suitable to detect the expected variations – at the level of a few percent – from a varying IMF. We come back to this point at the end of Sec. 2.2.

For the present study, we select the subsample of 38,447 ETGs with $\sigma_0 \geqslant 100\,\mathrm{km\,s^{-1}}$, as the SPIDER sample becomes significantly incomplete below this limit (see La Barbera et al. 2010b). Following our previous work (Ferreras et al. 2013, hereafter FLD13), we further limit the analysis to objects ($N_{ETGs} = 33,095$) with low internal extinction, i.e. a colour excess $E(B-V) < 0.1$ mag [3]. The $E(B-V)$ is measured by fitting the SDSS spectrum of each ETG with the spectral fitting code `STARLIGHT` (Cid Fernandes et al. 2005), assuming a Cardelli, Clayton & Mathis (1989) extinction law (see Swindle et al. 2011, hereafter Paper V, for details). Each spectrum is fitted in the spectral range of 3900 to

[1] Spheroids Panchromatic Investigation in Different Environmental Regions (La Barbera et al. 2010a)

[2] Adelman-McCarthy et al. (2008) tested the spectrophotometric accuracy of SDSS data by estimating the relative difference between observed and model spectra of white dwarfs. The difference is smaller than $\sim 1\%$ from ~ 3800 to 8000 Å, except for regions possibly affected by interstellar absorption.

[3] We note that relaxing the threshold in colour excess does not affect our results. For instance, for $E(B-V) < 0.2$, the number of objects in each σ_0 bin changes by a few percent. Since we median-combine the spectra in each bin, the impact of this variation on line strengths is completely negligible (e.g. the $\mathrm{Na8190_{SDSS}}$ equivalent width changes by less than 0.01 Å in all bins).

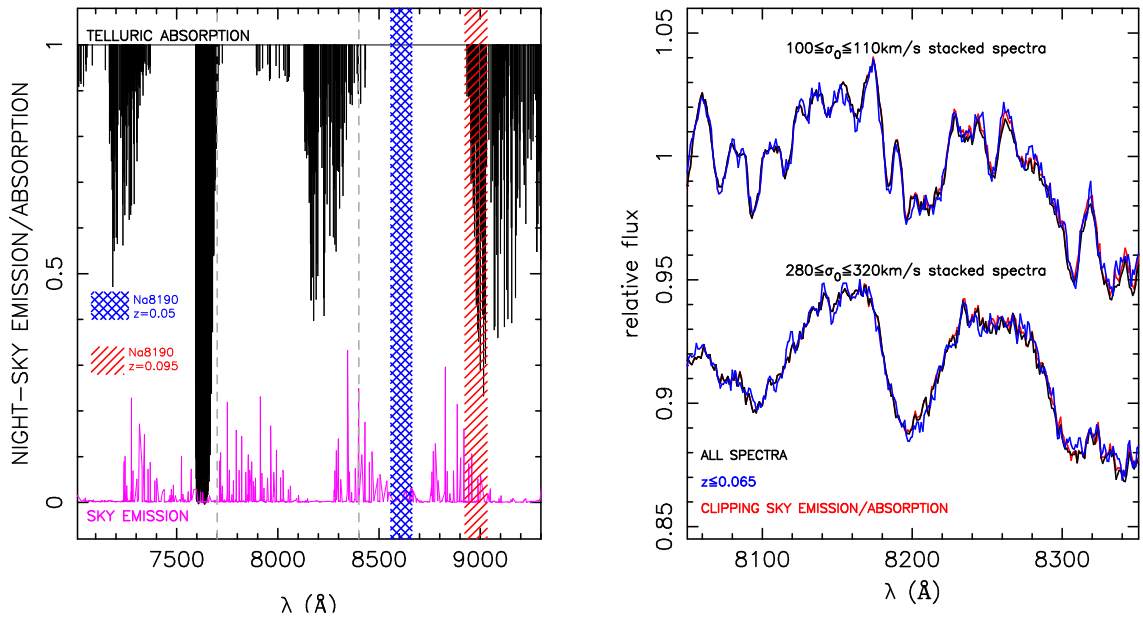

Figure 1. Left: telluric (black) and emission (red) lines of the night-sky are plotted in the wavelength range from ~ 7000 to ~ 9300 Å. The blue and red shaded regions mark the observed spectral window of $\mathrm{Na8190_{SDSS}}$ for the lowest ($z \sim 0.05$) and highest ($z \sim 0.095$) redshift limits of our sample. Notice that at $z \sim 0.05$, the $\mathrm{Na8190_{SDSS}}$ is unaffected by sky contamination. Right: stacked spectra with $\sigma \sim 100$ km s^{-1} (upper curves) and $\sigma \sim 300$ (lower curves; as labelled) are plotted over a 300 Å width region, centered on the $\mathrm{Na8190_{SDSS}}$ feature. All spectra have been normalized by the median flux in the given spectral region. The high-σ_0 stacks have been arbitrarily shifted downwards (by -0.085) for displaying purposes. Different colours correspond to the cases where all (black), only $z \leqslant 0.065$ (blue) spectra are stacked, and the case where sky lines are clipped out of the stacking procedure (red).

7350 Å, with three different sets of simple stellar population (SSP) models, namely, Bruzual & Charlot (2003, BC03), updated Charlot & Bruzual (often refereed to as CB07), and MILES models (Vazdekis et al. 2010, MI10). Each set of models spans a wide range of ages and metallicities (see Paper V for details). The IMFs used are Scalo (BC03), Chabrier (CB07), and Kroupa (MI10). We estimate $E(B-V)$ by averaging output values from the three `STARLIGHT` runs [4]. Notice that this procedure is aimed at removing objects with significant internal extinction from the analysis, while not accounting for possible IMF variations within the sample (i.e. the hypothesis we want to test).

Finally, we restrict the sample to spectra with the highest signal-to-noise (S/N) ratio (see Sec 2.2), resulting in a dataset comprising 24,781 galaxies (i.e. 62% of the original SPIDER catalogue). In addition, for the analysis of the CaT index the sample is further reduced to 3,877 ETGs as we need to exclude galaxies with redshift $z > 0.06$, where the index falls close to the red limit of the SDSS spectra.

2.2 Stacked spectra

Dwarf (relative to giant) stars contribute only up to a few percent to the integrated light of galaxies. Hence, constraining the stellar IMF from gravity-sensitive features requires spectra with exquisite signal-to-noise ratio, typically a few hundreds or more (Conroy & van Dokkum 2012a, hereafter CvD12a). Unfortunately, single SDSS spectra usually do not have such high S/N. For the SPIDER sample, the average S/N over the Na8190 passband (8180 − 8200 Å) amounts to ~ 15 (hereafter quoted per Å), ranging from ~ 12 at $\sigma_0 \sim 100$ km s^{-1} to ~ 25 at $\sigma_0 \sim 300$ km s^{-1}. In order to test for variations of the IMF, we rely on stacked spectra.

As described in FLD13, we have assembled 18 stacked spectra in narrow bins of σ_0, over the available range of 100 to 320 km s^{-1}(see Sec. 2.1). The bins have a width of 10 km s^{-1}, except for the last two bins, where, because of the smaller number of galaxies, we adopt the range [260,280], and [280,320] km s^{-1}, respectively. We bin the sample according to σ_0, because the underlying stellar populations of ETGs are known to correlate strongly with velocity dispersion (Bernardi et al. 2005). For each σ_0 bin, we median stack the available spectra, considering only pixels with no SDSS flag raised[5]. In order to avoid possible biases related to differences in S/N within the σ_0 bins, we exclude spectra in the lowest quartile of the S/N distribution in each bin, resulting in a total number of 24,781 ETGs used to create the stacks. Moreover, in the spectral region of CaT ($\lambda > 8470$ Å), we exclude spectra of galaxies at redshift $z > 0.06$, for which the CaT feature is redshifted beyond the SDSS upper spectral limit of ~ 9200 Å. This selection leads to a smaller, but still significant, sample of 3,877 ETGs used for the stacking at $\lambda > 8470$ Å. Notice that excluding spectra at $z > 0.06$ over the entire available spectral range does not change significantly the other relevant IMF-sensitive features explored in

[4] Runs with different models provide fairly consistent extinction estimates. The mean difference of $E(B-V)$ amounts to about -0.03 and -0.035 for BC03-MI10 and CB07-MI10, respectively.

[5] i.e. no bad pixels, flat field issues, etc. For details see `http://www.sdss.org/dr6/dm/flatFiles/spSpec.html`

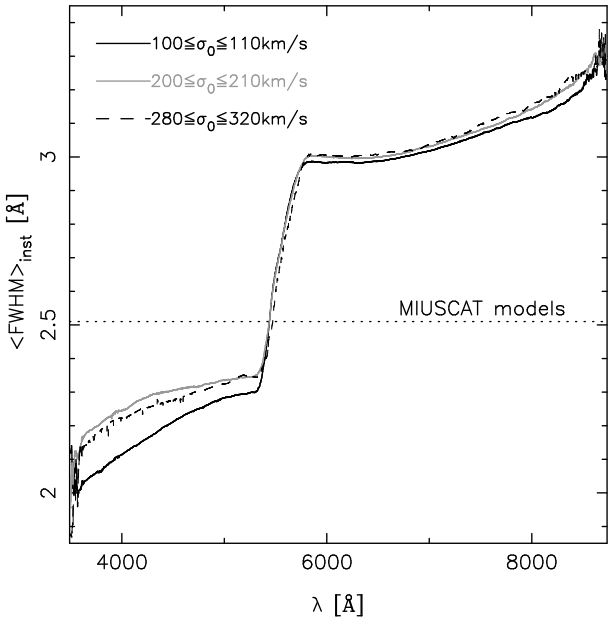

Figure 2. Median resolution of stacked spectra of ETGs, for three bins of σ_0, as labelled. The horizontal dotted line marks the FWHM spectral resolution of the extended MILES (MIUSCAT) models (Falcón-Barroso et al. 2011).

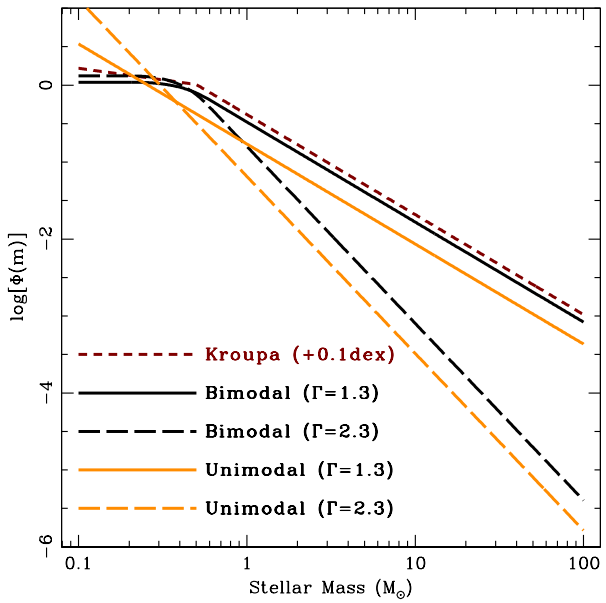

Figure 3. Examples of the unimodal (orange) and bimodal (black) Initial Mass Functions used in this paper. Note the $\Gamma = 1.3$ unimodal case (orange solid line) matches the Salpeter (1955) IMF (defined as a power law with index 1.35), whereas the bimodal case with $\Gamma = 1.3$ (black solid line) maps the Kroupa Universal (2001) IMF (red dashed line), shifted by 0.1 dex in the figure for illustration purposes.

the present work. For instance, averaging over all stacks, the equivalent width of Na8190$_{\rm SDSS}$ would change by less than 1 σ (between the full stacks and those with $z \leqslant 0.06$). This proves that the EWs of CaT can be meaningfully compared to those of spectral features at bluer wavelengths. Relevant properties of each stack are summarized in Tab. 1, where we report the σ_0 range of all bins, the number of ETGs per bin, and the median S/N ratio of stacked spectra, computed within the central passband of five representative spectral indices used in this work (Sec. 4). The stacked spectra feature a remarkably high S/N, larger than a few hundreds throughout the whole spectral range. At $\sigma_0 \sim 150$ km s^{-1}, the S/N of the stacks peaks up to a maximum value of ~ 1800 (~ 800) for the IMF-sensitive TiO2 (Na8190$_{\rm SDSS}$) spectral feature, at $\lambda \sim 6200$ Å (8200 Å). In addition, in Sec. 5, we probe the effect of variations in [α/Fe] on our analysis by further splitting the sample according to [α/Fe], at fixed σ_0, we refer the reader to that section for details.

A major source of concern when studying NIR spectral features (e.g. Na8190$_{\rm SDSS}$ and CaT) is the possible sky contamination of observed spectra, including telluric absorption and emission lines from the night sky. We performed extensive tests, all of them showing that sky contamination does not affect at all our EW estimates. As an example, Fig. 1 (left panel) plots telluric lines (from Hanuschik 2006, unpublished) and sky emission lines in the wavelength region of 7000 to 9200 Å. The red and blue shaded areas mark the observed wavelength range of the Na8190 feature at the lower ($z \sim 0.05$; blue) and upper ($z \sim 0.095$; red) redshift limit of the SPIDER sample. At $z \sim 0.05$, the Na8190 is observed in a region almost unaffected by sky contamination, while at $z \sim 0.095$, the feature overlaps with a strong (H_2O) telluric band (at $\lambda \sim 9000$ Å). The right panel of the same Figure compares the stacked spectra with $\sigma \sim 100$ km s^{-1} and $\sigma \sim 300$ km s^{-1} (black curves), to the case where (i) only ETGs at $z \leqslant 0.065$ are combined, with Na8190 being virtually unaffected by sky contamination, and (ii) a more "aggressive" stacking approach is adopted, where only flux values more than 1Å away from any telluric line and sky emission are combined. The resulting spectra (not used for the present analysis but for sky contamination tests) show an excellent agreement, with differences at the subpercent level. To obtain a more quantitative estimate of how sky contamination may affect our results, we split the sample into low- and high-redshift bins, with $0.05 < z < 0.06$ and $0.085 < z < 0.095$, respectively. We have produced stacked spectra corresponding to these two z intervals for the lowest and highest velocity dispersion bins of our stacks, $100 \leqslant \sigma_0 \leqslant 110$ km s^{-1} and $280 \leqslant \sigma_0 \leqslant 320$ km s^{-1}, respectively. At highest σ_0, the equivalent width [6] of the Na8190$_{\rm SDSS}$ index (see Sec. 4) is 0.51 ± 0.03 Å (0.52 ± 0.04 Å) at lower (higher) redshift, while at lowest σ_0, the corresponding equivalent widths are 0.75 ± 0.04 and 0.78 ± 0.07 at lower and higher redshift. Consistent with FLD13, we conclude that sky contamination does not affect at all the Na8190$_{\rm SDSS}$ feature. The same result holds true for the other relevant features. Regarding the CaT index, one may notice that part of this feature always falls within the H_2O telluric band, at $\lambda \sim 9000$ Å. To test the impact of this on the stacked spectra, we split the CaT sample of ETGs into two redshift bins,

[6] These equivalent widths are computed on the stacks at their nominal resolution, i.e. no correction is applied to bring them to the same σ_0.

with $0.05 < z < 0.055$ and $0.055 < z < 0.060$, respectively. For the $\sigma_0 = 100$–110 and 200–210 km s^{-1} stacks, we find that a difference of CaT equivalent width between the two z intervals of 0.3 ± 0.25 and 0.24 ± 0.21, respectively, i.e. fully consistent with zero within the errors.

In order to compare stellar population models to stacked spectra of ETGs, we characterize how they are affected by the instrumental resolution of the SDSS spectrograph. For each spectrum, the SDSS pipeline provides the instrumental resolution, $FWHM_{inst}$, as a function of observed wavelength. We de-redshifted and stacked the $FWHM_{inst}$ curves in the same way as the galaxy spectra. Fig. 2 compares the resulting stacked resolution, $\langle FWHM \rangle_{inst}$, for three representative σ_0 bins ($\sim$ 100, 200, and 300 km s^{-1}). The variation of $\langle FWHM \rangle_{inst}$ with λ reflects the fact that the SDSS resolution is wavelength dependent (see e.g. Bernardi et al. 2003a), increasing from ~ 2.2 Å for the blue arm of the spectrograph ($\lambda < 6000$ Å) to ~ 3.1 Å for its red arm. Notice that the variation of $\langle FWHM \rangle_{inst}$ among stacked spectra is completely negligible (< 0.2 Å in the blue). For this reason, throughout the present study, we use the average stacked resolution of all spectra in the sample. Notice also that the actual resolution of all stacked spectra analyzed in the present study (given by the SDSS instrumental resolution plus the σ_0 of each stack [7]) is well above that of our reference stellar population models (i.e. the extended MILES models, see below), allowing for an accurate comparison of models and data to be performed.

Finally, we notice that our sample of ETGs is likely contaminated by a small fraction of early spiral systems, i.e., spiral galaxies with a prominent bulge component. As discussed in Paper I, this contamination fraction is about 15%, falling to less than 5% for a high quality subsample defined on the basis of visual image classification. We found that restricting the stacking procedure to this high quality selected sample does not lead to any significant change in the relevant spectral indices. For instance, the Na8190$_{\rm SDSS}$ index changes by less than 0.02 Å for all stacks. This might be expected because we combine the spectra using the median, instead of the average, and confirms that morphological contamination does not affect at all our conclusions.

Table 1. Properties of stacked spectra of ETGs in bins of central velocity dispersion (σ_0).

σ_0 range [km/s] (1)	$N_{\rm ETGs}$ (2)	median signal-to-noise ratio (Å^{-1}) CaHK (3)	Hβ_o (4)	TiO2 (5)	Na8190 (6)	CaT (7)
100–110	1062	134	446	955	401	160
110–120	1864	190	604	1318	561	223
120–130	2452	226	732	1564	690	273
130–140	2604	245	766	1692	772	298
140–150	2662	255	799	1790	807	309
150–160	2516	263	798	1797	830	324
160–170	2494	277	824	1837	852	333
170–180	2003	255	767	1716	802	305
180–190	1711	247	706	1636	761	282
190–200	1376	233	655	1519	702	263
200–210	1087	215	601	1422	633	248
210–220	824	196	550	1279	605	245
220–230	645	182	498	1172	539	209
230–240	487	159	457	1042	486	171
240–250	340	135	374	868	444	166
250–260	239	122	328	787	378	138
260–280	255	127	371	850	417	163
280–320	160	106	268	693	347	126

3 STELLAR POPULATION MODELS

We analyze the spectra of ETGs with the extended MILES (MIUSCAT) stellar population models [8] (Vazdekis et al. 2012; Ricciardelli et al. 2012, hereafter MIUSCAT-I, and MIUSCAT-II, respectively), combining CaT (Cenarro et al. 2001) and MILES (Sánchez-Blázquez et al. 2006) with Indo-U.S. empirical stellar libraries over the spectral range $\lambda\lambda 3465 - 9469$ Å, at a nominal resolution of 2.51 Å FWHM (Falcón-Barroso et al. 2011). MIUSCAT models are identical to MILES and CaT models in the spectral ranges covered by these libraries, $\lambda\lambda 3525 - 7500$ Å and $\lambda\lambda 8350 - 9020$ Å, respectively, while the Indo-U.S. is used to "fill the gap" between MILES and CaT and extend blueward and redward the wavelength coverage of the models (see MIUSCAT-I for details). Notice also that MIUSCAT models rely on solar-scaled isochrones with stellar spectra following the abundance pattern of our Galaxy, i.e. approximately solar-scaled at solar metallicity. The MIUSCAT SSPs cover a wide range of ages, from 0.06 to 17.78 Gyr, and seven metallicity bins, i.e. $[Z/H] = \{-2.32, -1.71, -1.31, -0.71, -0.4, 0, +0.22\}$. The SSPs are provided for several IMFs. We use here two power-law IMFs, described in Vazdekis et al. (1996), i.e unimodal and bimodal, both characterized by their slope Γ as a single free parameter (see Fig. 3). The bimodal IMFs are similar to the unimodal ones for stars with mass above 0.6 M$_\odot$, but significantly shallower at lower masses, becoming flat below ~ 0.2 M$_\odot$. For $\Gamma \sim 1.3$, the bimodal IMF gives a good representation of the Kroupa IMF, while the unimodal case coincides, for the same slope, with a Salpeter (1955) IMF. The lower and upper mass-cutoff of the IMFs are set to 0.1 and 100 M$_\odot$, respectively. We refer the reader to appendix A of Vazdekis et al. (2003) for a detailed description of unimodal and bimodal IMFs. For the present study, we interpolate the extended MILES (MIUSCAT) SSPs, for each IMF, over the age (metallicity) range from 1 (-0.4) to 17.78 Gyr ($+0.22$), where the models are expected to be safe (see MIUSCAT-I). Younger ages, as well as lower metallicities, than those considered here are not relevant to study our sample of luminous ETGs. The interpolation is done for 200 and 150 steps in age and metallicity, respectively. For bimodal IMFs, we consider the cases $\Gamma = \{0.3, 0.8, 1.0, 1.3, 1.5, 1.8, 2.0, 2.3, 2.8, 3.3\}$. For unimodal IMFs, we restrict the analysis to cases with $\Gamma \leqslant 2.3$. At larger slopes, current uncertainties in the modelling of very low Main Sequence stars may impact significantly the synthetic SEDs (see MIUSCAT-I).

[7] Hereafter, with this expression, we mean that the actual resolution of a given spectrum is obtained by adding in quadrature the σ_0 to the resolution of the SDSS spectrograph.

[8] The models are publicly available at `http://miles.iac.es/pages/ssp-models/miuscat-models.php`.

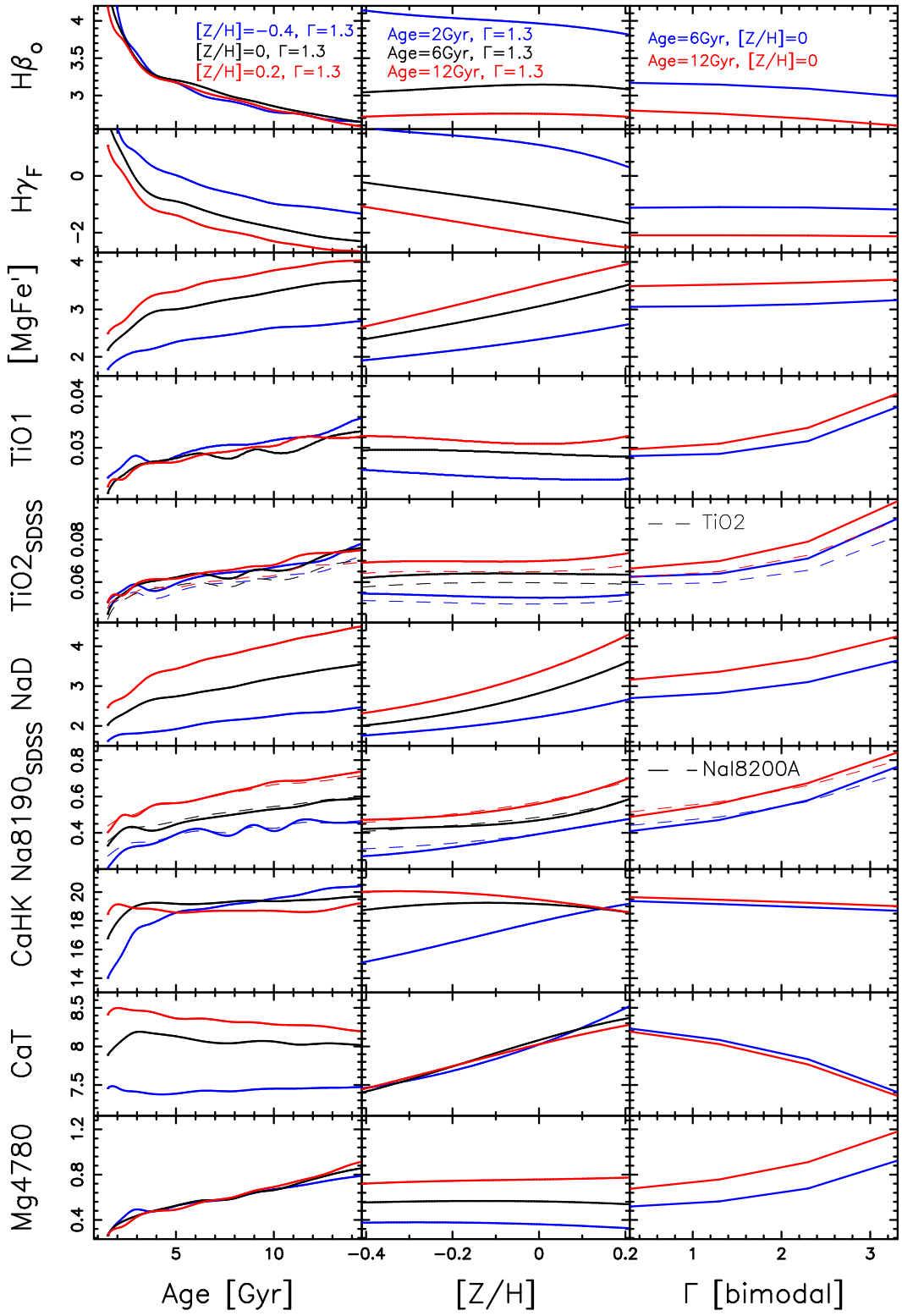

Figure 4. Sensitivity of selected spectral indices to age (left), metallicity (middle), and (bimodal) IMF slope (right). Different colours correspond to different MILES extended (MIUSCAT) SSPs, for age, metallicity, and IMF slope, as labelled in the top panels. In particular, we plot three SSPs with $\Gamma = 1.3$, and metallicities $[Z/H] = -0.4$, 0 (solar), and +0.2 (left panels); three SSPs with ages 2, 6, and 12 Gyr, and bimodal $\Gamma = 1.3$ (middle panels); and two SSPs with solar metallicity and ages of 6 and 12 Gyr (right panels). In the panels showing $\mathrm{TiO2_{SDSS}}$ and $\mathrm{Na8190_{SDSS}}$, we overplot the trends for the Lick-based TiO2 and the NaI8200A spectral indices, respectively. Notice the similar behaviour of the new ("SDSS") and the Lick-based indices (see text for details).

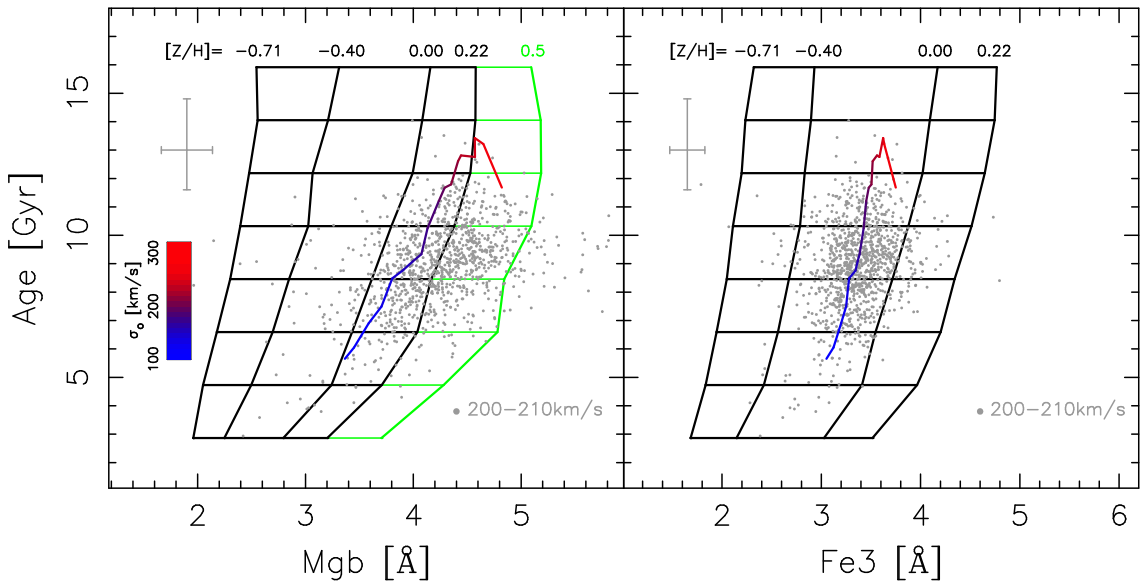

Figure 5. Illustration of the [α/Fe] proxy obtained from base (nearly solar-scaled) extended MILES (MIUSCAT) models. The *Age* parameter is plotted against Mg*b* (left) and Fe3 (right) spectral indices. Grey dots are ETGs within the $\sigma_0 \sim 200 - 210$ km s^{-1} bin, while the blue-through-red curve connects data points for the 18 σ_0 stacks, with colour encoded as shown by the bar on the left panel. The grey error bars show typical uncertainties on age, as well as on the Mg*b* and Fe3 indices. The grids show the effect of varying age and metallicity of extended MILES (MIUSCAT) SSPs, with the green portion, in the left plot, resulting from a (linear) extrapolation of the model Mg*b* to high ($[Z/H] = +0.5$) metallicity. The proxy is defined as the difference of metallicities estimated from the Mg*b* and Fe3 grids, respectively. Notice that for the grey points (i.e. single ETGs) the age is estimated from spectral fitting (as obtained from the `STARLIGHT` code), while for the stacks – because of the high S/N ratio – we used Hβ_o-based age estimates (see text for details).

4 SPECTRAL INDICES

Our analysis is mainly based on constraining the IMF by the use of targeted line strengths. We mainly focus on a detailed analysis of the spectral indices, although we also include information from spectral fitting to make the results more robust (as in FLD13, see §§7.5) The use of line strengths brings some well-known drawbacks into the study of unresolved stellar populations. First, indices are defined relative to pseudo-continua, often affected themselves by absorption features. Second, line strengths may reflect the abundance of individual elements in a stellar population, in addition to age, metallicity, and IMF, complicating the interpretation of their variation. On the other hand, spectral indices have the advantage of summarizing the spectral information in a few numbers. In principle, one can define specific indices that efficiently constrain metallicity and age, or – most importantly for this work – single element abundance patterns and the IMF. We select in this paper a variety of spectral indices, bringing the observed line strengths to solar scale by means of their correlations with the abundance ratio ([α/Fe], Sec. 5.2). This has the advantage of allowing for a direct comparison with the expectations from nearly solar-scaled, fully empirical – rather than theoretical – stellar population models (MIUSCAT). In contrast, CvD12a and Conroy & van Dokkum (2012b) adopted a direct spectral fitting approach, using α-enhanced stellar population models, based on synthetic stellar spectra to describe the effect of abundance patterns. We notice that most pixels of a galaxy spectrum are sensitive to age, metallicity, and abundance patterns, while only a small number of absorption features are sensitive to the IMF. Therefore, a direct comparison to stellar population models may be driven by differences between models and data, rather than true IMF variations. This further motivates our choice to rely on line strengths, and complement the analysis with the hybrid approach.

We point out that all line indices used for the present analysis are measured at the nominal resolution (i.e. SDSS plus σ_0) of each stack. Since line indices are also sensitive to velocity dispersion – as the broadening of lines changes their contribution to the fluxes measured both in the central and sidebands – we always extract information (e.g. IMF slope) by comparing indices to expectations of stellar population models smoothed to match the resolution of each individual stack. This makes the derived trends (of IMF slope as well as elemental abundances) with σ_0 independent of resolution. However, and for illustration purposes only, in the figures showing trends of line indices among different stacks, we correct the indices to a reference broadening of $\sigma_{0,\rm ref} = 200$ km s^{-1}. The correction is done by estimating the variation in each index when smoothing the best-fitting stellar population model to the σ_0 of a given stack and to $\sigma_{0,\rm ref}$, respectively. We note that 200 km s^{-1}corresponds to the central value of the σ_0 range of our sample, hence this choice of $\sigma_{0,\rm ref}$ minimizes the correction for all stacks in the figures. Notice that measuring indices at the original resolution of the stack, rather than degrading all stacks to the same maximum σ_0 value of ~ 300 km s^{-1}, has the advantage of maximizing the information extracted from the data, avoiding the effect of correlated variations among adjacent pixels when smoothing the data. However, to test the impact of resolution on our results, as well as to explore a wider parameter space in the analysis, we smooth both data and

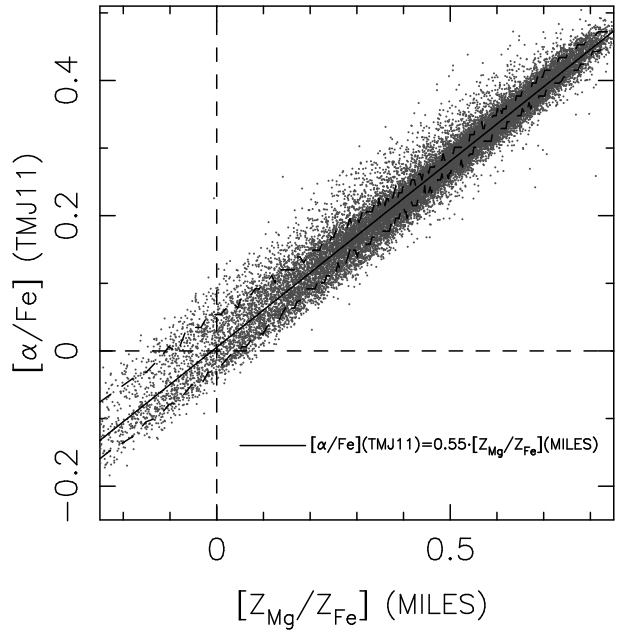

Figure 6. Comparison of the "true" [α/Fe] parameter with the (approximately) solar-scaled proxy, $[Z_{Mg}/Z_{Fe}]$, obtained from extended MILES (MIUSCAT) models (see the text). The [α/Fe] is estimated with TMJ11 stellar population models. Grey points correspond to the sample of 24,781 SPIDER ETGs selected for the present study. Dashed horizontal and vertical lines mark the value of zero on both axes. The solid curve is the best-fitting line, obtained with a least-squares fitting procedure, assuming [α/Fe] as dependent variable. Notice the small scatter, with a fitting rms of ∼0.025 dex in [α/Fe]. The black dashed curves, bracketing the best-fit line correspond to the 16th and 84th percentiles of the [α/Fe] distribution in bins of $[Z_{Mg}/Z_{Fe}]$.

models to the same σ_0 of 300 km s^{-1}, when performing the hybrid approach (Sec. 7.5).

4.1 Selection of spectral features

The list of spectral indices, adopted in this study is assembled as follows.

IMF-sensitive spectral indices. We have visually inspected the flux ratio of two bimodal SEDs, within contiguous, 300 Å width, spectral windows, looking for IMF-sensitive wavelengths (as, e.g., in figure 9 of MIUSCAT-I). The two SEDs are chosen to have the same age (10 Gyr) and (solar) metallicity, with $\Gamma = 0.3$ and 3.3, respectively. Matching the list of potentially useful wavelengths to existing lists of spectral indices resulted in a list of five IMF-sensitive features [9], namely Mg4780, TiO1, TiO2$_{\rm SDSS}$, Na8190$_{\rm SDSS}$, and CaT. Here, the CaT is defined as CaT=Ca1+Ca2+Ca3, following the definition of Cenarro et al. (2001). The definition of spectral indices – mostly based on previous works – is summarized in Tab. 2. Two exceptions are the Na8190$_{\rm SDSS}$ and TiO2$_{\rm SDSS}$ features, which are slightly different versions of the NaI8200A index, defined in MIUSCAT-I, and the well-known, Lick-based, TiO2 molecular band (Trager et al. 1998), respectively. In practice, we have modified the blue (red) pseudo-continua of NaI8200A (TiO2), in order to minimize systematic discrepancies between models and data (independent of the IMF). Further details on this issue are given in App. A.

Abundance-sensitive spectral indices. The list of IMF-sensitive spectral indices is complemented with the NaD and CaHK spectral features. These indices, being much more sensitive to Na and Ca abundances than IMF, can be useful tools to break the degeneracy between IMF and abundance ratios (see e.g. CvD12). For instance, by analyzing the diagram NaD vs. NaI (their NaI index being similar to our Na8190$_{\rm SDSS}$), STK12 concluded that both a dwarf-enriched IMF and overabundant [Na/Fe] are required to match the equivalent widths of a small set of ETGs from the SDSS. A powerful Ca abundance diagnostic is also given by the Ca4227 index (Trager et al. 1998). In fact, the Ca4227 has been recently used by Johansson et al. (2012) to conclude in favour of an underabundance of [Ca/Fe] in ETGs. Unfortunately, we have found that none of our fitting schemes (including the modelling of abundance patterns) is able to produce an acceptable fit to Ca4227. For this reason, we have excluded this index from the analysis, but for reference, we present a comparison between models and data for this index in Sec. 7.3.1. The definition of abundance-sensitive spectral indices is summarized, together with that of IMF-sensitive indices, in Tab. 2.

Age-metallicity sensitive spectral indices. In order to account for the well-known variation of age and metallicity with galaxy properties (e.g. Thomas et al. 2005), we also include the H$\beta_{\rm o}$, H$\gamma_{\rm F}$, and [MgFe]$'$ spectral indices. The H$\beta_{\rm o}$ is a modified Hβ index, optimized to minimize the age-metallicity degeneracy (Cervantes & Vazdekis 2009). The H$\gamma_{\rm F}$ is also a very useful age indicator, due to its small sensitivity to [α/Fe], similar to Hβ, in constrast to higher-order Balmer lines (Thomas et al. 2004). Finally, we adopt the total metallicity estimator [MgFe]$'$ of Thomas et al. (2003a), whose definition removes the residual dependence of the González (1993) [MgFe] spectral index on [α/Fe].

Fig. 4 plots the sensitivity of selected spectral indices to age, metallicity, and IMF. For each index, we show three panels, plotting line strengths of extended MILES (MIUSCAT) SSPs as a function of (from left to right) age, metallicity, and (bimodal) IMF slope, Γ. Each panel shows the model predictions for a small set of simple stellar populations. The extended MILES (MIUSCAT) SSPs have been smoothed to match the wavelength dependent resolution of SDSS (see Sec. 2.2) plus a σ of 200 km s^{-1}. Both H$\beta_{\rm o}$ and H$\gamma_{\rm F}$ decrease significantly with increasing age. However, while H$\beta_{\rm o}$ is essentially independent of metallicity, consistent with its definition (Cervantes & Vazdekis 2009), H$\gamma_{\rm F}$ tends to decrease with $[Z/H]$. Both indices (and in particular H$\gamma_{\rm F}$) are independent of IMF. [MgFe]$'$ is also independent of Γ, increasing with total metallicity, and, to a lesser extent, with age. As expected, all TiO1, TiO2$_{\rm SDSS}$, Na8190$_{\rm SDSS}$, CaT, and Mg4780 show a significant dependence on Γ. The TiO1, TiO2$_{\rm SDSS}$, Na8190$_{\rm SDSS}$, and Mg4780 increase with

[9] Notice that the Mgb5177 index was also first selected among the IMF-sensitive indices. However, because of its strong sensitivity to [α/Fe], we have decided not to include it in the analysis. Moreover, as discussed by CvD12, the sensitivity of Mgb5177 to the IMF is significantly reduced by the fact that a CrI blend partially overlaps with the red pseudo-continuum.

IMF slope, while CaT exhibits the opposite behaviour. The TiO indices, as well as Mg4780, are insensitive to metallicity, but tend to increase with age. For $TiO2_{SDSS}$(TiO1), the latter trend is weaker (similar) to that with Γ. Notice also that $TiO2_{SDSS}$ has a dependence on age, metallicity, and IMF, very similar to the Lick-based TiO2 index (dashed curves in the Figure). Regarding $Na8190_{SDSS}$, it strongly increases with IMF slope, with a weaker dependence on age and metallicity. The NaD shows a decent sensitivity to IMF, but it strongly increases with both age and metallicity. On the contrary, for age older than ~ 2 Gyr and either solar or super-solar metallicity, the CaHK, i.e. the other abundance-sensitive index included in this study, is essentially independent of both age, metallicity, and IMF. The CaT index is constant with respect to age, for SSPs older than a few Gyr, while it depends significantly on metallicity and decreases significantly with increasing IMF slope.

The different sensitivity of all selected spectral indices to age, metallicity, and IMF, makes them a powerful tool to constrain all these parameters simultaneously, as shown in Sec. 7.

An important remark concerns the effect of internal dust on spectral indices. Being a resonant line, NaD can be highly affected by interstellar absorption. This has hampered, so far, its use, in combination with $Na8190_{SDSS}$, to constrain the relative contribution of [Na/Fe] and IMF to gravity-sensitive features. The same issue applies to TiO1 (see e.g. TMJ11), whose blue pseudo-continuum can be affected by the Na interstellar absorption, leading to overly weak strengths. Notice that our work is virtually unaffected by dust, as the stacked spectra are constructed by removing, *ab initio*, ETGs with significant amount of reddening. Also, plotting NaD as well as TiO1 strengths as a function of $E(B-V)$, for spectra in each σ_0 bin, does not show any significant correlation.

Another remark is that all our spectral indices are measured within the central $3''$ diameter aperture of the SDSS fibres, corresponding to a smaller fraction of the effective radius for the more massive galaxies. Radial trends of spectral indices might thus bias our conclusions on the IMF variation with galaxy mass. In App. C we present the trends of some IMF-sensitive indices with effective radius, showing that the aperture effect does not affect our conclusions.

5 THE EFFECT OF [α/Fe]

There is a well-known correlation between velocity dispersion and [α/Fe] abundance ratio (see, e.g., Trager et al. 2000). This correlation needs to be addressed in our study, to confirm that our trends in the IMF-sensitive spectral indices are not simply caused by the change in [α/Fe]. In order to study this issue, we split our sample of ETGs within each σ_0 bin (see Sec. 2.1), according to [α/Fe]. This is done by estimating a proxy of [α/Fe] for each galaxy, as detailed in Sec. 5.1. In Sec. 5.2 we present the correlations of indices vs. proxy.

5.1 [α/Fe] stacks at fixed σ_0

For each ETG, we estimate a proxy of [α/Fe], based on (nearly) solar-scaled extended MILES (MIUSCAT) models. First, we measure the galaxy luminosity-weighted age by spectral fitting the wavelength range from 3900 to 7350 Å [10], with the `STARLIGHT` fitting code (Cid Fernandes et al. 2005). We feed `STARLIGHT` with an input list of 132 SSPs, covering a wide range of ages (1–17.78 Gyr) and metallicities (from $[Z/H] = -0.71$ to $+0.22$), assuming a Kroupa IMF. For the given age, we estimate two independent metallicities, Z_{Mg} and Z_{Fe}, from the spectral indices Mgb and Fe3 $\equiv$ (Fe4383+Fe5270+Fe5335)/3, respectively. This procedure is illustrated in Fig. 5, for galaxies in the $\sigma_0 = 200-210$ km s^{-1} stack (grey dots). The Figure also plots *Age*-Mg*b* and *Age*-Fe3 grids for MILES extended (MIUSCAT) SSPs (Kroupa IMF). While at solar scale both $[Z/H]_{Mg}$ and $[Z/H]_{Fe}$ should coincide, for an α-enhanced population the $[Z/H]_{Mg}$ is larger than $[Z/H]_{Fe}$, as it is actually the case for most data-points. Since the $[Z/H]_{Mg}$ is often larger than the maximum metallicity of the base SSPs ($[Z/H] = +0.22$), for each age, we extrapolate the model Mg*b* up to a metallicity of $[Z/H] = +0.5$, as shown by the green portion of the grid in the left panel of Fig. 5. We define as solar proxy of [α/Fe], the difference $[Z_{Mg}/Z_{Fe}] \equiv [Z/H]_{Mg} - [Z/H]_{Fe}$. Notice that for single SDSS spectra estimating ages from spectral fitting, rather than single spectral features (e.g. Hβ), gives a more robust (i.e. less uncertain) age, and thus metallicity, estimate. In fact, the S/N ratio of single (with respect to stacked) SDSS spectra prevents us from obtaining accurate age estimates from Hβ alone (with the median Hβ_o equivalent width uncertainty being ~ 0.3 Å). Large age uncertainties would spread a significant fraction of points at both high and low ages. As seen from the shape of the *Age*-Mg*b* grid (Fig. 5), at fixed Mgb, young populations do require a larger extrapolation in $[Z/H]$ than older ones, making the proxy estimate more uncertain when the errors in the age are larger. For the stacked spectra, thanks to the high S/N ratio, we estimate the $[Z_{Mg}/Z_{Fe}]$ from Hβ_o-based (rather than spectral fitting) ages, as shown in Fig. 5. In practice, we derive the SSP-equivalent age by fitting Hβ_o and [MgFe]$'$ equivalent lines with MILES SSPs (Kroupa IMF). Varying the IMF (according to the $1SSP$ fitting results of Sec. 7.1) and/or the method to estimate the age (`STARLIGHT` rather than Hβ_o), does not change the $[Z_{Mg}/Z_{Fe}]$ more than by a few percent [11]. The $[Z_{Mg}/Z_{Fe}]$ increases systematically for our stacks, from ~ 0.18 in the lowest σ_0 bin, up to ~ 0.47 at highest σ_0. This is consistent with the well-known result that the [α/Fe] of ETGs increases with σ_0 (see, e.g., Trager et al. 2000; Thomas et al. 2005).

Since we aim to stack spectra with respect to $[Z_{Mg}/Z_{Fe}]$, an important issue is to establish whether reliable estimates of $[Z_{Mg}/Z_{Fe}]$ can be obtained for individual galaxies in our sample. The relevant parameter is the median S/N (per Å) over the passbands of the Mgb5177

[10] The lower limit of 3900 Å avoids the bluest part of the SDSS spectral range, which is potentially more affected by small-scale flat-fielding uncertainties, while the upper limit corresponds approximately to the upper limit of the MILES spectral library.

[11] On the other hand, the age estimates differ when derived with different methods. For instance, STARLIGHT luminosity-weighted ages are about 20 % older than Hβ_o-based, SSP equivalent, ages. This difference implies a vertical offset between the blue-through-red curve and the center of the distribution of grey points in Fig. 5.

Table 2. Targeted spectral indices to constrain the low-mass end of the IMF.

Index	Units	Blue Pseudo-continuum [Å]	Central feature [Å]	Red Pseudo-continuum [Å]	source
CaHK	Å	3806.5–3833.8	3899.5–4003.5	4020.7–4052.4	Serven+05
Mg4780	Å	4738.9–4757.3	4760.8–4798.8	4819.8–4835.5	Serven+05
NaD	Å	5860.625–5875.625	5876.875–5909.375	5922.125–5948.125	Trager+98
TiO1	mag	5816.625–5849.125	5936.625–5994.125	6038.625–6103.625	Trager+98
$TiO2_{SDSS}$	mag	6066.625–6141.625	6189.625–6272.125	6422.0–6455.0	This work
$Na8190_{SDSS}$	Å	8143.0–8153.0	8180.0–8200.0	8233.0–8244.0	This work
Ca1	Å	8474.0–8484.0	8484.0–8513.0	8563.0–8577.0	Cenarro+01
Ca2	Å	8474.0–8484.0	8522.0–8562.0	8563.0–8577.0	Cenarro+01
Ca3	Å	8619.0–8642.0	8642.0–8682.0	8700.0–8725.0	Cenarro+01

and Fe3 spectral features (hereafter S/N_{MgFe}). We find that for individual spectra the S/N_{MgFe} ranges from $\sim$ 15 to 30 – quoting the 10-th and 90-th percentiles of the distribution – with a median value of 20. Notice that the S/N is larger for the Mg and Fe than for the $Na8190_{SDSS}$ feature, because of the rapid decline of the SDSS spectrograph throughput above $\sim$ 8000 Å. We estimate the uncertainty on $[Z_{Mg}/Z_{Fe}]$ by comparing estimates of this quantity for 2,313 galaxies of our sample with repeated observations in SDSS (see Paper I and Paper IV), finding that the error on $[Z_{Mg}/Z_{Fe}]$ varies approximately in a linear way with S/N (in the range $12 \leqslant S/N_{MgFe} \leqslant 32$), from $\sim$ 0.2 at $S/N_{MgFe} = 15$, to $\sim$ 0.1 at $S/N_{MgFe} = 30$. By selecting repeated observations whose spectra have large differences in S/N ($\Delta S/N_{MgFe} > 10$), we also find no significant variation in their average $[Z_{Mg}/Z_{Fe}]$ ($\sim 0.03 \pm 0.04$), implying no differential bias in $[Z_{Mg}/Z_{Fe}]$ with S/N, and thus with respect to σ_0 (i.e. among different stacks).

Fig. 6 compares the "presumably-true" [α/Fe] [12] with $[Z_{Mg}/Z_{Fe}]$ for our sample of 24,781 ETGs (see Sec. 2.1). The "true" [α/Fe] is estimated by comparing the [MgFe]$'$, Mgb5177, and Fe3 spectral indices of each galaxy to the prescriptions of Thomas, Maraston & Johansson (2011, hereafter TMJ11) α-enhanced SSP models (covering a range of age and metallicity). To this effect, we fix the age of TMJ11 models to the luminosity-weighted age measured from `STARLIGHT` with MILES models, as described above. Hence, both [α/Fe] and $[Z_{Mg}/Z_{Fe}]$ in Fig. 6 are computed for the same age, but using different models [13]. Notice the tight relation between [α/Fe] and solar proxy, well described by the linear best-fit line in the Figure, with a fitting rms of $\sim$ 0.025 dex. This small scatter proves that indeed, one can study abundance ratio effects by relying completely on the MILES-based (nearly solar-scaled) $[Z_{Mg}/Z_{Fe}]$ proxy. Notice that the relation between [α/Fe] and $[Z_{Mg}/Z_{Fe}]$ has a slope of about 0.5. Hence the [α/Fe] of our 18 σ_0 stacks varies from $\sim$ 0.09 at lowest σ_0, to $\sim$ 0.23 at highest σ_0 (see the $[Z_{Mg}/Z_{Fe}]$ values reported above).

We stack galaxies according to $[Z_{Mg}/Z_{Fe}]$, considering six $[Z_{Mg}/Z_{Fe}]$ bins for each σ_0 interval. The $[Z_{Mg}/Z_{Fe}]$ bins are defined by selecting ETGs (1) below the 10-th percentile, (2) below the 25-th percentile, (3) between the 25-th and 50-th percentiles, (4) between the 50-th and 75-th percentiles, (5) above the 75-th percentile, and (6) above the 90-th percentile of the $[Z_{Mg}/Z_{Fe}]$ distribution. For each case, we median-combine the spectra, as described in Sec. 2.2. At fixed σ_0, the $[Z_{Mg}/Z_{Fe}]$ stacks span a range of $\delta([Z_{Mg}/Z_{Fe}]) \sim 0.6$ ($\delta([\alpha/\mathrm{Fe}]) \sim 0.3$). We use these stacks to study the dependence of our targeted spectral indices on element abundance ratios.

5.2 Correlations with [α/Fe]

Fig. 7 plots the variation of the spectral indices as a function of the solar proxy for α-enhancement ($[Z_{Mg}/Z_{Fe}]$) for all stacked spectra within the 18 bins in σ_0. In addition to the indices selected for the IMF study (see above), we also plot Mgb5177 and Fe3, which enter the definition of $[Z_{Mg}/Z_{Fe}]$ (see Sec. 5.1). We point out that all indices are measured at the nominal resolution of the stacks (SDSS plus σ_0). Hence, while the variation of the indices at fixed σ_0 is not affected by resolution, the variation of indices among different σ_0 bins is also partly driven by their different velocity dispersion, an effect that we take into account in the analysis (see below).

Most of the targeted spectral indices exhibit clear trends with $[Z_{Mg}/Z_{Fe}]$. This might be due to the dependence of the indices on [α/Fe], but also due to a variation of age, metallicity, IMF, and/or individual element abundances within each bin. The Mgb5177 increases with $[Z_{Mg}/Z_{Fe}]$, while Fe3 shows the opposite behaviour. Notice that this different behaviour is not a mere consequence of the fact that we stacked spectra with respect to $[Z_{Mg}/Z_{Fe}]$, as $[Z_{Mg}/Z_{Fe}]$ can change because of either a variation of Mgb5177 or Fe3. The tight correlation in panels (k) and (i) of Fig. 7, rather, reflect the fact that Mgb5177 (Fe3) anticorrelates with Fe (Mg) abundance (see, e.g., figure 1 of Thomas, Johansson & Maraston 2011). For what concerns the IMF, one can notice that, at fixed $[Z_{Mg}/Z_{Fe}]$, the dynamical range of all IMF-sensitive indices with respect to σ_0 is much larger than that with $[Z_{Mg}/Z_{Fe}]$ at fixed σ_0. Hence, the IMF is likely not driving the $[Z_{Mg}/Z_{Fe}]$ trends. This result also holds true when removing the effect of age and metallicity, as well as the dependence of line indices on σ_0, from the $[Z_{Mg}/Z_{Fe}]$ correlations (see below). The panels with Hβ_o, Hγ_F, and [MgFe]$'$ show that age and metallicity vary significantly at fixed σ_0, in the sense of galaxies with higher α-enhancement having older ages (i.e. weaker Balmer

[12] The expression "true" refers to [α/Fe] estimates obtained from stellar population models taking abundance ratios explicitly into account.

[13] Although the two sets of models differ, one should notice that TMJ11 models are actually based on fitting functions from the MILES stellar library.

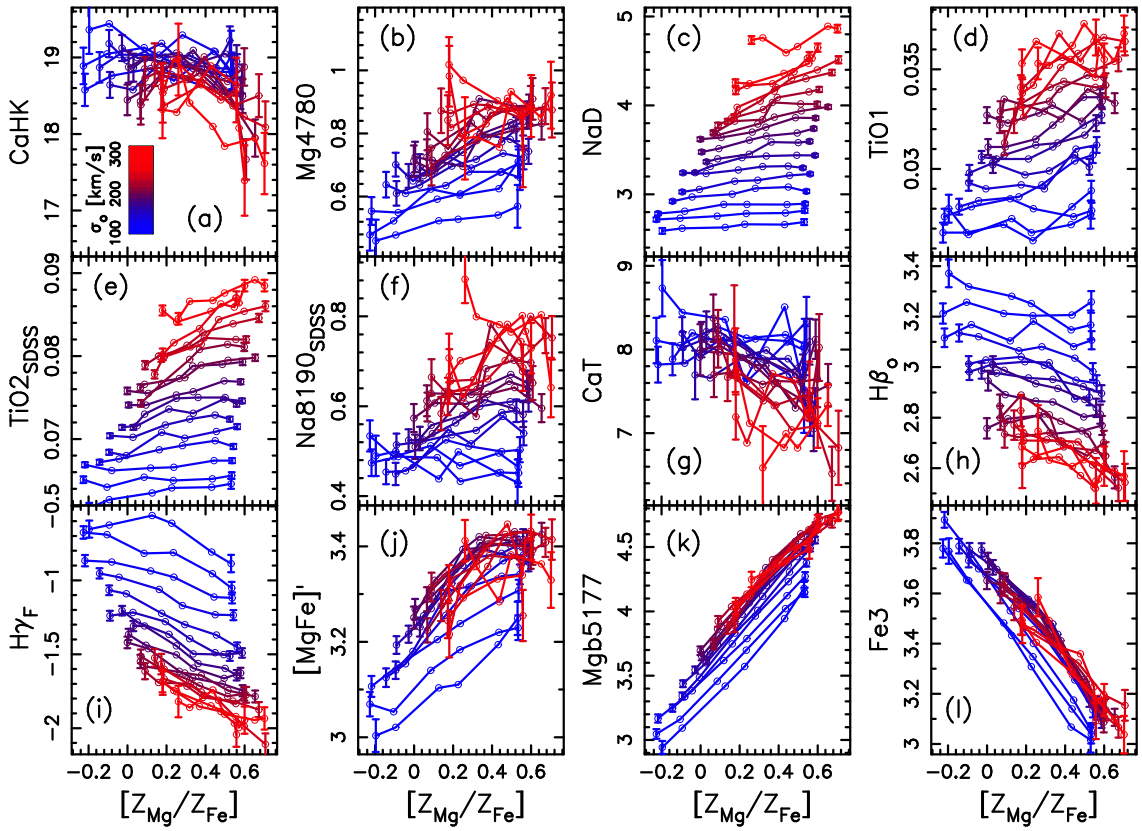

Figure 7. Dependence of spectral indices on solar proxy for α-enhancement, $[Z_{Mg}/Z_{Fe}]$. All indices refer to stacks at their nominal resolution, i.e. SDSS instrumental resolution plus σ_0. Different colours correspond to different velocity dispersion bins, as shown by the colour bar in the top–left panel. Panels (a–g), as labelled, plot IMF- and abundance-sensitive indices (see the text), while the remaining panels correspond to indices sensitive to age and metallicity (h–j), and [α/Fe] (panels k and l). Error bars are 1 σ measurement errors on the line strengths. Notice the strong increase (decrease) of Mgb5177 (Fe3) as a function of $[Z_{Mg}/Z_{Fe}]$, reflecting the variation of [α/Fe] at fixed σ_0. The dependence of Hβ_o and [MgFe]$'$ on $[Z_{Mg}/Z_{Fe}]$ likely reflects a variation of age and metallicity in each velocity dispersion bin.

lines), as well as higher metallicities (i.e. larger [MgFe]$'$). This conclusion is based on the fact that, at fixed total metallicity ([Z/H]), both Hβ_o and Hγ_F, as well as [MgFe]$'$, are essentially independent of [α/Fe] [14].

We correct the spectral indices for their dependence on age and metallicity at fixed σ_0, as well as their dependence on resolution among stacks with different σ_0. The correction procedure estimates age and metallicity from the Hβ_o–[MgFe]$'$ diagram for each stack, and then uses those age and metallicity estimates to remove the age/metallicity dependence of each index, for each stack in a given σ_0 interval. More explicitly, we adopt the following equation:

$$\mathrm{I_{corr}} = \mathrm{I_{obs}} - \mathrm{I_{mod}}(\mathrm{H}\beta_o; \mathrm{MgFe}'; \mathrm{Kroupa}) + \langle \mathrm{I_{mod}} \rangle_{200}, \qquad (1)$$

where $\mathrm{I_{obs}}$ is the index line strength for a given $[Z_{Mg}/Z_{Fe}]$ stacked spectrum; I_{corr} is the index after correction is applied; $\mathrm{I_{mod}}(\mathrm{H}\beta_o; \mathrm{MgFe}'; \mathrm{Kroupa})$ is the index value expected for the same stack by fitting its Hβ_o and [MgFe]$'$ EWs with extended MILES (MIUSCAT) SSPs having a Kroupa IMF; $\langle \mathrm{I_{mod}} \rangle_{200}$ is the index value predicted for an SSP with a Kroupa IMF, $\sigma_{0,\mathrm{ref}} = 200\ \mathrm{km\,s^{-1}}$ (see Sec. 4), and age and metallicity fixed to their average values within the σ_0 bin. Notice that the quantities $\mathrm{I_{mod}}(\mathrm{H}\beta_o; \mathrm{MgFe}'; \mathrm{Kroupa})$ are computed by first correcting Hβ_o for nebular emission (see App. B for details). The $\mathrm{I_{mod}}(\mathrm{H}\beta_o; \mathrm{MgFe}'; \mathrm{Kroupa})$ is computed at the same resolution as $\mathrm{I_{obs}}$, i.e. the SDSS resolution plus the σ_0 of the given stack. Since $\langle \mathrm{I_{mod}} \rangle_{200}$ is computed at $\sigma_{0,\mathrm{ref}} = 200\ \mathrm{km\,s^{-1}}$, Eq. 1 does also correct the trends of Fig. 7 to the same spectral resolution. We point out that the correction does not assume any variation of IMF among stacks, which is the hypothesis to be tested in this paper. Furthermore, as noticed in Sec. 4, the reference value of $\sigma_{0,\mathrm{ref}} = 200\ \mathrm{km\,s^{-1}}$is the central value of the σ_0 range of our stacks, hence minimizing the resolution correction to the indices for all bins. Fig. 8 is the same as Fig. 7 but after applying Eq. 1, i.e. it shows the genuine dependence of the indices on $[Z_{Mg}/Z_{Fe}]$. Most of the trends are weaker than those presented in Fig. 7. In particular, by construction, Hβ_o and [MgFe]$'$ do not show any variation with $[Z_{Mg}/Z_{Fe}]$, while Hγ_F does not show any significant correlation with $[Z_{Mg}/Z_{Fe}]$, aside from a few bins (e.g. for the lowest σ_0; where the correction might have been overestimated). For what concerns IMF-sensitive indices, as already noticed above, their variation with σ_0 is similar, or

[14] According to Thomas et al. (2004), Hβ and Hγ_F are expected to slightly increase with [α/Fe], while Fig. 7 shows a trend of both indices to *decrease* with $[Z_{Mg}/Z_{Fe}]$, reflecting a variation in age.

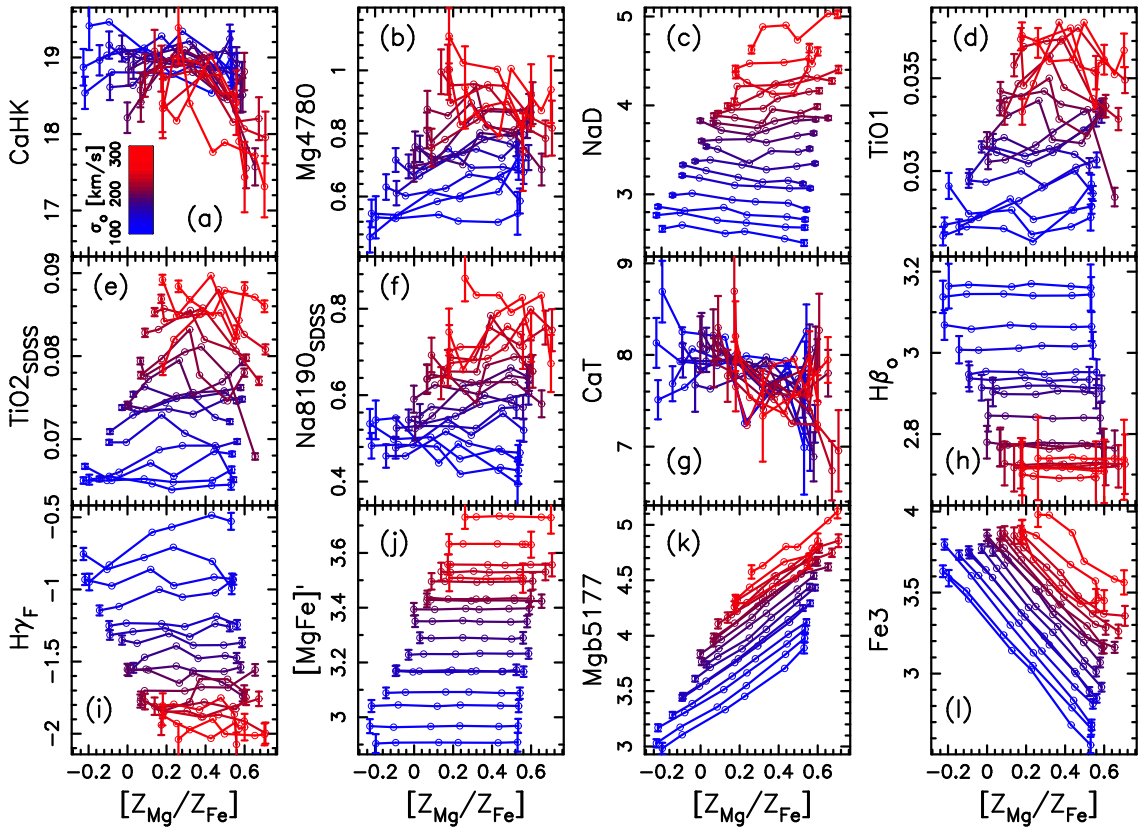

Figure 8. Same as Fig. 7 but after removing the trends of Hβ_o and [MgFe]′ in each σ_0 bin, using extended MILES (MIUSCAT) SSPs with a Kroupa IMF (see the text).

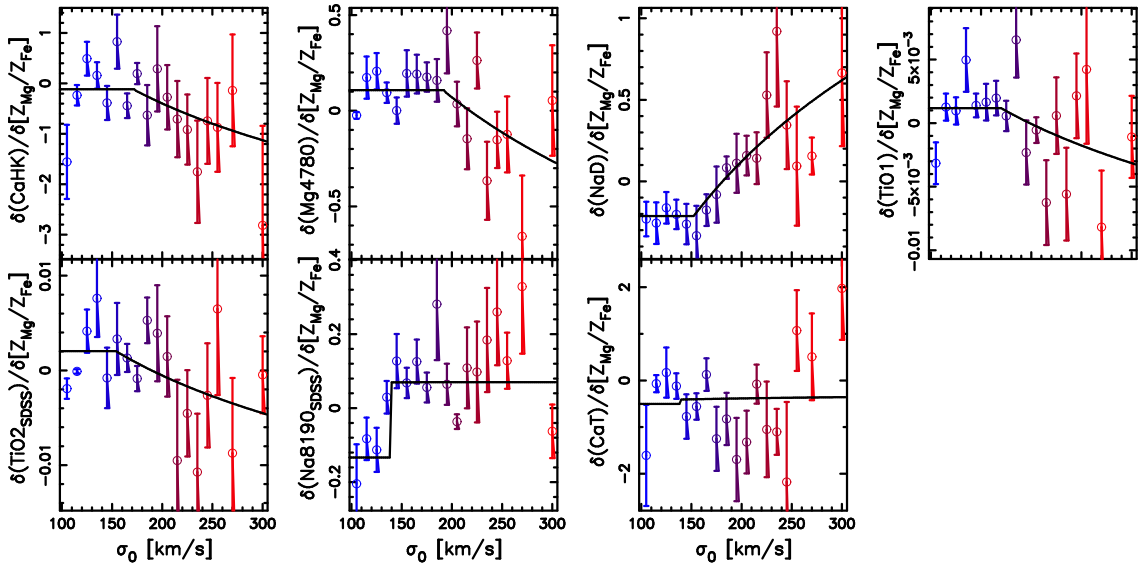

Figure 9. Slopes of the trends of spectral indices vs. $[Z_{Mg}/Z_{Fe}]$ as a function of velocity dispersion. Colours correspond to different velocity dispersion values, as in Fig. 7. Error bars are $1\,\sigma$ uncertainties of the slope. Black curves trace the best-fitting analytic approximations of the observed trends (see the text).

even larger, at low $[Z_{Mg}/Z_{Fe}]$, implying that σ_0 is the main driver of IMF variations among stacks. Since the error on $[Z_{Mg}/Z_{Fe}]$ is about 0.15 dex (see Sec. 5), i.e. significantly smaller than the $[Z_{Mg}/Z_{Fe}]$ range of ~ 0.8 dex, our finding is likely not affected by the errors on $[Z_{Mg}/Z_{Fe}]$. In addition, by stacking only galaxies with a higher S/N_{MgFe} (> 25), we find consistent trends to those presented in Fig. 8.

In order to characterize the trends of spectral indices with $[Z_{Mg}/Z_{Fe}]$, we fit them with linear relations, treating index values as independent variables. In Fig. 9, we plot the slopes of the best-fitting relations, $\delta(\mathrm{index})/\delta([Z_{Mg}/Z_{Fe}])$, as a function of σ_0. For each index line strength, I, and each σ_0 bin, we also compute the rms of the residuals around the best fit (s_I). The quantity s_I provides an estimate of the uncertainty in the use of linear relations to interpolate/extrapolate index values to solar abundances ($[Z_{Mg}/Z_{Fe}]= 0$), and is included into the error budget when fitting stellar population models to data (Sec. 6). The figure shows that all indices except CaT, exhibit two regimes with different slopes, featuring a constant slope at low σ_0 ($\lesssim 130-150$ km s^{-1}), followed by a correlation with σ_0 at higher velocity dispersion. This behaviour is traced by the black curves in each panel of Fig. 9. Each curve is obtained by connecting the median slope value at low σ_0 to a best-fitting power-law relation at higher σ_0. For CaT, we notice that our stacking procedure involves fewer spectra (i.e. only those at lower redshift, see Sec. 2.2), making the corresponding $[Z_{Mg}/Z_{Fe}]$ trends – hence the slope values in Fig. 9 – not as robust as with other indices. For instance, given the large uncertainty on the slopes for the three highest σ_0 bins, we cannot exclude that CaT is insensitive to $[Z_{Mg}/Z_{Fe}]$ at lowest σ_0, with the slope becoming negative at $\sigma_0 > 150$ km s^{-1}, as for CaHK. The main features of the $[Z_{Mg}/Z_{Fe}]$ trends can be summarized as follows.

Na indices – At low velocity dispersion, the median slopes are negative, i.e. both NaD and Na8190$_{\rm SDSS}$ tend to decrease with $[Z_{Mg}/Z_{Fe}]$. On the contrary, at high velocity dispersion, the slopes are positive, i.e. the Na indices increase with $[Z_{Mg}/Z_{Fe}]$. The low-σ_0 behaviour is qualitatively consistent with the predictions of the CvD12 stellar population models, where [α/Fe] is expected to affect the continua of both NaD and Na8190$_{\rm SDSS}$, causing these indices to decrease with [α/Fe]. However, CvD12 models predict a slope of $\delta(\mathrm{Na8190})/\delta([\alpha/\mathrm{Fe}]) \sim -0.5$ [15], which is significantly different from the value of -0.15 one obtains for the lowest three bins of σ_0 (after accounting for the relation between $[Z_{Mg}/Z_{Fe}]$ and [α/Fe], see Fig. 6). The same discrepancy exists for NaD where we measure $\delta(\mathrm{NaD})/\delta([\alpha/\mathrm{Fe}]) \sim -0.4$ (at lowest σ_0), while CvD12 models predict ~ -2. Even stronger differences exist when comparing different models, as shown in Tab. 3, where we report the [α/Fe] sensitivity of NaD for different stellar population models, namely CvD12,

[15] This value refers to CvD12 models with an age of 13.5 Gyr and Chabrier IMF, smoothed to $\sigma = 200$ km s^{-1}. Notice that CvD12 models are computed for [Fe/H] = 0. Hence, higher [α/Fe] SSPs have higher total metallicity, and the variation of a given index with [α/Fe] does also reflect a metallicity variation. Since Na8190$_{\rm SDSS}$ tends to increase with $[Z/H]$, one might expect an even steeper slope (i.e. more negative) than that reported above (-0.5).

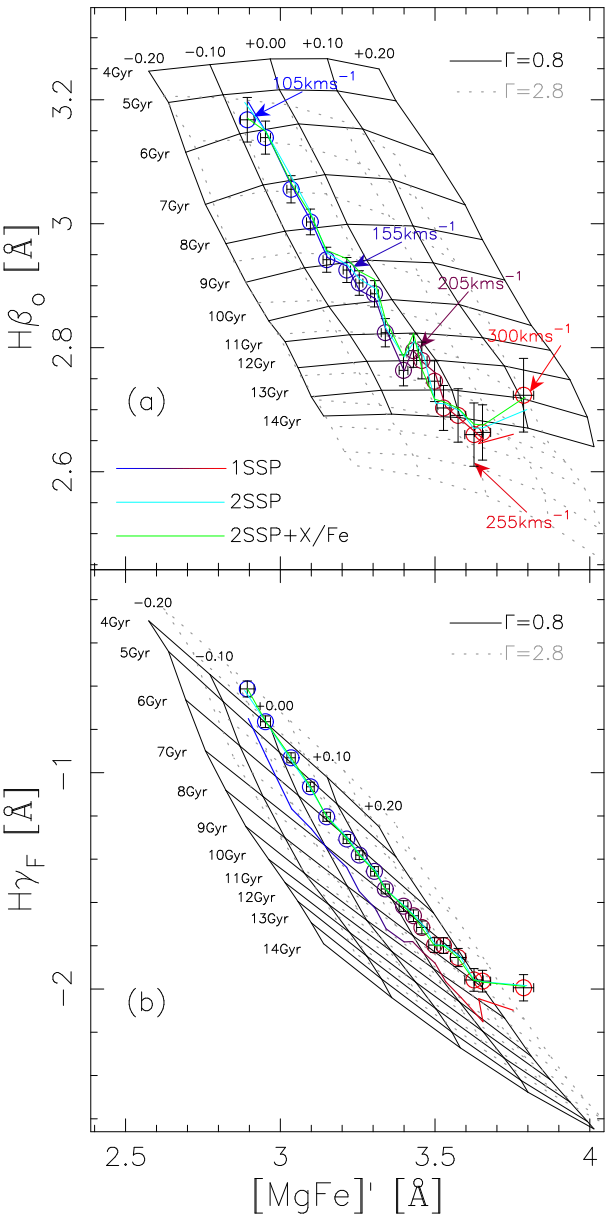

Figure 10. Results of fitting spectral indices with $1SSP$, $2SSP$, and $2SSP + X/Fe$, models. The age-sensitive spectral indices Hβ_o (*top*) and Hγ_F (*bottom*) are shown as a function of the total metallicity proxy, [MgFe]′. The grids correspond to 1SSP extended MILES (MIUSCAT) models, smoothed to a resolution of 200 km s^{-1}, with different age and metallicity, as labelled, for a top-heavy ($\Gamma = 0.8$; black) and bottom-heavy ($\Gamma = 2.8$; grey) bimodal IMF. Open circles plot line strengths of the 18 σ_0 stacks corrected to a common resolution of 200 km s^{-1}. Error bars are given at the $2\,\sigma$ level (including measurement errors and $[Z_{Mg}/Z_{Fe}]$ correction uncertainties). Circles are plotted with different colours, as in Fig. 9, depending on the σ_0 bin. Solid curves show the best-fitting solutions for $1SSP$ (blue-through-red curve), $2SSP$ (cyan), and $2SSP + X/Fe$ (green).

Table 3. Sensitivity of the NaD index to [α/Fe] according to different stellar population models.

model† (1)	δ(NaD)/δ([α/Fe]) (2)	model parameters (3)
TMJ11	+0.2	Salpeter IMF; $[Z/H] = 0.0$; Age= 10 Gyr; $0 \leqslant$[α/Fe]$\leqslant 0.5$
CvD12	−2.0	Chabrier IMF;$[Fe/H] = 0.0$; Age= 13.5 Gyr; $0 \leqslant$[α/Fe]$\leqslant 0.3$
COE07	−1.3	Chabrier IMF; $[Fe/H] = 0.0$; Age= 10 Gyr; $0 \leqslant$[α/Fe]$\leqslant 0.4$
CER07	−2.5	Kroupa IMF; $[Z/H] = 0.0$; Age= 10 Gyr; $0 \leqslant$[α/Fe]$\leqslant 0.4$

† TMJ11: Thomas, Maraston & Johansson (2011); CvD12: Conroy & van Dokkum (2012a); COE07: Coelho et al. (2007); CER07: Cervantes et al. (2007).

TMJ11, Cervantes et al. (2007, CER07), and Coelho et al. (2007, COE07). We find large differences when comparing different models [16]. Moreover, while CvD12, COE07, and CER07, agree qualitatively, in that the NaD weakens as [α/Fe] increases, TMJ11 models predict a mild *increase* with enhancement. Unfortunately, the same model comparison cannot be performed for Na8190$_{\rm SDSS}$, as only CvD12 models can be used to make predictions [17] at $\lambda \sim 8200$ Å.

TiO indices – The slopes change similarly for both indices, from slightly positive at low σ_0 to negative (on average) for $\sigma_0 \gtrsim 200$ km s^{-1}. Even in this case, large differences exist when comparing different models, where the two TiO indices are expected to be either almost independent (TMJ11); strongly increasing (CER07); mildly increasing (CvD12); or mildly decreasing (COE07) with [α/Fe].

Ca indices – Both CaHK and CaT have slopes consistent with zero at low σ_0. The slopes become negative at high σ_0 for CaHK, while for CaT the trend is less clear. Notice that CvD12 models predict both indices to increase with [α/Fe], the same trend being also predicted by COE07 and CER07 models for the CaHK index, in contrast to our findings (at both low and high σ_0). For CaHK, this discrepancy might also be due to the fact that this index is expected to be affected, for low mass stars, by chromospheric emission fill-in, hampering its modelling.

$Mg4780$ – This index mildly increases with $[Z_{Mg}/Z_{Fe}]$ at the lowest σ_0, consistent with the expected sensitivity to [Mg/Fe] (see Serven et al. 2005), while it decreases with $[Z_{Mg}/Z_{Fe}]$ at high σ_0. This double-regime behaviour is similar to that of the other indices shown, and indicates that $Mg4780$ might be sensitive to other elements [18] besides Mg.

The fact that the response of spectral indices to $[Z_{Mg}/Z_{Fe}]$ depends on σ_0 implies that $[Z_{Mg}/Z_{Fe}]$ traces different element abundance ratios at different galaxy mass scales. At high σ_0, the positive slope of the $[Z_{Mg}/Z_{Fe}]$ trends of NaD and Na8190$_{\rm SDSS}$ might be reflecting a stronger increase in Na abundance with $[Z_{Mg}/Z_{Fe}]$, with respect to other α elements. Would this be the case, one might expect a negative slope of Ca indices at high σ_0, as the abundance of Na, at fixed Ca abundance, is expected to influence the Ca line strengths through its effect on electron pressure in stellar atmospheres (see e.g. CvD12). While this is indeed the case for CaHK, the situation for CaT is less clear (see above)[19]. In practice, a variation in $[Na/Ca]$ with [α/Fe], at fixed σ_0, might dominate the effect of electron pressure, eventually leading to no correlation among the slopes of Ca and Na indices. On the other hand, at low (relative to high) σ_0, the trends with $[Z_{Mg}/Z_{Fe}]$ might be reflecting instead the true dependence of the spectral indices with [α/Fe]. Regardless of what causes the variation of the slopes, the main point for the present study is that one can use these slopes, for each σ_0 bin, in order to correct the observed indices to solar abundance ratio ($[Z_{Mg}/Z_{Fe}]= 0$), and compare them with the predictions from (nearly solar-scale) MILES extended (MIUSCAT) models.

6 FITTING PROCEDURE

For a given IMF (either bimodal or unimodal), we adopt a multi-index fitting procedure, minimizing the following expression:

$$\chi^2(\Gamma) = \sum \frac{(I_{corr} - I_{MOD})^2}{\sigma_I^2 + s_I^2}, \qquad (2)$$

where the sum extends over all the selected spectral indices (see Sec. 4), I_{corr} and s_I are the index line strength corrected to $[Z_{Mg}/Z_{Fe}]$=0 and the correction uncertainty, respectively (see Sec. 5.2), σ_I is the measurement uncertainty on I (reflecting the statistical noise in a stacked spectrum), and I_{MOD} is the (extended MILES; MIUSCAT) model line strength, with MOD being either $1SSP$ or $2SSP$ (see below). The minimization is performed with respect to the model parameters, and for each stack, both observed and model indices are computed at the nominal resolution (SDSS plus σ_0) of a given stacked spectrum. Three different models are considered, namely:

1 SSP – The model parameters are the age and metallicity of a single extended MILES (MIUSCAT) SSP. As de-

[16] Notice that while some difference between models can be expected because different conventions for metallicity are adopted (i.e. either [Fe/H] or $[Z/H]$), large differences also exist between models adopting the same definition of metallicity (i.e. TMJ11 vs. CER07, and CvD12 vs. COE07).

[17] Neither TMJ11 nor CER07 models have the wavelength coverage required to compute Na8190$_{\rm SDSS}$. This is not the case for COE07 synthetic models, but for these models the equivalent width of Na8190$_{\rm SDSS}$ turns out to be negative, in contrast to observations.

[18] For instance, using CvD12 models, one finds that the equivalent width of Mg4780 decreases as $[C/Fe]$ increases, showing an opposite behaviour to [Mg/Fe].

[19] The fact that we do not see an opposite behaviour among $[Z_{Mg}/Z_{Fe}]$ slopes of CaT and Na indices at high σ_0 argues against a picture whereby abundance ratios, rather than IMF, drive variations of Na and Ca line strengths.

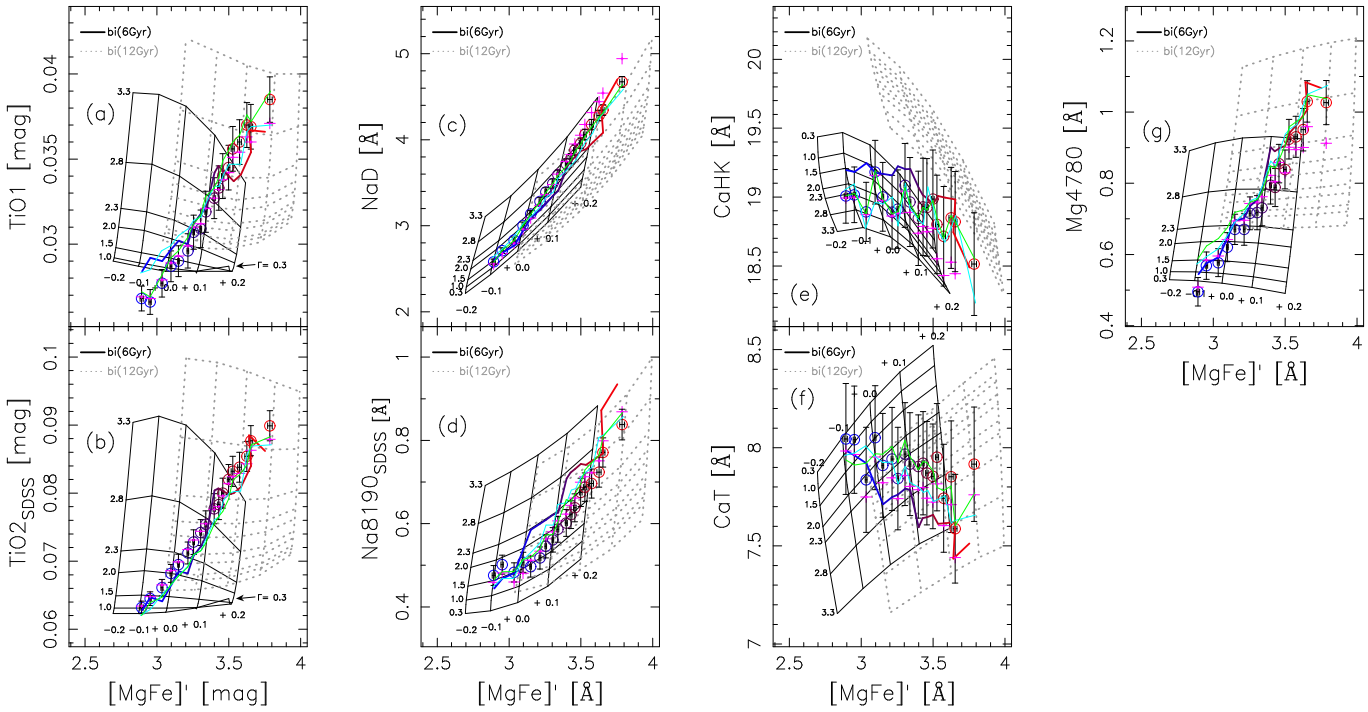

Figure 11. Same as Fig. 10, but for IMF- and abundance-sensitive spectral indices. Black and grey grids show the effect of changing IMF slope and metallicity, for two SSPs, with "young" (6 Gyr) and "old" (12 Gyr) age, respectively (see upper-left corner of each panel). Error bars are $1\,\sigma$ uncertainties (including measurement errors and $[Z_{Mg}/Z_{Fe}]$ correction uncertainties). Open circles plot the line strengths of the 18 σ_0 stacks corrected to a common resolution of 200 km s^{-1}, and solar abundance ($[Z_{Mg}/Z_{Fe}]$=0). For reference, magenta crosses show line strengths when no abundance correction is applied.

scribed in Sec. 3, we consider SSPs covering a wide range of (200×150) ages and metallicities. Eq. 2 is minimized over the grid for each value of Γ, and then, for a given choice of the IMF (i.e. bimodal or unimodal), the value of Γ giving the minimum χ^2 is selected. The procedure is repeated by shifting indices according to their uncertainties (σ_I and s_I), resulting in a PDF (probability distribution function) for Γ (marginalized in age and metallicity). For the 1SSP fits, we exclude Hγ_F from the fitting, for reasons explained in Sec. 7.1.

2 SSPs – The models consists of a linear combination of two extended MILES (MIUSCAT) SSPs, having the same IMF, but different ages and metallicities. The five model parameters are the ages and metallicities of the 2 SSPs plus a mass fraction giving their relative contribution to the linear combination. The minimization is performed by varying the ages and metallicities of the two populations independently, over the same grid as for 1SSP. Since the 2SSP fitting procedure involves a much larger volume of parameter space, we do not iterate the procedure to estimate uncertainties. Instead, we weight each linear combination by $\exp(-\chi^2/2)$, generating a PDF for Γ (marginalized over all other fitting parameters).

2 SSPs+X/Fe – The models consist of 2SSP (five free parameters), plus three free parameters describing the abundances of calcium, sodium, and titanium ([Ca/Fe], [Na/Fe], and [Ti/Fe], respectively). In practice, we replace I_{MOD} in Eq. 2 with $I_{2SSP+X/Fe} = I_{2SSP} - \delta_X \cdot [X/Fe]$, where $\delta_X = \delta(I)/\delta([X/Fe])$ is the sensitivity of a given index to a variation in the abundance of element X. Uncertainties on each fitting parameter (and Γ) are computed as for the 2SSP fits, marginalizing the PDF over all the other fitting parameters. For each index, we consider only the contribution from the dominant element the index is expected to be sensitive to, i.e. [Ca/Fe] for CaHK and CaT, [Na/Fe] for NaD and Na8190$_{\rm SDSS}$, and [Ti/Fe] for TiO1 and TiO2. For a given stacked spectrum (i.e. σ_0 bin), we compute the corresponding δ_X's by using the publicly available CvD12 models with varying abundance ratios. These models, having a Chabrier IMF, [Fe/H] = 0, and an age of 13.5 Gyr, are smoothed to match $\sigma = 200$ km s^{-1} (i.e. the average σ_0 of our stacks) plus the SDSS resolution. Varying the velocity dispersion in the smoothing does not change significantly the δ_X estimates. In Sec. 7.3, we compare the δ_X estimates from CvD12 models with estimates from some simple SSPs we create by using different synthesis ingredients from CvD12 (see App. D), finding good consistency. Using CvD12 models, we have explored the sensitivity of spectral indices to the abundance of several individual elements (Ca, C, Mg, Na, N, Si, Ti), by estimating the variation of each index (with respect to the solar scale) caused by a factor of two change in the abundance of each element. All selected indices are found to be at least three times more sensitive to the dominant, than any other, element. For TiO1, TiO2, and NaD, the choice of a given element as the dominant one is also consistent with the response of Lick indices to single element abundance ratios, as reported by Johansson et al. (2012, see their fig. 1). Notice that the dominant element of Mg4780 is Mg. Since the $[Z_{Mg}/Z_{Fe}]$ should reflect directly the Mg abundance, and the indices of our stacks are corrected to $[Z_{Mg}/Z_{Fe}]$= 0, we

do not consider the effect of a residual [Mg/Fe] variation in the 2SSP+X/Fe fits.

7 FITTING RESULTS

Figs. 10 and 11 compare observed and best-fitting spectral indices for different fitting methods, i.e. $1SSP$, $2SSP$, and $2SSP + X/Fe$ models (blue-through-red, cyan, and green curves, respectively). Fig. 10 plots the main age- and metallicity-sensitive indicators, H$\beta_{\rm o}$, H$\gamma_{\rm F}$, and [MgFe]$'$, while Fig. 11 shows abundance- and IMF-sensitive indices. The measured spectral indices, corrected to $[Z_{Mg}/Z_{Fe}]= 0$ and reported to a common resolution [20] of $\sigma_0 = 200$ km s^{-1}, are plotted as blue-through-red circles. All indices are plotted as a function of [MgFe]$'$ (proxy of total metallicity). For each panel in the Figures, the grids correspond to single SSP models, with varying age, metallicity, and bimodal IMF slope, as labelled. The effect of $[Z_{Mg}/Z_{Fe}]$ corrections is illustrated by the magenta crosses, showing line strengths when no correction is applied. The corrections are generally mild, shifting data-points (i.e. blue-through-red relative to magenta symbols) within error bars, with the main exception of NaD (see Fig. 11), where the shift at high σ_0, towards lower equivalent widths, is significant at more than the $3\,\sigma$ level.

To compare the fitting quality among different σ_0 bins and different fitting methods, we report in Tab. 5, for each fit, the reduced chi-squared statistics, χ^2_ν, and the probability, $P_{\geqslant\chi^2_\nu}$, for the χ^2_ν to be larger than the observed value, given the number of degrees of freedom (ν, with $\nu = 7$, 5, and 2, for $1SSP$, $2SSP$, and $2SSP + X/Fe$, respectively). By definition, lower values of $P_{\geqslant\chi^2_\nu}$ imply less likely best-fitting solutions, with $P_{\geqslant\chi^2_\nu} < 5\%$ representing a rejection at more than the $2\,\sigma$ level for a random normal deviate. In practice, because the models may present small systematic deviations with respect to the data, independent of the relevant stellar population properties (age, metallicity, and IMF), we mainly use the $P_{\geqslant\chi^2}$ in a relative sense here, i.e. to compare different σ_0 bins and different methods, as detailed below. We notice that in addition to constraining the IMF slope, different fitting models also give information about the stellar population content (i.e. age and metallicity) of ETGs as a function of σ_0. Since our main focus here is that of the stellar IMF, in the following sections we only discuss some general features of the stellar population properties inferred from different fitting schemes, postponing a more detailed analysis to a future paper.

In Secs. 7.1, 7.2, and 7.3 we present the results obtained for $1SSP$, $2SSP$, and $2SSP + X/Fe$ models, assuming bimodal IMF models. The case of unimodal IMFs is considered in Sec. 7.4, while Sec. 7.5 presents results of the hybrid approach.

[20] The correction to $\sigma_0 = 200$ km s^{-1} is performed by computing best-fitting $1SSP$ indices at the actual resolution of a given stack and the reference resolution of $\sigma_0 = 200$ km s^{-1}. The correction is given by the corresponding difference of line strength values.

7.1 Bimodal IMFs – $1SSP$ fits

Overall, single SSPs reproduce fairly well the relative trends of H$\beta_{\rm o}$, [MgFe]$'$, IMF- and abundance-sensitive spectral indices as a function of σ_0. As seen from the H$\beta_{\rm o}$ vs. [MgFe]$'$ plot (panel a of Fig. 10), $1SSP$ fits yield older ages and higher metallicities with increasing velocity dispersion, in agreement with previous work (e.g. Gallazzi et al. 2006). The IMF slope, Γ, is found to increase, becoming more bottom-heavy at high σ_0. This is shown in Fig. 12 (top panel), where we plot the best-fitting Γ, for bi-modal IMFs, as a function of σ_0, with the same colour coding, for different σ_0 bins, as in Fig. 10. The $1SSP$ best-fitting Γ increases from ~ 1.4 (i.e. a Kroupa-like slope) at $\sigma_0 \sim 100$ km s^{-1} to ~ 3 at $\sigma_0 \sim 300$ km s^{-1}. This IMF trend is consistent with that derived in our previous work (see fig. 4 of FLD13), where we adopted a smaller set of spectral indices, and a different approach to analyze the stacked spectra (see Sec. 7.5): we analyzed the stacks after smoothing all of them to the same σ_0 of 300 km s^{-1}(rather than keeping them at their original resolution), and no abundance ratio corrections were applied. To further test whether our results are affected by the different resolution of the stacks (see Sec. 4), we repeated the $1SSP$ analysis by measuring and fitting line indices after smoothing all spectra and models to 300 km/s, finding negligible differences ($< 10\,\%$) in the resulting values of Γ as a function of σ_0. Notice that, since H$\beta_{\rm o}$ slightly decreases with IMF slope (panel a of Fig. 10), a steeper slope for more massive ETGs implies them to have younger ages than expected from a Kroupa/Chabrier IMF. In particular, at highest σ_0, for $\Gamma = 2.8$, the highest σ_0 stacks turn out to have an age of ~ 11 Gyr, i.e. smaller than the age of the Universe, which is not the case when assuming a Kroupa/Chabrier IMF [21].

A thorough inspection of single panels in Fig. 11 reveals that for IMF- and abundance-sensitive indices some discrepancies exist, at the level of a few σ's, between models and observational data, namely

– at low (high) σ_0, the model line strength of TiO1 is higher (lower) than the data; i.e., the slope of the TiO1-[MgFe]$'$ relation is shallower for models than data (see panel a of Fig. 11);
– the model trend of TiO2$_{\rm SDSS}$ (panel b) is slightly offset downwards (by $\sim 1 - 1.5\,\sigma$) with respect to the data;
– at $\sigma_0 \sim 230$ km s^{-1} the $1SSP$ fits give too weak NaD (panel c);
– the Na8190$_{\rm SDSS}$ (panel d) is larger for models than data, for most σ_0 bins; the largest differences amounting to $\sim 3\,\sigma$, found for stacks at $\sigma_0 \sim 195$ and 270 km s^{-1};
– the CaT (panel f) tends to be weaker in models than data, for all stacks with $\sigma_0 > 130$ km s^{-1}; with the largest discrepancies at high σ_0, but comparable to the error bars.

Albeit small, all these discrepancies result into probabilities

[21] The fact that stellar population models predict ages larger than that of the Universe is known as the age zero-point issue. Although the problem might be solved with a bottom-heavy IMF for high-mass galaxies, it persists for globular clusters, where no evidence exists for a steepening of the IMF. Hence, the zero-point issue still remains as a fundamental aspect to deal with in the modelling of stellar population (e.g. Vazdekis et al. 2001; Schiavon et al. 2002)

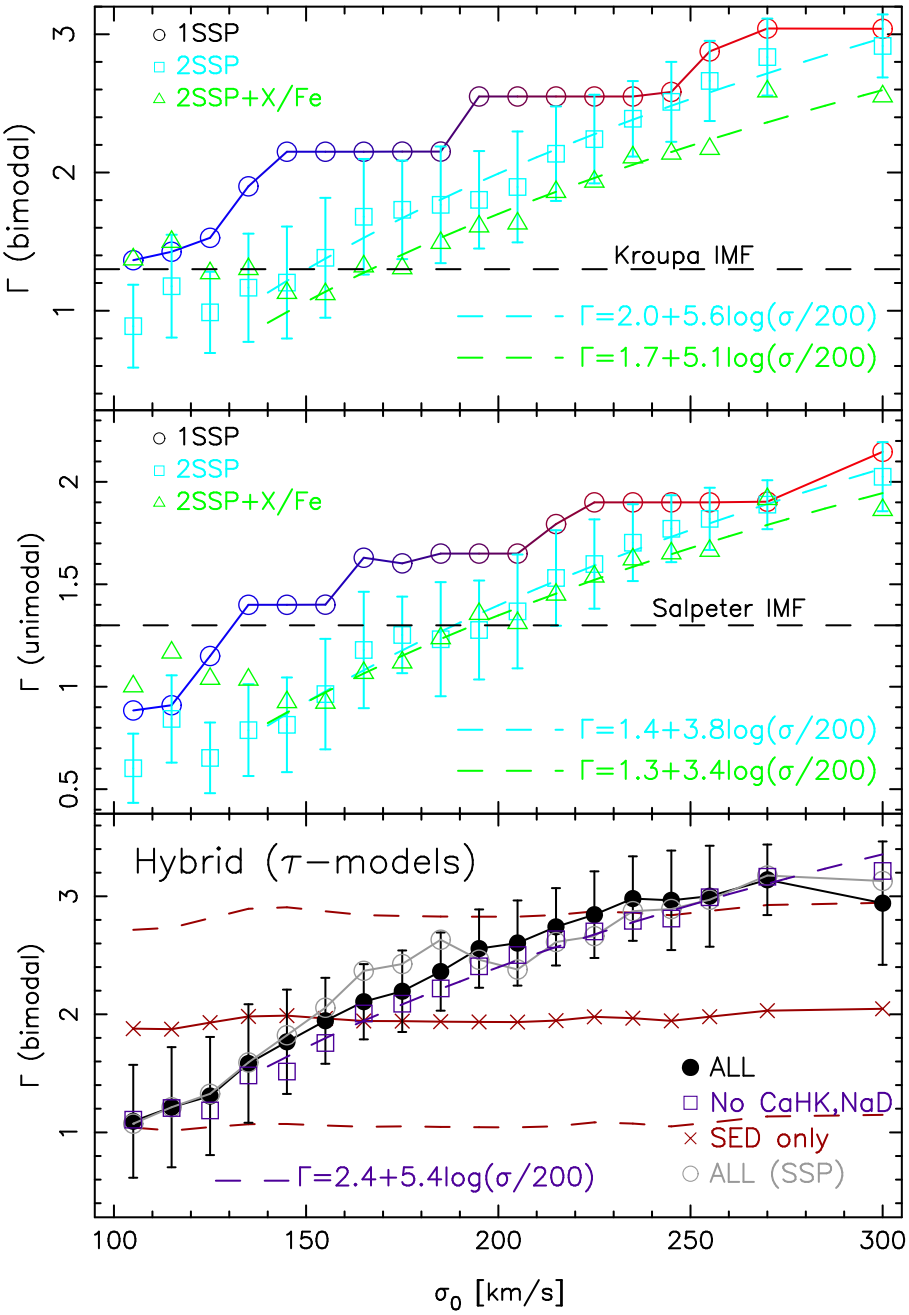

Figure 12. Best-fit slope of the IMF, Γ, from different methods and models, as a function of central velocity dispersion (σ_0). Top panel: best-fit slope of the bimodal IMF obtained by fitting spectral indices with $1SSP$, $2SSP$, and $2SSP + X/Fe$ models. Different symbols and colours correspond to the different models, as labelled in the top–left corner of the plot. The colours follow the same scheme as in Figs. 10 and 11. The error bars are given at the $1\,\sigma$ level, and are only shown for the $2SSP$ models for clarity. The horizontal dashed line marks the value of $\Gamma = 1.3$, corresponding to a Kroupa-like IMF. For $\sigma_0 > 140$ km s^{-1}, where a significant variation of Γ with σ_0 is detected, we also show the best-fit relations to the Γ–σ_0 trends as dashed curves, for $2SSP$ and $2SSP + X/Fe$ models, respectively. The best-fit relations are reported in the lower-right corner of the plot. Middle panel: same as top panel but for unimodal, rather than bimodal, IMFs. Notice that both bimodal and unimodal models lead to the similar conclusion of a systematic increase of IMF slope with central velocity dispersion (σ_0). The horizontal dashed line marks the value of $\Gamma = 1.3$, corresponding, for a unimodal IMF, to the Salpeter slope. Bottom panel: marginalized values of the (bimodal) IMF slope, obtained by our hybrid approach, with respect to velocity dispersion, including 1σ confidence levels. The joint method (SED fitting plus line strengths) for a grid of τ models is shown as black solid dots. The plot also shows the case for simple stellar populations (grey open dots) and for the τ model, where only the strongest IMF-sensitive line strengths are considered (Mg4780, TiO1, TiO2$_{\rm SDSS}$, Na8190$_{\rm SDSS}$, CaT). In this case, the best-fit relation to the Γ–σ_0 trend is also shown as a magenta, dashed, curve, for $\sigma_0 > 140$ km s^{-1}. For reference, the same analysis restricted to spectral fitting alone is given by the red crosses and dashed red lines (1σ level).

$P_{\geqslant\chi^2}$ smaller than a few percent for most (13) σ_0 stacks (see Tab. 5). The discrepancies tend to disappear for $2SSP$ models, as discussed in Sec. 7.2. Regarding Balmer lines, we remark that $1SSP$ fits include only Hβ_o, i.e. we do not include Hγ_F (see Sec. 6). When only using Hβ_o in the $1SSP$ fits, the predicted Hγ_F values are significantly smaller than the observations, as seen in panel (b) of Fig. 10. In other words, the $1SSP$ ages inferred from Hβ_o are older (by $\sim 1-2$ Gyr) than those derived from Hγ_F alone. The fact that different Balmer lines provide discrepant SSP-equivalent ages is a well-known issue, whose explanation might involve the stronger sensitivity of high-order (relative to Hβ) Balmer lines to (i) [α/Fe] (Thomas et al. 2004; Thomas & Davies 2006), (ii) single element abundance ratios (Serven & Worthey 2007), and (iii) fraction of young stars (Schiavon, Caldwell & Rose 2004; Serra & Trager 2007; Rogers et al. 2010). A detailed analysis of these issues is beyond the scope of the present paper, but we notice that using $2SSP$ models (Sec. 7.2) allows us to consistently match both Hβ_o and Hγ_F within error bars, indicating that a $1SSP$ model might be too simplistic to describe the data (although we note that the contribution from a second, young, component is not large either, see below).

7.2 Bimodal IMFs – $2SSP$ fits

For two SSP models, the fits improve significantly with respect to the $1SSP$ case, as seen by comparing cyan ($2SSP$) to blue-through-red ($1SSP$) curves in Figs. 10 and 11, and by the fact that they give larger $P_{\geqslant\chi^2}$ values than $1SSP$ models (see Tab. 5; with the exception of the lowest σ_0, see below). In particular, $2SSP$ models fit well the trends of both Hβ_o and Hγ_F with [MgFe]$'$, match TiO1 and NaD indices at high σ_0, give a better description of Na8190$_{SDSS}$ and on average reproduce better the trends of Ca indices with σ_0. On the other hand, some small discrepancies persist:

– at low σ_0 (< 150 km s^{-1}), the model predictions of TiO1 are still too high.
– a small ($\sim 1\,\sigma$) average offset remains in TiO2$_{SDSS}$, with models having weaker line strength than the data, as in the $1SSP$ case;
– the model Na8190$_{SDSS}$ is still too high with respect to the observations, but the average difference ($-0.9\,\sigma$) is significantly reduced with the use of two populations.

While part of the discrepancy in TiO2$_{SDSS}$ and that of TiO1 at low σ_0 might be explained by a varying [Ti/Fe] abundance ratio (see Sec. 7.3), differences between model and observed indices (e.g. Na8190$_{SDSS}$) might also have an intrinsic origin, reflecting subpercent-level uncertainties in stellar population models, and/or differences between the true shape of the IMF and that assumed in the present analysis (either bimodal or unimodal). We come back to the latter point in Sec. 7.4, when discussing the possibility of discriminating among different IMF shapes.

For what concerns stellar population parameters, for all σ_0 bins, the $2SSP$ best-fit models consist of an old ($11-14$ Gyr), and a younger population, the latter contributing by less than 25% (in light) to the mixture [22]. Both $1SSP$ and $2SSP$ fits consistently suggest a significant variation of IMF slope with velocity dispersion. The $2SSP$ best-fit Γ changes from ~ 1 at $\sigma_0 < 150$ km s^{-1} to ~ 2.9 at $\sigma_0 < 300$ km s^{-1} (see top panel of Fig. 12). The shape of the Γ–σ_0 relation differs significantly between $1SSP$ and $2SSP$ fitting schemes, with $1SSP$ models exhibiting a faster increase with σ_0 towards a bottom-heavy IMF for more massive systems. At $\sigma_0 \sim 200$ km s^{-1}, the $2SSP$ best-fit Γ is ~ 1.6, while $1SSP$ models give $\Gamma \sim 2.6$. On the other hand, at $\sigma_0 > 250$ km s^{-1}, both $2SSP$ and $1SSP$ models give compatible values for Γ within error bars. At low σ_0, spectral indices are less sensitive to variations in the IMF slope, as seen from the shape of the grids in Fig. 11, hence the larger difference of model predictions for Γ between $1SSP$ and $2SSP$ fits. The adoption of different stellar population mixtures will therefore affect significantly the inferred Γ values in this regime. In contrast, at high Γ (i.e. σ_0), spectral indices are strongly sensitive to IMF variations, and the constraints on Γ appear more robust with respect to the other stellar population ingredients. In summary, for the purpose of the present work, the main conclusion here is that $2SSP$ models plus a varying IMF reproduce well the variation of all spectral indices with σ_0, and the quality of the fits does not change significantly with σ_0, as proven by comparing $P_{\geqslant\chi^2}$ values among different σ_0 bins (see Tab. 5), with the exception of the three lowest σ_0 bins ($\leqslant 130$ km s^{-1}), where a small variation of single element abundances might be required (see Sec. 7.3).

Following our previous work (FLD13), we model the trend of Γ with σ_0 with the relation:

$$\Gamma = A + B\log(\sigma_0[\mathrm{km/s}]/200), \quad (3)$$

where A and B are obtained by a least-squares fitting procedure to the data, with Γ as dependent variable in the fit. The uncertainties on A and B are bootstrap errors, reflecting the uncertainties on Γ. Notice that the fit is restricted to stacks with $\sigma_0 > 140$ km s^{-1}, where a significant variation of IMF slope with velocity dispersion is detected. The values of A and B, for $2SSP$ as well as for other fitting methods, are summarized in Tab. 4. Notice that, considering the quoted errors, the $2SSP$ best-fitting value of B (5.4 ± 0.9) is larger than zero at a 6σ level, reflecting the fact that our data strongly support an increase of IMF slope with velocity dispersion in ETGs.

Fig. 13 shows, in wavelength, rather than index–index, space, the main conclusion of the present work, namely that high-mass ETGs are on average better fit by an IMF that is more bottom heavy than the standard Kroupa-like case. The Figure compares the stacked spectrum at $\sigma_0 \sim 270$ km s^{-1} with the best-fitting $2SSP$ model (blue) and a $2SSP$ best-fitting model obtained by assuming a $\Gamma \sim 1$ IMF, the latter being representative of low-mass ETGs (see top panel of Fig. 12). The comparison is shown for different spectral windows where IMF- and abundance-sensitive spectral indices

[22] We notice that the young component is about 2 Gyr old only for the two stacks with $\sigma_0 \leqslant 120$ km s^{-1}, while in the other cases, excluding the highest σ_0 bin, it is older than ~ 3 Gyr. At the highest σ_0 (~ 300 km s^{-1}), the young component is 1 Gyr old, but this contributes negligibly, by less than 1%, to the mixture.

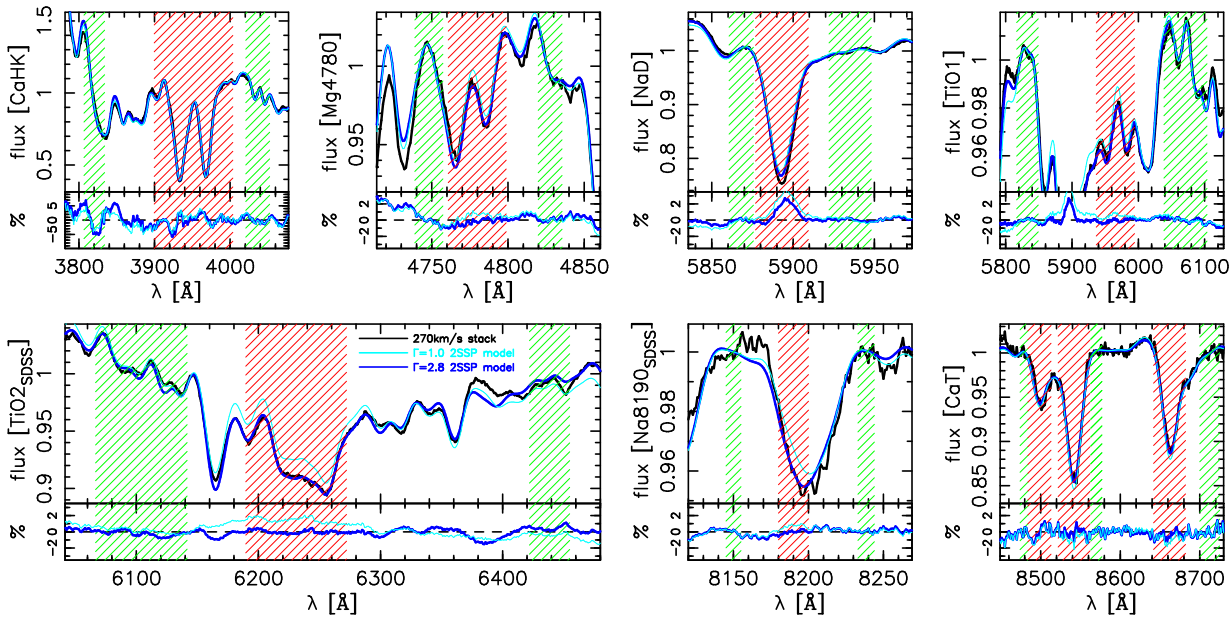

Figure 13. Comparison of the $\sigma_0 = 260 - 280$ km s^{-1} stacked spectrum to $2SSP$ best-fitting models with bimodal IMF $\Gamma = 1$ (Kroupa-like; cyan) and $\Gamma = 2.8$ (bottom-heavy). The six panels correspond to spectral regions of IMF- and abundance-sensitive spectral indices. Hatched green and red regions mark the sidebands and central features of spectral indices. For each plot, the upper panel plots the observed spectrum and models, while the lower panel shows relative residuals (in percent) after subtracting the model from the data. For each spectral region, but CaT, models and data have been normalized by linear fitting the median fluxes in the sidebands. For CaT the normalization is obtained by fitting a second order polynomial to the pseudo-continua of the three Ca features. Notice that a bottom-heavy IMF clearly provides a better fit to the data for all selected spectral regions.

Table 4. Best-fit coefficients, A and B, of the relation between IMF slope (Γ) and $\log\sigma_0$ (Eq. 3) for different methods used to constrain the Γ. Uncertainties are quoted at the 1σ level.

method (1)	A (2)	B (3)
bimodal, $2SSP$	2.0 ± 0.1	5.6 ± 0.9
bimodal, $2SSP + X/Fe$	1.7 ± 0.1	5.1 ± 0.9
unimodal, $2SSP$	1.4 ± 0.1	3.8 ± 0.6
unimodal, $2SSP + X/Fe$	1.3 ± 0.1	3.4 ± 0.6
bimodal, hybrid	2.4 ± 0.1	5.4 ± 0.9

are defined. Notice that a high Γ (~ 2.8) gives the best fit to all relevant features [23], i.e. Na and CaT lines, and in particular the observed spectrum in the TiO2$_{\rm SDSS}$ spectral range, making this feature an extremely useful tool to constrain the IMF (in agreement with STK12).

7.3 The role of individual abundance patterns

Comparing the cyan and green curves in Fig. 11, one can see that the overall quality of the fits to our targeted spectral indices does not improve significantly when allowing for an individual variation of Ca, Na, and Ti abundance patterns. In fact, for most σ_0 bins, the probability $P_{\geqslant\chi^2}$ values are *lower* for $2SSP + X/Fe$ than $2SSP$ models (see Tab. 5). On the other hand, looking at TiO features alone, one can notice an improvement with respect to the $2SSP$ case, in that $2SSP + X/Fe$ models match better TiO1 at the lowest σ_0 (< 150 km s^{-1}), as well as TiO2$_{\rm SDSS}$ at high σ_0 (in particular around 250 km s^{-1}). The improved matching of TiO1 is due to the fact that, according to CvD12 models [24], TiO1 is slightly more sensitive to [Ti/Fe] than TiO2$_{\rm SDSS}$. Hence, by lowering [Ti/Fe], one decreases the model TiO1 more than TiO2$_{\rm SDSS}$, allowing both observed indices to be matched simultaneously. This point is illustrated in Fig. 14, where the best-fit abundance ratios, [Ca/Fe], [Na/Fe], and [Ti/Fe] are shown as a function of σ_0. We point out that, since spectral indices have been corrected to $[Z_{Mg}/Z_{Fe}]= 0$ (see Sec. 5.2), the [Ca/Fe], [Na/Fe], and [Ti/Fe] estimates in Fig. 14 do not reflect true abundance ratios in different σ_0 bins, but should rather be interpreted as *residual* abundances, i.e. not accounted for by the correlation of single element abundances with [α/Fe], and the fact that [α/Fe] increases with σ_0. Another caveat is that we rely on a given set of *theoretical* models (CvD12) to infer [Ca/Fe], [Na/Fe], and [Ti/Fe], although we also explore the effect of using our own simple synthetic SSPs (see App. D) partly based on different ingredients to the CvD12 models (see below). For these reasons, our conclusions on individual abundance ratios should be considered on a qualitative basis.

[23] Notice that, in contrast to the indices, the observed spectrum in Fig. 13 is not corrected to solar-scale, which might explain some small discrepancies between models and data in the Figure (e.g., in the though of the NaD line).

[24] This different sensitivity of TiO1 and TiO2$_{\rm SDSS}$ to [Ti/Fe] is qualitatively consistent with the predictions of the TMJ11 models.

Table 5. Reduced chi-squared statistics, χ^2_ν, for all stacked spectra and the three fitting models ($1SSP$, $2SSP$, and $2SSP + X/Fe$) used to fit spectral indices in this work. The $P_{\geqslant\chi^2}$[%] bracket value is the probability to obtain a χ^2_ν larger than the measured one.

σ_0 range [km/s] (1)	$\chi^2_\nu(P_{\geqslant\chi^2}[\%])$ $1SSP$ (2)	$2SSP$ (3)	$2SSP + X/Fe$ (4)
100–110	2.1(8)	3.1(1)	5.1(1)
110–120	2.6(3)	2.0(7)	2.1(12)
120–130	2.0(11)	2.0(8)	3.4(3)
130–140	1.4(31)	1.2(31)	2.7(7)
140–150	2.8(2)	1.1(38)	2.2(11)
150–160	3.4(0)	1.5(19)	3.0(5)
160–170	2.9(1)	1.4(23)	1.8(16)
170–180	2.5(3)	1.6(17)	2.2(11)
180–190	2.7(2)	1.3(25)	2.5(8)
190–200	3.4(0)	1.3(27)	4.1(2)
200–210	2.8(2)	1.5(20)	2.2(11)
210–220	1.8(14)	1.6(17)	2.6(8)
220–230	1.7(18)	1.4(21)	3.3(4)
230–240	2.8(2)	1.3(28)	2.2(12)
240–250	3.3(1)	1.7(12)	2.6(8)
250–260	3.3(1)	1.5(17)	1.9(15)
260–280	1.9(12)	0.5(78)	1.6(21)
280–320	3.8(0)	1.9(9)	2.2(12)

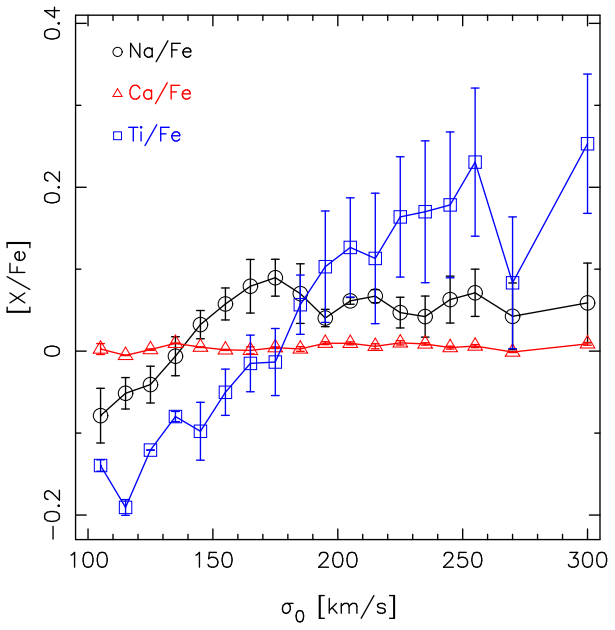

Figure 14. Best-fit "residual" calcium, sodium, and titanium abundances ([X/Fe] with X = Ca, Na, and Ti, respectively), as a function of central velocity dispersion (σ_0). Residual abundances refer to the fact that we have already corrected all spectral indices to [α/Fe]= 0 for each σ_0 bin. The [X/Fe]'s are obtained from the fitting of spectral indices with $2SSP$ extended MILES (MIUSCAT) synthetic populations, modelling the abundance sensitivity of different indices with the CvD12 models. Since the indices are corrected to $[Z_{Mg}/Z_{Fe}]$= 0, the [X/Fe]'s represent residual abundance patterns, not accounted for by the $[Z_{Mg}/Z_{Fe}]$ correction procedure. Error bars are quoted at the 1 σ level.

Ti abundances – The [Ti/Fe] is found to increase with σ_0, changing from negative (~ -0.2 dex) at the lowest σ_0 to positive for $\sigma_0 > 180$ km s^{-1}. Notice that at $\sigma_0 < 150$ km s^{-1}, the error bars for [Ti/Fe] are very small (less than a few percent), reflecting the fact that a negative value of [Ti/Fe] is required to reduce the discrepancy between model and observed TiO1 strength for the lowest velocity dispersion stacks. At high σ_0, the [Ti/Fe] becomes positive, as TiO2$_{\rm SDSS}$ increases, producing a better match to the observed TiO2$_{\rm SDSS}$. Notice, in fact, that [Ti/Fe] peaks at $\sigma_0 \sim 250$ km s^{-1} (Fig. 14), where the $2SSP$ models differ the most from the data (see panel *b* of Fig. 11). The error bars on [Ti/Fe] are large at $\sigma_0 \gtrsim 200$ km s^{-1}, meaning that a deviation of Ti abundance from solar scale is only marginally significant for massive systems.

Na abundances – The [Na/Fe] also increases with σ_0, varying by about 0.2 dex from $\sigma \sim 100$ to 300 km s^{-1}. This amount of variation is far smaller than that recently reported by CvD12b, who found that [Na/Fe] can be as high as $\sim$1 dex for ETGs in the SAURON sample. Notice that this is not necessarily in disagreement with our findings. In fact, the NaD feature is not covered by the observed spectra of CvD12b, with the [Na/Fe] being inferred indirectly by the authors because of its effect on the free electron pressure in stellar atmospheres. Also, as noticed above, our best-fit abundance ratios should be considered as residual (with respect to [α/Fe]), rather than absolute estimates. The effect of varying [Na/Fe] on Na indices is illustrated in Fig. 15 (top panel), where NaD is plotted against Na8190$_{\rm SDSS}$. We also show the expected effect of varying [Na/Fe] by +0.3 dex, when using (i) CvD12 models with a Chabrier IMF, solar metallicity, and an age of 13.5 Gyr (blue arrow); (ii) our synthetic SSP, with a Kroupa IMF, solar metallicity, and age of 12 Gyr (red arrow); (iii) the same SSP but for a Salpeter IMF (orange arrow). We refer the reader to App. D for details on how our synthetic SSPs are created. Notice the remarkable agreement between CvD12 and our-SSP predictions for a Chabrier/Kroupa IMF. Increasing [Na/Fe] makes both NaD and Na8190$_{\rm SDSS}$ to increase along a direction which is either steeper (Chabrier/Kroupa) or similar (Salpeter SSP) to the observed NaD–Na8190$_{\rm SDSS}$ trend. This indicates that disentangling the effect of IMF and [Na/Fe] is in general very difficult, and one actually needs a multi-index approach, based on indices from different species, as in the present work. We emphasize that a significant variation of [Na/Fe] with σ_0 alone (after correcting for the $[Z_{Mg}/Z_{Fe}]$ trends) appears to be ruled out by our data, as the $2SSP$ fits reproduce well the NaD–Na8190$_{\rm SDSS}$ trend, as well as the other index-σ_0 trends.

Ca abundances – The best-fit [Ca/Fe] is very close to zero for all stacks, with small error bars throughout the full σ_0 range. The reason of this behaviour is illustrated in Fig. 15 (bottom panel), where CaHK is plotted as a function of CaT. The effect of decreasing Ca abundance by a "small" amount (-0.05 dex) is shown by the blue (CvD12), red (our-SSP, Kroupa IMF), and orange (our-SSP, Salpeter IMF) arrows. Notice that in contrast to [Na/Fe], Chabrier CvD12 models and our simple synthetic SSP with Kroupa IMF do agree only in a qualitative way, in that the $[Ca/Fe]$ variation produces a strong change in CaHK and only a minor change to CaT (especially in the case of a Salpeter model). However, regardless of the prescription, the arrows show that even a

small change in [Ca/Fe] would bring the model indices away from the locus occupied by the observations. Therefore, since the extended MILES (MIUSCAT) base models match well the CaHK and CaT grid, with CaHK being significantly sensitive to $[Ca/Fe]$, there is not much space left for a *residual* deviation of Ca abundance from solar scale.

We point out that the present analysis considers only the effect of [Ca/Fe], [Na/Fe], and [Ti/Fe] abundance ratios, as these are expected to dominate the contribution to our targeted IMF-sensitive spectral indices (see Sec. 6). While other elements may contribute to the line strengths [25], our main conclusion here is that, after removing the effect of the [α/Fe] increase with velocity dispersion, a variety of IMF-sensitive spectral indices from different species (Ca, Na, Ti, and Mg) can all be recovered simultaneously with (nearly) solar-scaled models, by invoking a variation of the IMF to become increasingly bottom-heavy with velocity dispersion. The best-fitting coefficients of the Γ–σ_0 relation (Eq. 3), for $2SSP + X/Fe$ models with bimodal IMF, are reported in Tab. 3. Notice the fair agreement of fitting coefficients between $2SSP$ and $2SSP + X/Fe$'s models.

7.3.1 The case of Ca4227

An important caveat related to Ca-sensitive indices is that, as anticipated in Sec. 4, we have not been able to include the Ca4227 index in the present analysis. The reason for that is illustrated in Fig. 16, where we plot Ca4227r as a function of CaT. The Ca4227r is a modified version of Ca4227, that avoids the contamination of the blue sideband of Ca4227 from the CN4216 molecular band (Prochaska, Rose & Schiavon 2005). Both Ca4227r and CaT have been corrected for the index–$[Z_{Mg}/Z_{Fe}]$ correlation at fixed σ_0, as discussed in Sec. 5.2. The Ca4227r decreases with $[Z_{Mg}/Z_{Fe}]$ as seen by the fact that uncorrected data-points in the Figure (magenta relative to blue-through-red symbols) have weaker Ca4227r. All models ($1SSP$, $2SSP$, and $2SSP + X/Fe$) give Ca4227r EWs too large with respect to the data, the discrepancy being larger for more massive systems. Including Ca4227r in the fitting procedure would not solve the discrepancy, implying no significant change to the IMF trend with σ_0 (top panel of Fig. 12). The Ca4227 discrepancy is a well-known issue of stellar population studies, the origin of which has been extensively debated (see, e.g., Vazdekis et al. 1997; Thomas et al. 2003b; Yamada et al. 2006). As recently claimed by Johansson et al. (2012), Ca4227 EWs would be explained by the fact that Ca is underabundant in ETGs with respect to Mg, following more closely the Fe abundance. Using CaHK, Worthey, Ingermann & Serven (2011) concluded, indeed, that both [Ca/Fe] and [Ca/Mg] systematically decrease with increasing elliptical galaxy mass. While our [α/Fe] corrections to Ca indices seem to support this claim (as Ca indices decrease, at fixed σ_0, with $[Z_{Mg}/Z_{Fe}]$), Fig. 15 (bottom panel) and Fig. 16 indicate that the discrepancy remains unresolved. In fact, changing $[Ca/Fe]$ abundance would shift the models in a direction orthogonal to the sequence of data-points in the Ca4227r-CaT diagram

[25] For instance, Worthey (1998) raised the issue that TiO indices might also be sensitive to elements lighter than Ti, like Sc and V.

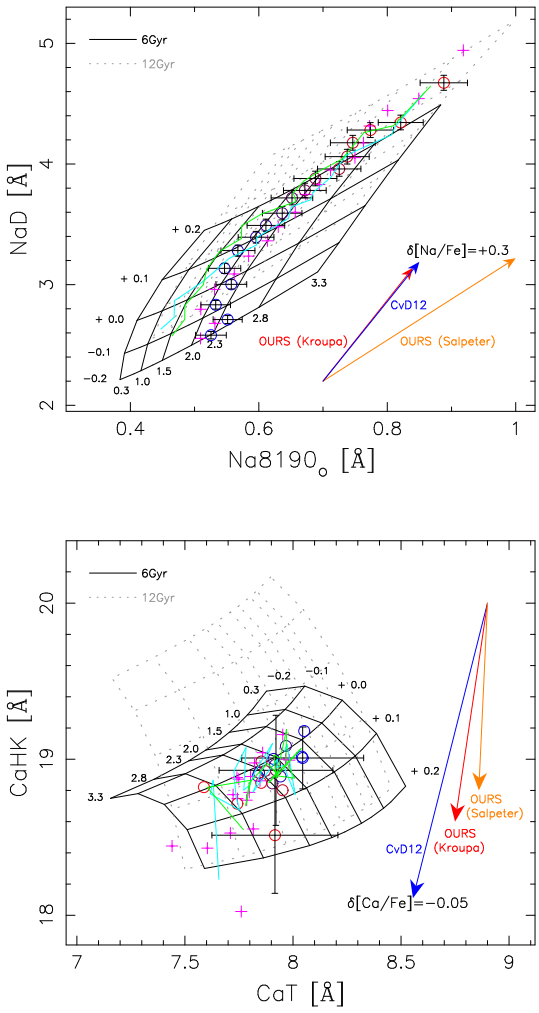

Figure 15. Plots of abundance- vs. IMF-sensitive spectral indices. The top panel shows Na-sensitive indices, i.e. NaD vs. Na8190$_{\rm SDSS}$, while the bottom panel shows Ca-sensitive indices, CaHK vs. CaT. Only results from $2SSP$ and $2SSP + X/Fe$ fits are shown, as cyan and green curves, respectively. Symbols are the same as in Figs. 10 and 11. The blue arrows show the effect of changing [Na/Fe] by +0.3 dex (top) and [Ca/Fe] by −0.05 dex according to CvD12 models. Error bars are shown only for stacks with $\sigma_0 \sim 100$, 200, and 300 km s^{-1}, respectively.

(see blue arrow in Fig. 16), and would also not fit the CaHK-CaT diagram. Furthermore, our simple SSPs indicate that for an IMF more bottom-heavy than the standard Kroupa/Chabrier (i.e. a Salpeter IMF; see orange arrow in the Figure) the effect of [Ca/Fe] abundance on Ca4227r becomes really minor, further hampering the explanation of the discrepancy between models and data for this feature. We notice that, while understanding the origin of the Ca4227r discrepancy goes certainly beyond the scope of the present study, to our knowledge, this is the first time that such a discrepancy is shown for spectral data with exceptionally high S/N ratio, allowed by the stacking of a large sample of SDSS spectra.

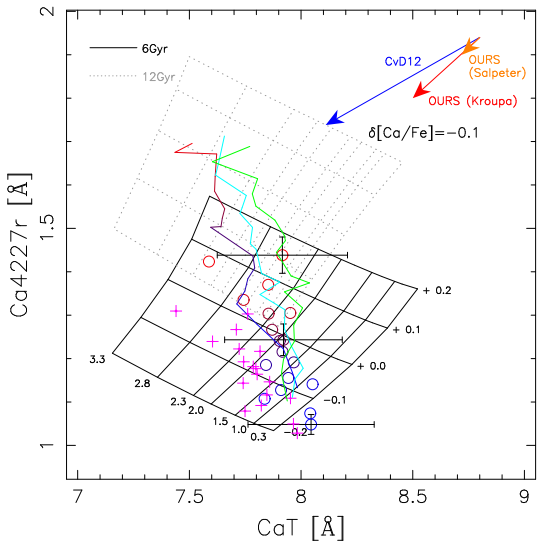

Figure 16. Same as the lower panel of Fig. 15 for the Ca4227r index as a function of CaT. The arrows show the effect of a change in [Ca/Fe] by −0.1 dex, rather than −0.05 dex, as in Fig. 15, for displaying purposes.

7.4 Unimodal vs. bimodal IMFs

Figs. 17 and 18 plot the results of fitting spectral indices with unimodal (i.e. single power law) IMF models. The corresponding IMF slope–σ_0 trends are shown in Fig. 12 (middle panel), with the best-fitting coefficients of the Γ–σ_0 relation (Eq. 3) given in Tab. 3. As explained in Sec. 3, we have limited the range of unimodal slopes to $\Gamma \leqslant 2.3$. Indeed, the trends of Γ with σ_0 show that higher values of Γ are not required to describe the data with single-slope IMFs.

Unimodal models provide a good fit to spectral indices, similar to bimodal IMFs. In particular, $2SSP$ fits match well all selected spectral indices. At $\sigma_0 \lesssim 150$ km s^{-1}, the models give too high values of TiO1 with respect to the observations, both for $1SSP$ and $2SSP$ models, as in the case with a bimodal IMF. The discrepancy disappears when including the effect of single element abundance ratios, with [Ti/Fe] being more negative in lower mass galaxies. Indeed, the individual trends we find for [Ca/Fe], [Na/Fe], and [Ti/Fe], vs. σ_0 are very similar to the bimodal case, with small deviations from solar scale.

Unimodal models also feature a clear tendency for the IMF slope to increase with velocity dispersion, the best-fitting slope in Eq. 3 differing from zero at more than 6σ (see Tab. 4). However, the amount of variation is different from the bimodal case: Γ ranges from ~ 0.7 to 2 for a single-slope IMF, whereas best-fit bimodal IMF slopes vary from ~ 1 to 3. In fact, for $2SSP$ models, the best-fitting slope of the Γ–σ_0 relation changes from ~ 5.6 for bimodal to ~ 3.8 for unimodal IMF. This difference arises from the fact that – at a given Γ – unimodal and bimodal IMFs are characterized by a different fraction of high- to low-mass stars, and thus the Γ has a different physical meaning for unimodal and bimodal models. Fig. 19 illustrates this point, where, instead of Γ we use the mass fraction in stars with masses below some threshold, as a function of velocity dispersion. This mass fraction is given at "time zero", by using the given functional form of the IMF over the stellar mass range from 0.1 to 100 $M_\odot$ (as in Vazdekis et al. 1996). At a given σ_0, we use the Γ value corresponding to the $2SSP$ best-fit models to determine the mass fraction. Two cases are considered, corresponding to a threshold of 0.5 and 0.75 $M_\odot$, respectively. The mass fractions agree pretty well between unimodal and bimodal IMFs. In particular, for $M/M_\odot < 0.5$, the agreement is better than 10%, proving that mass fractions are robustly constrained regardless of the adopted IMF shape. For $M/M_\odot < 0.5$, the trends in the initial mass fraction for both unimodal and bimodal models can be described by the following relation:

$$\text{Fraction}(<0.5M_\odot) \equiv \frac{\int_{0.1M_\odot}^{0.5M_\odot} M\Phi(M)dM}{\int_{0.1M_\odot}^{100M_\odot} M\Phi(M)dM} = \\ = 0.49 + 1.86\log(\sigma_0[\text{km/s}]/200), \quad (4)$$

where $\Phi(M)$ is the IMF. The coefficients are obtained by fitting simultaneously both trends, for stacks with $\sigma_0 > 140$ km s^{-1}(i.e. the range where a significant variation of Γ with σ_0 is detected, see Fig. 12). Eq. 4 is plotted in Fig. 19 as a dot-dashed curve. From Fig. 19 we conclude that the initial stellar mass fraction in low-mass stars ($M/M_\odot < 0.5$) increases systematically in ETGs, from $\sim$ 20% at $\sigma_0 \sim 100$ km s^{-1} to $\sim$ 80% at $\sigma_0 \sim 300$ km s^{-1}.

7.5 Hybrid approach

So far, the analysis is based on equivalent widths alone, to constrain *both* the IMF slope, Γ, and the distribution of stellar ages and metallicities. As an additional test, we define a complementary probability distribution function based on spectral fitting, and we combine this information with our targeted IMF-sensitive line strengths, following a method analogous to the one described in FLD13. Furthermore, we consider here the effect of a more complex distribution of stellar ages and metallicities, by adopting a standard exponentially decaying star formation rate (i.e. a τ-model), where a star formation history is described by four parameters: formation epoch, exponential timescale, metallicity (kept fixed for each individual model), and IMF slope, where the bimodal function is chosen. Table 6 shows the range in parameters. For each stack, we explore a grid of $32\times32\times10\times6$ models, defining two independent PDFs from the constraints on either spectral fitting or line strengths (we use in this analysis CaHK, Mg4780, NaD, TiO1, TiO2$_{\rm SDSS}$, Na8190$_{\rm SDSS}$, and CaT). We apply the same corrections for [α/Fe] as in the rest of the paper. The final PDF is given by the product of the individual PDFs, enabling us to combine spectral fitting, to constrain the age and metallicity distribution, and individual line strengths, to target the IMF slope.

The spectral fit is performed over the 3900 − 5400 Å range [26], after convolving the synthetic spectra, from the original 2.51 Å resolution of the extended MILES (MIUSCAT) models, to a velocity dispersion of 300 km s^{-1} (i.e. the

[26] In contrast to Sec. 5.1, where we adopt an upper limit of 7350 Å, the value of 5400 Å is chosen here to avoid several features, like TiO molecular bands and NaD, which are already taken into account as line strength constraints.

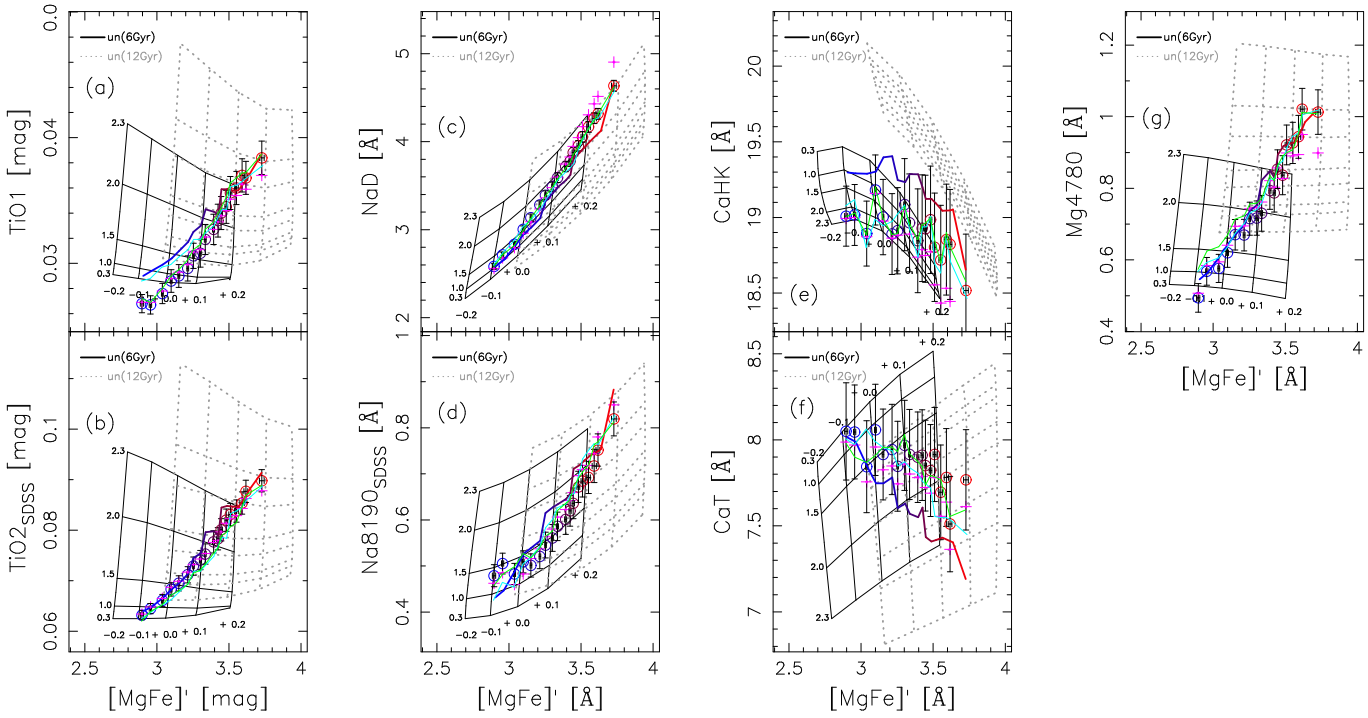

Figure 18. Same as Fig. 11, but for unimodal, rather than bimodal, IMF models. Notice that only models with unimodal $\Gamma \leqslant 2.3$ are considered, as explained in Sec. 3.

Table 6. Parameters used in the hybrid method (τ-model)

Parameter	Steps	Range	Description
$t_{\rm FOR}$	32	$0.1 \cdots tU^{\star}$	Formation Epoch
τ (Gyr)	32	$-1 \cdots +0.7$	Exponential timescale
$[Z/H]$	6	$-1.7 \cdots +0.22$	Metallicity
Γ	10	$0.3 \cdots 3.3$	IMF slope (bimodal)

$\star$ t_U is the current ($z = 0$) age of the Universe, i.e. 13.5 Gyr for a vanilla flavoured ($\Omega = 0.3$; $H_0 = 70\,{\rm km\,s^{-1}\,Mpc^{-1}}$) ΛCDM cosmology.

maximum value of σ_0 for stacked spectra), plus the SDSS spectral resolution. We avoid extending the fit over a wider range of wavelengths to minimise the effect of flux calibration systematics. Our results do not change significantly if a smaller spectral window is used, but it is important to include in the fitting range the region around the 4000 Å break for an effective constraint on the stellar ages. The bottom panel of Fig. 12 shows the best fit values of the IMF bimodal slope with respect to velocity dispersion, including $1\,\sigma$ error bars. In addition to the general model (black solid dots), we include, for reference, the constraints when only using the SED fit (red crosses), illustrating the expected complete degeneracy. The magenta open squares give the results when only using the targeted IMF-sensitive line strengths (i.e. Mg4780, TiO1, TiO2$_{\rm SDSS}$, Na8190$_{\rm SDSS}$, and CaT). Finally, the full hybrid analysis is also shown for models comprising only simple stellar populations (i.e a single age and metallicity), as open grey dots. The figure confirms that our previous results are robust with respect to more complex distributions of stellar ages and metallicities. In particular, fitting Eq. 3 to the Γ–σ_0 trend, when only using the targeted IMF-sensitive line strengths (magenta dashed curve in the bottom panel of Fig. 12), we find consistent results to the $2SSP$ fits of line strengths alone (see the values of best-fitting coefficients in Tab. 4). Also, the results of the hybrid approach can be compared to those of our previous work (FLD13), where we used the same hybrid approach to constrain the Γ, but with a smaller set of spectral indices, no correction for abundance ratio at fixed σ_0, and we did not optimize the definition of TiO and Na indices. In FLD13, we reported a Γ–σ_0 slope of $B = 7.2$, consistent with that of 5.4 ± 0.9 found here (Tab. 4). On the other hand, the offset of the Γ–σ relation reported by FLD13 ($B \sim 1.85$), is shallower than that of 2.4 ± 0.1 derived here from the hybrid approach, but fully consistent with that we derive from the $2SSP$ analysis ($B = 2.0 \pm 0.1$, see Tab. 4).

Fig. 20 shows jointly and independently the constraining power of spectral fitting (SED) and line strength fitting (EWs). From top to bottom, the panels give the probability distribution function with respect to stellar age, metallicity, and IMF slope, for two different stacks, corresponding to a velocity dispersion of $\sigma_0 = 150$ km s^{-1} (dashed line) and 300 km s^{-1} (solid line). The figure shows that an analysis based exclusively on line strengths cannot discriminate between the different age distributions of galaxies with different velocity dispersion. Notice in the hybrid method we only use the IMF-sensitive indices, since the spectral fitting substitutes the age- and metallicity-sensitive indices: H$\beta_{\rm o}$,H$\gamma_{\rm F}$ and [MgFe]$'$. In contrast, differences in IMF slope cannot be distinguished between these two stacks when using spectral fitting alone. It is the combination of the two that enables us to obtain strong constraints on Γ, that are complemen-

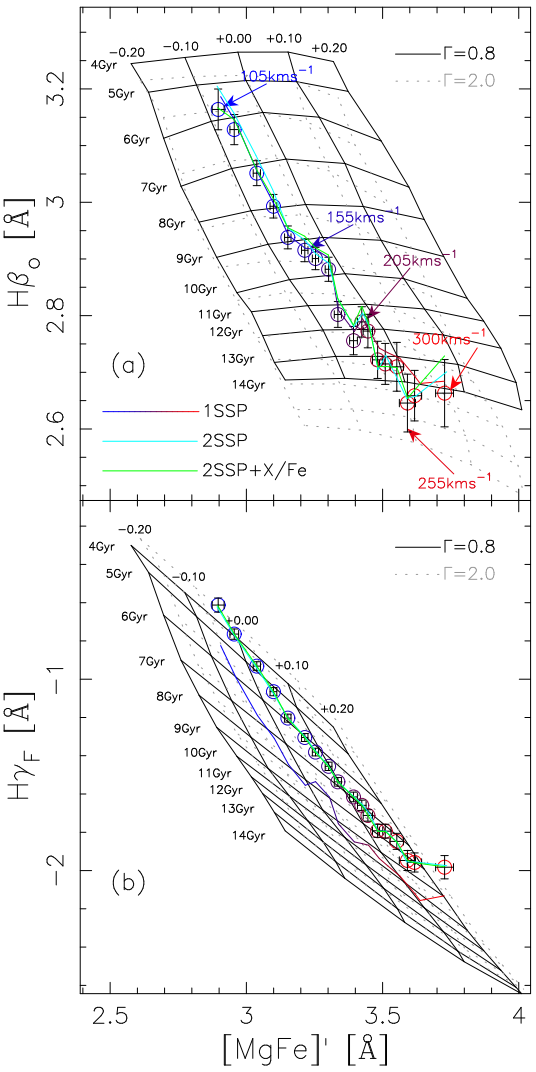

Figure 17. Same as Fig. 10, for unimodal, rather than bimodal, IMF models. Notice that only models with unimodal $\Gamma \leqslant 2.3$ are considered, as explained in Sec. 3.

tary to our previous analysis, only based on spectral lines. The hybrid method confirms the strong correlation between IMF slope and velocity dispersion, even when a complex distribution of ages and metallicities is allowed for. The middle panels reveal that only metallicities $[Z/H] \geqslant -0.1$ dex contribute to the analysis, in agreement with our previous results (see e.g. Fig. 10).

8 EXPECTED COLOURS AND M/L RATIOS

In addition to gravity-sensitive features from integrated light, the stellar IMF can affect indirectly other observable galaxy properties, like broad-band colours (see Goudfrooij & Kruijssen 2013) and mass-to-light ratios (hereafter M/L; see, e.g., Cappellari et al. 2012a; Ferré-Mateu et al. 2013). Hence, it is interesting to contrast the expectations from our best-fit stellar population models with those from broad-band photometry and (dynamical) M/L estimates.

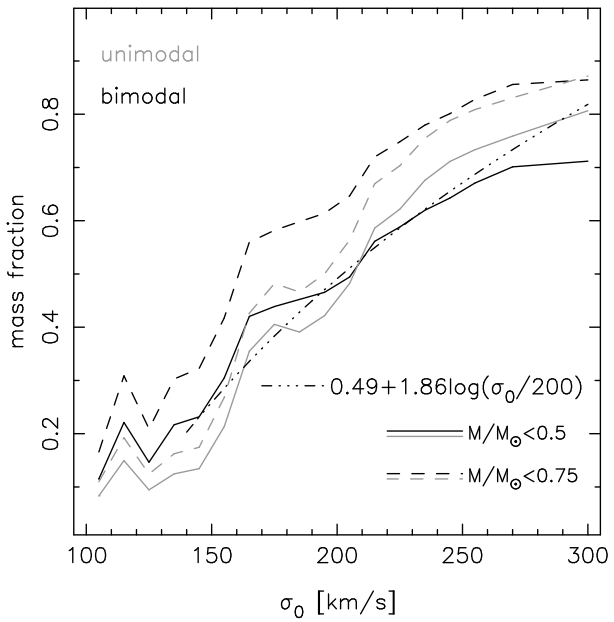

Figure 19. Stellar mass fractions expected from unimodal (grey) and bimodal (black) IMF models, as a function of velocity dispersion. Solid and dashed lines refer to the mass fractions of stars with mass smaller than 0.5 and 0.75 $M_\odot$, respectively. The dot–dashed curve shows the best-fit relation, $0.49 + 1.83\log(\sigma_0/200)$, to the mass fraction trends of both unimodal and bimodal models, for mass smaller than 0.5 $M_\odot$, in the range $\sigma_0 > 140$ km s^{-1}(see the text).

8.1 Variation of colours

Optical–NIR photometry provide additional constraints on the IMF, as a large fraction of M dwarfs can enhance the NIR light of a stellar population for an IMF heavier than Salpeter (see, e.g., Peletier et al. 1990), making optical–NIR colours significantly redder. In fact, an excess of reddening at optical–NIR wavelengths has been often invoked as an important argument against the steepening of the low mass end of the IMF with galaxy mass (see, e.g., Worthey, Ingermann & Serven 2011). In order to address this issue, we focus here on the bin at the highest velocity dispersion (i.e. $280 \leqslant \sigma_0 \leqslant 320$ km s^{-1}), for which the extended MILES (MIUSCAT)-based fits give the most bottom-heavy IMF, i.e. $\Gamma \sim 2$ and $\Gamma \sim 3$, for the unimodal and bimodal cases, respectively. Out of 160 ETGs in this bin (see Tab. 1), 21 galaxies have NIR (K-band) photometry available from the UKIDSS-LAS survey (see Paper I for details). The median $g - K$ for these galaxies [27] is reported in Tab. 7, and compared to the $g-K$ colour range of unimodal and bimodal extended MILES (MIUSCAT) models with bottom-heavy IMF. Model colours are estimated, for SSPs, using photometric stellar libraries, with the code of Vazdekis et al. (2010). To describe the high-mass systems,

[27] Notice that SDSS g-band photometry is in the AB system, while UKIDSS data are Vega-calibrated. As detailed in Paper I, colours are measured in an adaptive aperture of $3 \cdot r_{Kron,i}$, where $r_{Kron,i}$ is the i-band Kron radius. Median colours are corrected to the fibre aperture of radius 1.5″, using $g - K$ colour gradient estimates from La Barbera et al. (2010c) (Paper IV).

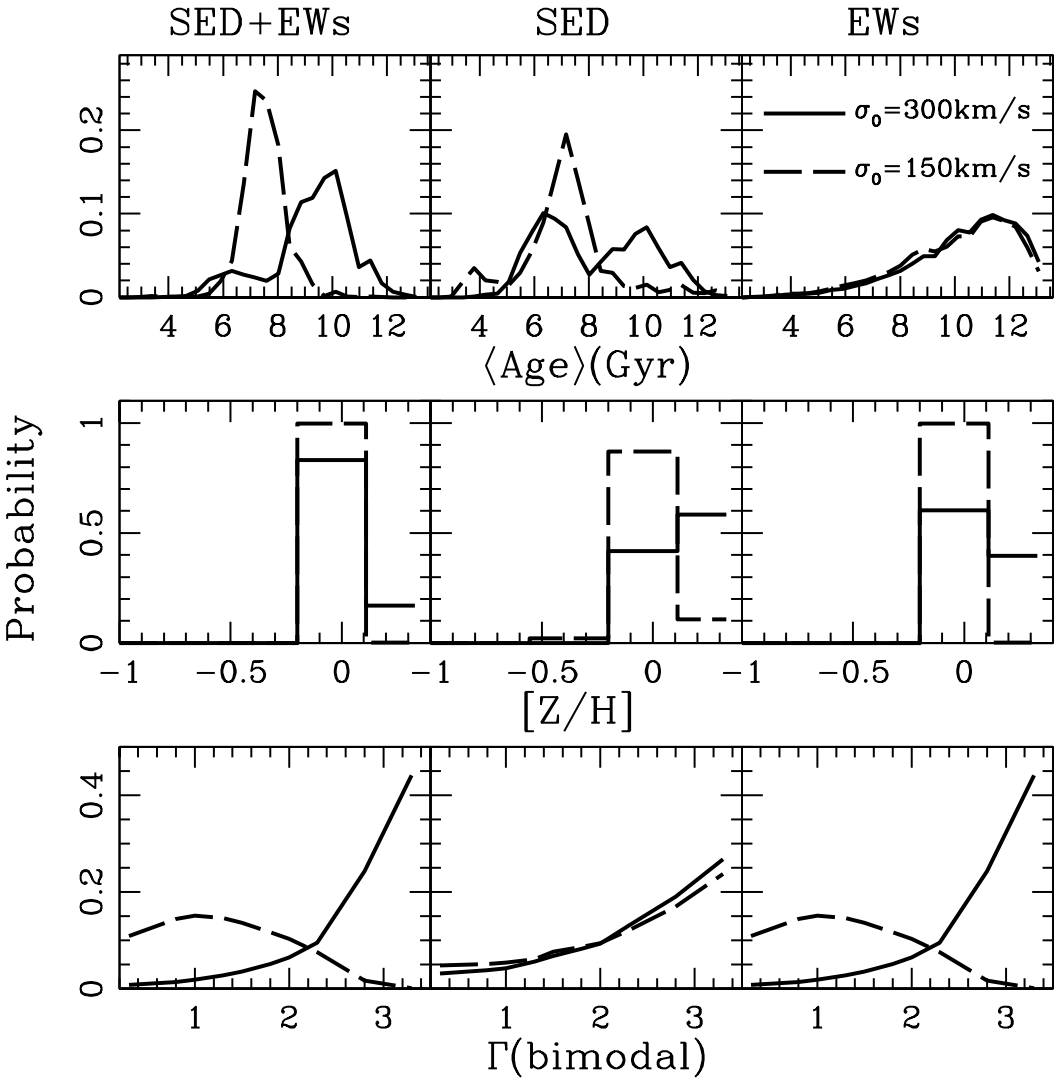

Figure 20. Probability distribution functions (PDFs) with respect to average age (top), metallicity (middle) and IMF slope (bottom) for two stacks, with velocity dispersion $\sigma_0 = 150$ km s^{-1} (dashed lines) and 300 km s^{-1} (solid lines). The hybrid method is considered (see §7.5) for a grid of τ models (see text for details). In each case, the joint PDF is shown on the leftmost panels (SED+EWs), with the individual PDFs split between spectral fitting (SED, middle) and line strengths (EWs, right).

Table 7. Optical-NIR colours for extended MILES (MIUSCAT) models with a bottom-heavy IMF, and our highest σ_0 stack.

$g-K$	Description
3.75–4.00	SSP, unimodal IMF, $\Gamma = 2$, $0 \leqslant [Z/H] \leqslant 0.22$, Age > 12 Gyr
3.65–3.97	SSP, bimodal IMF, $\Gamma = 3.3$, $0 \leqslant [Z/H] \leqslant 0.22$, Age > 12 Gyr
3.90 ± 0.02	observed, $N_{\rm ETGs} = 21$, $280 \leqslant \sigma_0 \leqslant 320$ km s^{-1}

we consider only colours for metallicities equal or above solar, and old ages (> 12 Gyr). The range of model colours in the Table is fully consistent with the observed $g-K$, even for the reddest unimodal models. We remark here that a detailed comparison of constraints from spectral indices and broad-band colours is beyond the scope of the present paper and will be addressed in a forthcoming contribution. Notice also that although a varying IMF can affect significantly some optical colours (e.g. $r-i$), proper modelling of different optical colours for quiescent galaxies still represents a challenge for current stellar population models, and the effect of α-enhancement on optical (as well as NIR) colours remains to be fully understood (see MIUSCAT-II). However, for the purpose of the present work, we emphasize

that optical–NIR colours do not pose any problem for the hypothesis of a bottom-heavy IMF in massive ETGs.

8.2 Variation of M/L

Fig. 21 plots the median dynamical M/L as a function of σ_0. The M/L is estimated as $5 \times R_e\sigma_e^2/(G \cdot L)$ (see, e.g., Cappellari et al. 2012b), where R_e is the effective radius, σ_e is the central velocity dispersion corrected to an aperture of $1\,R_e$, G is the gravitational constant, and L is the total galaxy luminosity. Both R_e and L are measured for each galaxy by fitting seeing-convolved Sérsic models to the SDSS r-band galaxy images (see SPIDER-I for details). The aperture correction to σ_0 is performed by using eq. 1 of Cappellari et al. (2006). The above approximation for M/L provides an estimate of the M/L within $1\,R_e$ with an accuracy of ~ 0.03 dex. This uncertainty is added in quadrature, for each σ_0 bin, to the error on the median M/L. We refer the reader to, e.g., Tortora et al. (2012); Cappellari et al. (2012b); Tortora et al. (2013) for a discussion on the impact of different model assumptions on the estimate of M/L. For the purpose of the present work, we do not aim to discuss the details beyond the computation of M/L, but instead, we focus on the comparison between the predictions of the stellar M/L (hereafter $M_\star/L$) from our best-fit population models with the estimates of the dynamical M/L. The key aspect is the constraint that stellar mass-to-light ratios cannot exceed dynamical estimates, i.e. $M_\star/L \leqslant M/L$. The expected $M_\star/L$'s are overplotted in Fig. 21, for $1SSP$, $2SSP$, and $2SSP + X/Fe$ models, respectively, and for bimodal (upper-) and unimodal (lower-) models [28]. The $1\,\sigma$ confidence contours on $M_\star/L$ are plotted only for $2SSP$ models, for clarity. The Figure shows that a unimodal IMF gives too high, and thus unphysical, $M_\star/L$, with respect to the dynamical M/L. Hence, although the unimodal models do fit spectral indices as well as the bimodal ones, they seem to be rejected based on the $M_\star/L$ predictions. On the contrary, bimodal models give an $M_\star/L$ broadly consistent with M/L, even for strongly bottom-heavy models, as at highest σ_0. Considering error bars, our bimodal best-fits are also compatible with stellar mass-to-light ratios being smaller than the dynamical ones, leaving room for additional, non-stellar, matter (i.e. dark-matter). A similar conclusion has been recently drawn by Conroy & van Dokkum (2012b), for a subsample of 35 ETGs from the SAURON survey. We remark that the above conclusions are based on the assumption that the expression for the dynamical M/L from Cappellari et al. (2012b) applies to the whole population of ETGs, represented by our stacked spectra. Detailed dynamical and lensing studies for large samples of ETGs will help to address this point in the future.

9 SUMMARY

This paper explores in detail the recent claims of a systematic variation of the low-mass end of the IMF in massive early-type galaxies (ETGs). In order to set robust constraints, we need a large, representative dataset of galaxy spectra at very high signal-to-noise ratio. For this purpose, we stack a large, high-quality sample of SDSS spectra, comprising 24,781 low redshift ($z \sim 0.07$) ETGs from the SPIDER survey (La Barbera et al. 2010a). The stacking is performed in bins, corresponding to their central velocity dispersion, and, at fixed velocity dispersion, we also assemble a subsample split with respect to α-enhancement, by using a solar-scale proxy ($[Z_{Mg}/Z_{Fe}]$, see Fig. 6). We select a variety of IMF-sensitive spectral features (Mg4780, TiO1, $\mathrm{TiO2_{SDSS}}$, $\mathrm{Na8190_{SDSS}}$, CaT, see Fig. 4), along with additional indices strongly sensitive to the abundance of individual elements that could affect their interpretation. The analysis includes standard age and metallicity indicators ($[\mathrm{MgFe}]'$, $\mathrm{H}\beta_o$, $\mathrm{H}\gamma_F$). After being corrected to solar-scale by means of semi-empirical correlations among line strengths and $[Z_{Mg}/Z_{Fe}]$ at fixed σ_0, the indices are fitted with state-of-the-art population synthesis models. We use the extended MILES (MIUSCAT) library (Vazdekis et al. 2012), covering a wide range of age, metallicity, star-formation histories, and IMF. The analysis is complemented with an independent hybrid approach, where direct spectral fitting in the optical is combined with constraints from IMF-sensitive features (following our previous work, Ferreras et al. 2013). Two types of IMF are considered, a single power-law distribution, generalizing the Salpeter law, and a bimodal IMF, with a gradual turn-off at low mass, that generalizes the Kroupa case. The main results can be summarized as follows:

i. All selected spectral features consistently suggest a vari-

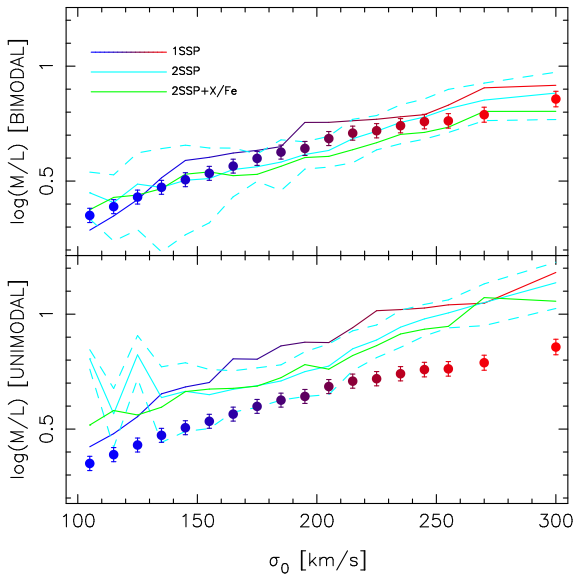

Figure 21. Mass-to-light ratios as a function of central velocity dispersion, for bimodal (top) and unimodal (bottom) best-fitting models of spectral indices. Dots and error bars are median dynamical mass-to-light ratios, with $1\,\sigma$ error bars on median values, while solid curves give stellar mass-to-light ratios predicted for different stellar population models of spectral indices, including the effect of a bottom-heavier IMF at high (relative to low) σ_0. Dashed curves mark $2\,\sigma$ confidence intervals on $2SSP$ model predictions. Notice the good matching of bimodal models to the dynamical estimates.

[28] The $M_\star/L$ estimates, as plotted in Fig. 21, are made available on request to the authors in tabular format, along with the same estimates obtained for a Kroupa Universal IMF.

ation of IMF slope (Γ) in ETGs, with a trend from a Kroupa/Chabrier case at low central velocity dispersion, towards a more bottom-heavy IMF with increasing σ_0. For a bimodal IMF, the best-fit Γ increases from about 1.3 at $\sigma_0 \lesssim 150$ km s^{-1} to almost 3 at $\sigma_0 \sim 300$ km s^{-1}. For unimodal models, the slope varies from $\Gamma \sim 1$ to 2 over the same σ_0 range (Fig. 12). The fits to the Γ–σ_0 correlation (eq. 3) give consistent values between different methods (Tab. 4), although we note that the physical quantity being constrained is the mass fraction in low-mass stars (see iii. below)

ii. Both unimodal and bimodal cases fit equally well all selected spectral indices, implying that we cannot distinguish between these two kinds of models based on the indices alone (see, e.g., Fig. 11 and 18). However, unimodal models seem to be clearly rejected by their overly high values of the stellar (relative to dynamical) mass-to-light ($M_\star/L$) ratios (Fig. 21). On the other hand, the varying-IMF bimodal best-fits are in good agreement with independent constraints, i.e. dynamical M/L estimates, and the optical-NIR broad-band colours of ETGs in our sample.

iii. Although unimodal and bimodal models cannot be distinguished with the present analysis, they predict very consistent stellar mass fractions at birth in low-mass stars ($< 0.5\,M_\odot$), varying from $\sim 20\,\%$ at $\sigma_0 \sim 100$ km s^{-1} to $\sim 70\%$ at $\sigma_0 \sim 300$ km s^{-1}(Fig. 19). Such stellar low-mass fractions (Eq. 4) represent the most robust constraint from the present analysis, and should be matched by theories aimed to explain the stellar IMF.

iv. The fact that both solar-scale corrected IMF- and abundance-sensitive line strengths from different species, i.e. Na, Ca, TiO, and Mg, can be all consistently explained by models with a varying IMF gives strong support to the claim that the IMF truly changes at the low-mass end in ETGs with high velocity dispersion, in constrast to a picture whereby single element adundances conspire to change simultaneously with σ_0. Indeed, including a varying abundance of Na, Ca, and Ti in our fits (based on Conroy & van Dokkum 2012a stellar population models), we find no evidence for a significant variation of these abundances with σ_0 besides the general [α/Fe] trend (Fig. 14).

v. The range of variation of IMF-sensitive line strengths with σ_0 is essentially similar for both low- and high-[α/Fe] stacks, implying that velocity dispersion (i.e. possibly galaxy mass) is the main driver of IMF variation, regardless of changes in α-enhancement.

vi. Regarding the [α/Fe], we find a remarkably tight correlation between the (nearly) solar-scale proxy, $[Z_{Mg}/Z_{Fe}]$, i.e. the difference between the two metallicities estimated from Mg and Fe lines with solar-scaled models, and the "true" [α/Fe], i.e. the one obtained by using α-enhanced stellar population models (Fig 6). This proves that one can study abundance ratio effects by relying entirely on solar-scaled models.

vii. Besides CaT and CaHK, we have also tried to fit the well-known Lick-based Ca4227 feature. This index remains a puzzle for current stellar population models, as no fitting scheme is able to match its line strengths, especially at high-σ_0, where model indices are far too high with respect to the observations (Fig. 16). The [Ca/Fe] under-abundance explanation for this discrepancy seems to be excluded because the extended MILES (MIUSCAT) base models match well both the CaHK and CaT features (see, e.g., Fig.11).

From the modelling point of view, the suggested change in the IMF of ETGs with velocity dispersion could be expected from the different physical properties of the star forming clouds during the formation of a massive galaxy (Larson 2005) – such as a turbulent ISM with a very high Mach number (Hopkins 2012). Alternatively, variations in the IMF properties convolved with the star formation history can leave its imprint on the so-called integrated galactic IMF (IGIMF, see, e.g., Kroupa & Weidner 2003), which corresponds to the superposition of all populations ever formed, and constitutes the observable we really map with unresolved spectroscopic data. Regardless of whether the cause lies in the microphysics of star formation, or the global formation history, the robust constraints we impose here on the initial mass fraction in low-mass stars should be met by any theory of star formation.

ACKNOWLEDGMENTS

We would like to thank the anonymous referee for his/her helpful report, which definitely helped improving parts of this manuscript. We also thank R. Smith for helpful comments on this manuscript. This paper is based on data retrieved from the Sloan Digital Sky Survey archives (`http://www.sdss.org/collaboration/credits.html`).
We have also made use of the 4th data release of the UKIDSS survey (Lawrence et al. 2007), which is described in detail in Warren et al. (2007). Funding for the SDSS and SDSS-II has been provided by the Alfred P. Sloan Foundation, the Participating Institutions, the National Science Foundation, the U.S. Department of Energy, the National Aeronautics and Space Administration, the Japanese Monbukagakusho, the Max Planck Society, and the Higher Education Funding Council for England. JFB acknowledges support from the Ramón y Cajal programme by the Spanish Ministry of Economy and Competitiveness (MINECO). This work has been supported by the Programa Nacional de Astronomía y Astrofísica of MINECO, under grants AYA2010-21322-C03-01 and AYA2010-21322-C03-02 and by the Generalitat Valenciana under grant PROMETEO-2009-103.. MT acknowledges the support of FAPESP, process no. 2012/05142-5.

APPENDIX A: DEFINITION OF Na8190$_{\rm SDSS}$ AND TiO2$_{\rm SDSS}$ SPECTRAL INDICES

In the present work, we adopt a modified version of TiO2 and NaI8200A spectral indices, previously defined by Trager et al. (1998) and Vazdekis et al. (2012), respectively. The NaI8200A index is, in turn, a modified version of the NaI doublet index proposed by Schiavon et al. (1997a). The reason for adopting a modified version of these indices is illustrated in Fig. A1, where we plot the stacked spectrum with $200 \leqslant \sigma_0 \leqslant 210$ km s^{-1} in the spectral range of TiO2 ($6050 \leqslant \lambda \leqslant 6470$ Å; left) and NaI ($8110 \leqslant \lambda \leqslant 8290$ Å; right). Two extended MILES (MIUSCAT) SSP models, with age 9 Gyr, solar metallicity ($[Z/H] = 0$), and two different IMFs, i.e. $\Gamma = 1.3$ (Kroupa-like) and $\Gamma = 2.8$, are overplotted. The SSPs have been smoothed to match the spectral resolution and velocity dispersion of the stack. The

red hatched regions mark the central bandpasses of the indices, for which we keep the original definition of TiO2 and NaI8200A. The grey hatched regions are the original sidebands of TiO2 and NaI8200A. While there is good agreement between models and data in the blue (red) pseudo-continuum of TiO2 (NaI8200A), for both IMFs, the models show a $\sim 1\%$ deviation from the observed spectrum in the red (blue) sidebands of TiO2(NaI8200A). The largest deviations are seen at $\lambda \sim 6380\,$Å and $\lambda \sim 8170\,$Å, and are also present in the other stacked spectra. The discrepancies are not removed by changing the age and metallicity (as well as IMF) of the SSP models, for $Age \geqslant 3\,$Gyr and $[Z/H] \geqslant -0.4$. Hence, we have re-defined the red (blue) sideband of TiO2 (NaI8190A) in order to minimize any deviation between models and data. This is done as follows.

1. We adopt the original definition of TiO2 and NaI8190A, and compute the $2SSP$ best-fit model to spectral indices (see Sec. 6). We assume here a Kroupa IMF in order to avoid any bias towards a σ_0-varying IMF (which is the hypothesis we want to test);
2. For TiO2, we vary the position (i.e. the lowest wavelength endpoint, λ_1) and width, $\delta\lambda$, of the red sideband, minimizing the absolute deviation of the index equivalent width between models and data. To this effect, we keep the central band and blue sideband definitions fixed to those of TiO2. The absolute deviation is computed by summing up the EW absolute deviations for five stacks ($\sigma_0 = 100$, 150, 200, 250, and 300 $\mathrm{km\,s^{-1}}$), spanning the whole velocity dispersion range. The deviation is minimized for $\lambda_1 = 6422\,$Å and $\delta\lambda = 33\,$Å (see the green hatched region in the left panel of Fig. A1). We adopt this definition throughout the present work, referring to the corresponding spectral index as $\mathrm{TiO2_{SDSS}}$, to point out that the definition has been optimized for the SDSS spectra.
3. For NaI8190A, we adopt a similar procedure to that at point 2 for TiO2, but varying the position of the blue sideband of the index. We impose the constraint $\delta\lambda \geqslant 10\,$Å, i.e. the value adopted in Vazdekis et al. (2012), in order to avoid overly reducing the region where the blue pseudo-continuum is measured. The minimum absolute deviation is obtained for $\lambda = 8143\,$Å, and $\delta\lambda = 10\,$Å (see the green hatched region in the right panel of the Figure). We refer to the corresponding spectral index as $\mathrm{Na8190_{SDSS}}$.

Repeating the entire procedure, but replacing TiO2 and NaI8190A at step 1 with $\mathrm{TiO2_{SDSS}}$ and $\mathrm{Na8190_{SDSS}}$ gives very similar sideband definitions as those adopted here, proving that the procedure is self-consistent. We also experimented with changing the Kroupa IMF assumption in step 1 with a σ_0-varying bimodal IMF (blue-through-red curve in top panel of Fig. 12), finding the optimum definitions of λ_1 and $\delta\lambda$ to change by only a few Angström.

In Fig. A2, we show the dependence of $\mathrm{TiO2_{SDSS}}$ and $\mathrm{Na8190_{SDSS}}$ EWs on velocity dispersion. These indices have the further advantage to be less sensitive to resolution than the previously defined TiO2 and NaI8200A. For $\mathrm{Na8190_{SDSS}}$, the decreased sensitivity is due to the fact that the blue sideband is measured in a more distant region from the feature. We also note that, as shown in Sec. 4, the new $\mathrm{TiO2_{SDSS}}$ and $\mathrm{Na8190_{SDSS}}$ indices have similar sensitivity to age, metallicity, and IMF as TiO2 and NaI8200A.

APPENDIX B: EMISSION CORRECTION TO Hβ

In order to fit the spectral indices with stellar population models, we correct the Hβ_o spectral index for contamination from nebular emission. The presence of such contamination in our stacked spectra of ETGs is shown in Fig. B1, where we plot the spectral region around the [OII] feature at $\lambda = 3727\,$Å for the stacks at the endpoints of the velocity dispersion range, i.e. $100 \leqslant \sigma_0 \leqslant 110$ $\mathrm{km\,s^{-1}}$ (top) and $280 \leqslant \sigma_0 \leqslant 320$ $\mathrm{km\,s^{-1}}$ (bottom), respectively. Best-fitting extended MILES (MIUSCAT) models, obtained by direct fitting of the spectral region of interest are overplotted in grey (assuming a Kroupa IMF). Notice the flux excess at $\lambda \sim 3727\,$Å, in particular at the lowest σ_0, revealing the presence of nebular emission in the spectra.

The correction procedure to Hβ_o is illustrated in Fig. B2. For a given IMF (either bimodal or unimodal), we fit the Hβ spectral region (from 4810 to 4910 Å) with a linear combination of two MIUSCAT SSPs, excluding the trough of the line (i.e. from 4856 to 4866 Å). To improve the matching of the continuum, a multiplicative fourth degree polynomial is also used in the fitting. The residuals (bottom panel of the Figure) are fitted with a Gaussian function. The emission correction is given by the difference between the Hβ_o index of the stack and the one re-measured on the same stack after adding the Gaussian fit. By definition, this procedure will depend on the assumed IMF. For instance, for the $100 \leqslant \sigma_0 \leqslant 110$ $\mathrm{km\,s^{-1}}$ ($280 \leqslant \sigma_0 \leqslant 320$ $\mathrm{km\,s^{-1}}$) stack, the emission correction varies from $\sim 0.13\,$Å (0.09 Å) for $\Gamma = 0.3$, to $\sim 0.08\,$Å (0.05 Å) for $\Gamma = 3.3$ (bimodal IMFs). Although the Γ dependence is small, following our previous work (FLD13), we have implemented an iterative procedure for the $1SSP$ and $2SSP$ models (see Sec. 6). First, we correct Hβ_o with the median correction (among all IMFs), and then we fit the spectral indices. Once the best-fit Γ is derived, the emission correction is updated accordingly, and the fitting is repeated again. In practice, we found that further iterations are not required, as the fits do not change appreciably when performing a second iteration. Notice that in FLD13 we applied a similar procedure to that described here. However, rather than fitting the stacks with two MIUSCAT SSPs in the Hβ spectral region, we ran the `STARLIGHT` spectral fitting code over a larger spectral range. We found that the two SSP fits provide more robust results than our previous approach, being less sensitive to the adopted IMF. We note that either varying the degree of the multiplicative polynomial between two and six, or changing the size of the line trough, excluded from the fitting, between 5 and 15 Å, does not produce any significant change to our results. The Hβ_o correction turns out to vary smoothly with σ_0, from $\sim 0.12\,\mathring{A}$ at lowest σ_0 to $\sim 0.04\,\mathring{A}$ for $\sigma_0 > 250$ $\mathrm{km\,s^{-1}}$, further confirming the robustness of our approach.

APPENDIX C: APERTURE EFFECTS

Given that the spectra used in this paper correspond to the central 3 arcsec region of each galaxy, a significant radial gradient of the properties of the stellar populations could affect the results. In Fig. C1 we explore this issue by showing, in the rightmost panels the variation of three of the

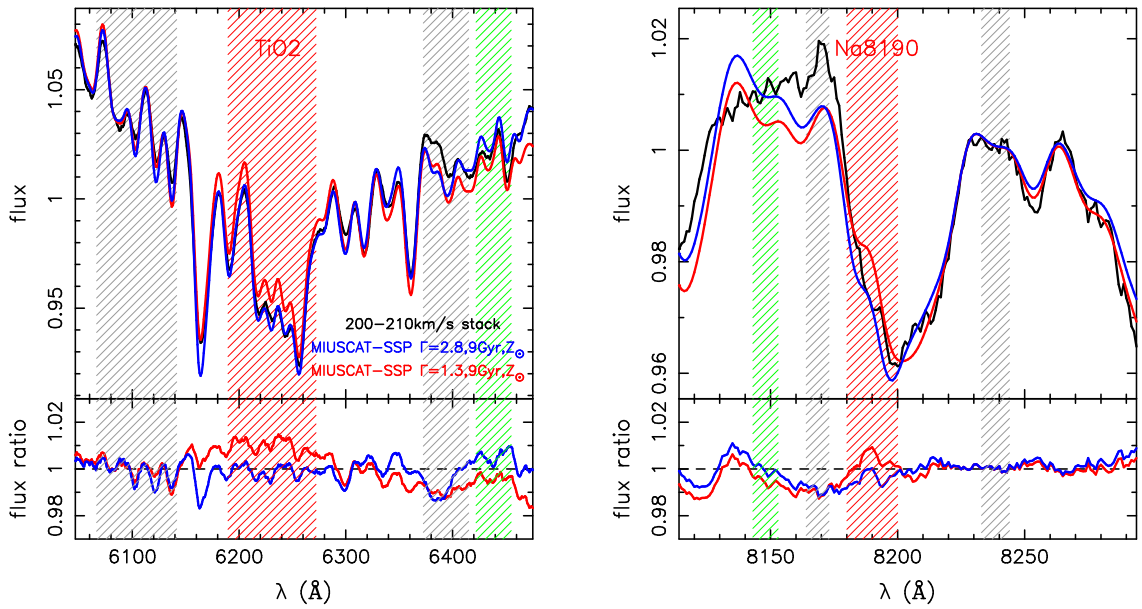

Figure A1. Re-definition of TiO2 (left) and Na8190 (right) spectral indices. The top panels show the SDSS stacked spectrum for $200 \leqslant \sigma_0 \leqslant 210$ km s^{-1} (black), and two extended MILES (MIUSCAT) SSPs, with solar metallicity, age of 9 Gyr, and two bimodal IMFs, namely a Kroupa-like IMF ($\Gamma = 1.3$; red) and a bottom-heavy model ($\Gamma = 2.8$, blue). The SSPs were smoothed to match the spectral resolution plus σ_0 of the stack. Both data and models have been scaled by the median flux computed over the spectral regions encompassed by the TiO2 and NaI8200A definitions. The red hatched regions map the index central passbands, while grey hatched regions mark the index sidebands. The bottom panels plot residuals between the two IMF models and data. Notice the deviation of both Kroupa-like and bottom-heavy models with respect to the data in the red and blue sidebands of TiO2 and NaI8200A, respectively. To minimize this discrepancy, we have optimized the definition of red and blue sidebands of TiO2 and NaI8200A (see text for details). The modified sidebands (green regions) define the spectral indices $\mathrm{TiO2_{SDSS}}$ and $\mathrm{Na8190_{SDSS}}$, used in the present work.

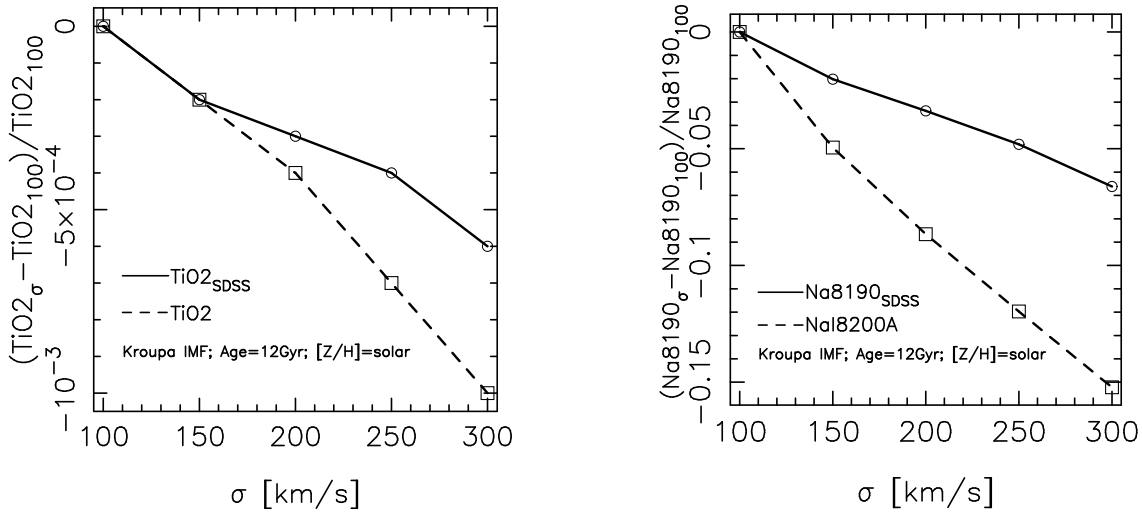

Figure A2. Sensitivity of the $\mathrm{TiO2_{SDSS}}$ (left) and $\mathrm{Na8190_{SDSS}}$ (right) spectral indices to resolution. The plot shows the relative variation of line strengths as a function of velocity dispersion, in the same range as our stacked spectra (namely, from $\sigma = 100$ to 300 km s^{-1}). Solid lines refer to indices defined in previous works, i.e. TiO2 (Trager et al. 1998) and NaI8200A (MIUSCAT-I). The dashed lines correspond to the indices adopted in the present study, optimized to better match the SDSS data with extended MILES (MIUSCAT) 2SSP models (independent of the IMF). The curves refer to an extended MILES (MIUSCAT) SSP model with Kroupa IMF, solar metallicity, and age of 12 Gyr, as labelled. Notice that the optimized indices are less sensitive to velocity dispersion than those defined in previous works.

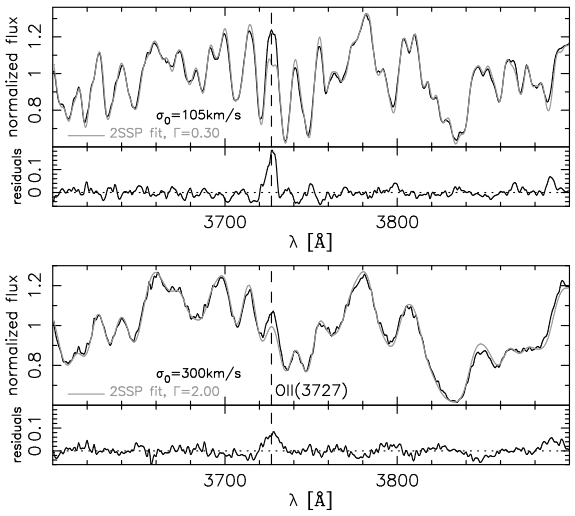

Figure B1. Evidence for nebular emission in stacked spectra of ETGs at the extremes of velocity dispersion in our sample, namely $100 \leqslant \sigma_0 \leqslant 110\,\mathrm{km\,s^{-1}}$ (*top plot*) and $280 \leqslant \sigma_0 \leqslant 320\,\mathrm{km\,s^{-1}}$ (*bottom plot*). For each plot, the upper panel shows the observed spectrum (black) at its nominal resolution, and the MIUSCAT best-fitting model (grey), obtained by assuming a Kroupa IMF (see text for details). The lower panel shows residuals, obtained by subtracting the model to the observed spectrum. Vertical dashed lines mark the [OII] feature at $\lambda = 3727\,\text{Å}$, while horizontal dotted lines mark a residual value of zero.

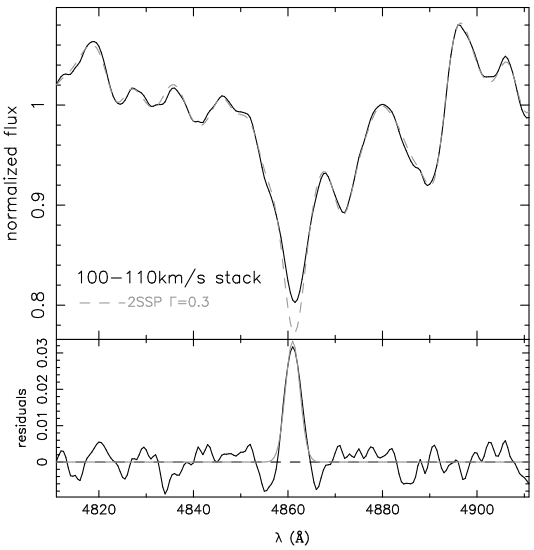

Figure B2. Correction method for the Hβ_o equivalent width of stacked spectra from nebular emission. (*Top*) The lowest σ_0 stack (black) is shown along with the best-fit MIUSCAT model for a bimodal IMF with $\Gamma = 0.3$ (grey). (*Bottom*) The residuals of the fit (black) are fitted with a Gaussian function (grey), that determines the Hβ_o correction for nebular emission (see text for details).

most IMF-sensitive line strengths, with respect to effective radius, in comparison to the SDSS 3 arcsec diameter fibre. The shaded regions encompass the $1\,\sigma$ confidence level of the $100\,\mathrm{km\,s^{-1}}$ (black) and $200\,\mathrm{km\,s^{-1}}$ (grey) stacks. For reference, the panels on the left show the variation of the line strengths over the whole range in velocity dispersion. The figure confirms that our results are not affected by variations in radial gradients of the stellar populations.

APPENDIX D: SYNTHETIC SSPS WITH VARYING ABUNDANCE RATIOS

In addition to the CvD12 stellar population models, we have also tested the effect of individual variations of Ca, Na, and Ti abundances on the targeted spectral indices by creating a set of simplified SSP models. Empirical stellar libraries are not well suited for this purpose, since they are restricted to abundance patterns of stars in the solar neighbourhood. For this reason, we rely completely on synthetic stellar libraries. To generate stellar spectra, we use the Padova evolutionary tracks (Bertelli et al. 2008), identifying 16 $\log g$–$T_{\rm eff}$ pairs along the 12 Gyr isochrone, from the tip of the RGB ($T_{\rm eff} = 3000\,\mathrm{K}$ and $\log g = -0.1$) down to the main sequence locus corresponding to a stellar mass of $0.15\,\mathrm{M_\odot}$ ($T_{\rm eff} = 3400\,\mathrm{K}$ and $\log g = 5.2$). For each $\log g$–$T_{\rm eff}$ pair. we generate synthetic stellar spectra with the `PFANT` code described in Cayrel et al. (1991), Barbuy et al. (2003) and Coelho et al. (2005). Given a stellar model atmosphere and lists of atomic and molecular lines, the code computes a synthetic spectrum assuming local thermodynamic equilibrium (LTE). We have used a refined atomic and molecular line list, calibrated through several stellar spectroscopic

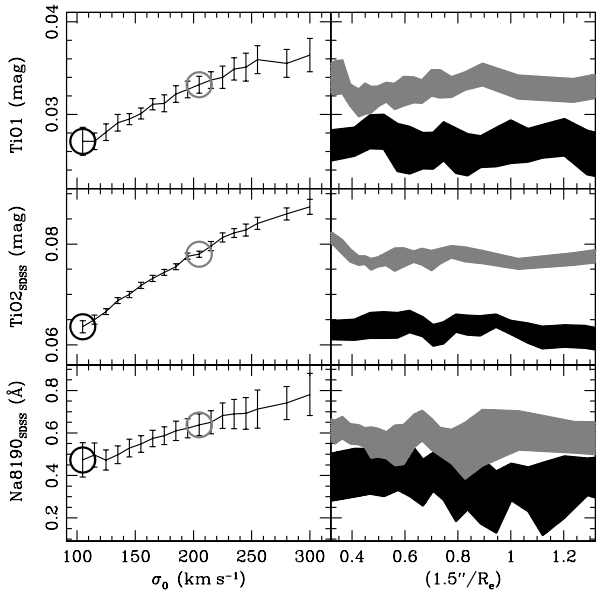

Figure C1. (*Left*) Variation of three IMF-sensitive line strengths with respect to velocity dispersion. (*Right*) Two stacks are considered (circled in the panels on the left), with velocity dispersion of $\sigma_0 = 100$ (black) and 200 (grey) $\mathrm{km\,s^{-1}}$. The shaded regions represent the variation in the corresponding line strengths with respect to effective radius, compared with the fixed 3 arcsec diameter fibre of the SDSS spectrograph. Error bars are shown at the $1\,\sigma$ confidence level.

studies (see, e.g., Barbuy et al. 2003). For stellar atmosphere models, we used the `MARCS 1D` hydrostatic LTE models (Gustafsson et al. 2008). For $\log g > 3$, the atmospheric model geometry is plane-parallel and mass independent; for $\log g < 3$ (giants with non-negligible photospheric depths), the models are calculated for a spherical geometry. In the latter case, models for $1\,M_{\odot}$ are adopted. A microturbulent velocity of $2\,km\,s^{-1}$ is adopted for all spectra. Notice that the flux predictions of `PFANT` are less accurate in the blue part of the spectrum, in particular at $\lambda < 5000\,\AA$, because of the so-called "predicted lines" problem (Kurucz 1992). For this reason, the use of our synthetic SSPs to model features at wavelengths bluer than 5000 $\AA$ (e.g., the CaHK, see Sec. 7.3) should be taken with some caution.

The SSP spectra, corresponding to an age of 12 Gyr, are created using the integral

$$f(\lambda) = \int_{m_1}^{m_2} s(\lambda, m)\phi(m)dm$$

where $s(\lambda, m)$ is the spectrum of an individual star with mass m at a given λ, and $\phi(m)$ is the (assumed) IMF. We adopt a mass interval from $m_1 = 0.15\,M_{\odot}$ to $m_2 = 1.01\,M_{\odot}$. We consider Kroupa as well as unimodal IMFs, the latter with $\Gamma = 0.3$, 1.35 (i.e. Salpeter) and 2.3, respectively. Notice that stars with $M < 0.15\,M_{\odot}$ are not included in the synthesis, as there are no Padova evolutionary tracks available below this mass limit. As discussed by CvD12, even in the case of a strongly bottom-heavy population (e.g. $\Gamma = 3.3$), this approximation should have little impact on the results, because of the negligible contribution of stars with $0.08 < M < 0.15\,M_{\odot}$ to the SSP integrated light. Fig. D1 compares one of our simple SSPs, with solar composition, to a MILES extended (MIUSCAT) SSP, with similar age, metallicity, and the same (Kroupa) IMF. Despite of the simple approach to create the synthetic models, the agreement with the MILES extended models is fairly good, with an rms of $\sim 2\%$ at $\lambda > 4500\,\AA$, and $\sim 10\%$ in the bluer part of the spectrum ($\lambda < 4500\,\AA$). We remind the reader that the simplified SSPs presented here are used only in a relative sense, i.e. to compute differences in the spectral indices when varying individual element abundances. We also notice that our synthetic SSPs are based on rather different ingredients than the CvD12 ones. In particular, we use the `MARCS` and `PFANT` codes for the atmospheric models and stellar spectra, while CvD12 adopt the `ATLAS12` (Kurucz 1970) and `SYNTHE` (Kurucz & Avrett 1981) codes, respectively. CvD12 adopt atomic and molecular line lists with oscillator strengths computed either theoretically or from lab measurements, while our oscillator strengths have been calibrated through several stellar spectroscopic studies. The synthetic stellar spectra in both models are created down to a stellar mass of $0.15\,M_{\odot}$. However, CvD12 extrapolate the library down to $0.08\,M_{\odot}$, while we completely disregard these low-mass stars. Finally, we use Padova evolutionary tracks, while CvD12 use Dartmouth isochrones (Dotter et al. 2008).

REFERENCES

Abazajian, K. N., et al., 2009, ApJS, 182, 543

Adelman-McCarthy, J.K., Agüeros, M.A., Allam, S.S., et al., 2008, ApJS, 175, 297

Auger, M.W., Treu, T., Bolton, A.S., Gavazzi, R., Koopmans, L.V.E., Marshall, P.J., Moustakas, L.A., Burles, S., 2010, ApJ, 724, 511

Barbuy B., Perrin M.-N., Katz D., Coelho P., Cayrel R., Spite M., Van't Veer-Menneret C., 2003, A&A, 404, 661

Barnabé, M., Czoske, O., Koopmans, L.V.E., Treu, T., Bolton, A.S., 2011, MNRAS, 415, 2215

Bastian, N., Saglia, R.P., Goudfrooij, P., Kissler-Patig, M., Maraston, C., Schweizer, F., Zoccali, M., 2006, A&A, 448, 881

Bastian, N., Covey, K. R. & Meyer, M. R. 2010, ARA&A, 48, 339

Bernardi, M., et al., 2003a, AJ, 125, 1817

Bernardi, M., Sheth, R.K., Annis, J. 2003b, AJ, 125, 1849

Bernardi, M., Sheth, R. K., Nichol, R. C., Schneider, D. P. & Brinkmann, J. 2005, AJ, 129, 61

Bertelli, G. et al. 2008, A&A, 484, 815

Bruzual, G., & Charlot, S. 2003, MNRAS, 344, 1000 (BC03)

Cappellari, M., et al., 2006, MNRAS, 366, 1126

Cappellari, M., et al., 2012, Nature, 484, 485

Cappellari, M., et al., 2012, MNRAS, submitted (arXiv:1208.3522)

Cappellari, M., et al., 2012c, MNRAS, submitted (arXiv:1208.3523)

Cardelli, J. A., Clayton, G. C., Mathis, J. S., 1989, ApJ, 345, 245

Carter, D., Visvanathan, N., Pickles, A.J., 1986, ApJ, 311, 637

Cayrel, R., Perrin, M.-N., Barbuy, B., Buser, R., 1991, A&A, 247, 108

Chabrier, G., PASP, 115, 763

Cid Fernandes, R., Mateus, A., Sodré, L., Stasinska, G., Gomes, J. M., 2005, MNRAS, 358, 363

Capaccioli, M., Caon, N., & D'Onofrio, M. 1992, MNRAS, 259, 323

Cenarro, A. J., Cardiel, N., Gorgas, J., Peletier, R. F., Vazdekis, A., Prada, F., 2001, MNRAS, 326, 959

Cenarro, A. J., Gorgas, J., Vazdekis, A., Cardiel, N., Peletier, R. F., 2003, MNRAS, 339, L12

Cervantes, J. L., Coelho, P., Barbuy, B., and Vazdekis, A., 2007, Proceedings IAU Symposium No. 241 'Stellar Populations as Building Blocks of Galaxies', A. Vazdekis and R.F. Peletier, eds, 167

Cervantes, J. L., Vazdekis, A., 2009, MNRAS, 392, 691

Coelho, P., Barbuy, B., Meléndez, J., Schiavon, R. P., Castilho, B. V., 2005, A&A, 443, 735

Coelho, P., Bruzual, G., Charlot, S., Weiss, A., Barbuy, B., Ferguson, J.W., 2007, MNRAS, 382, 498

Cohen, J. G., 1978, ApJ, 221, 788

Conroy, C., van Dokkum, P., 2012a, ApJ, 747, 69

Conroy, C., van Dokkum, P., 2012b, ApJ, 760, 71

de la Rosa, I. G., la Barbera, F., Ferreras, I., de Carvalho, R. R. 2012, MNRAS, 418, L74

Delisle, S., Hardy, E., 1992, AJ, 103, 711

Diaz, A.I., Terlevich, E., Terlevich, R., 1989, MNRAS, 239, 325

Dotter, A., Chaboyer, B., Jevremović, D., Kostov, V., Baron, E., Ferguson, J. W., 2008, ApJ, 178, 89

Dutton, A. A., Mendel, J. T., Simard, L., 2012, MNRAS,

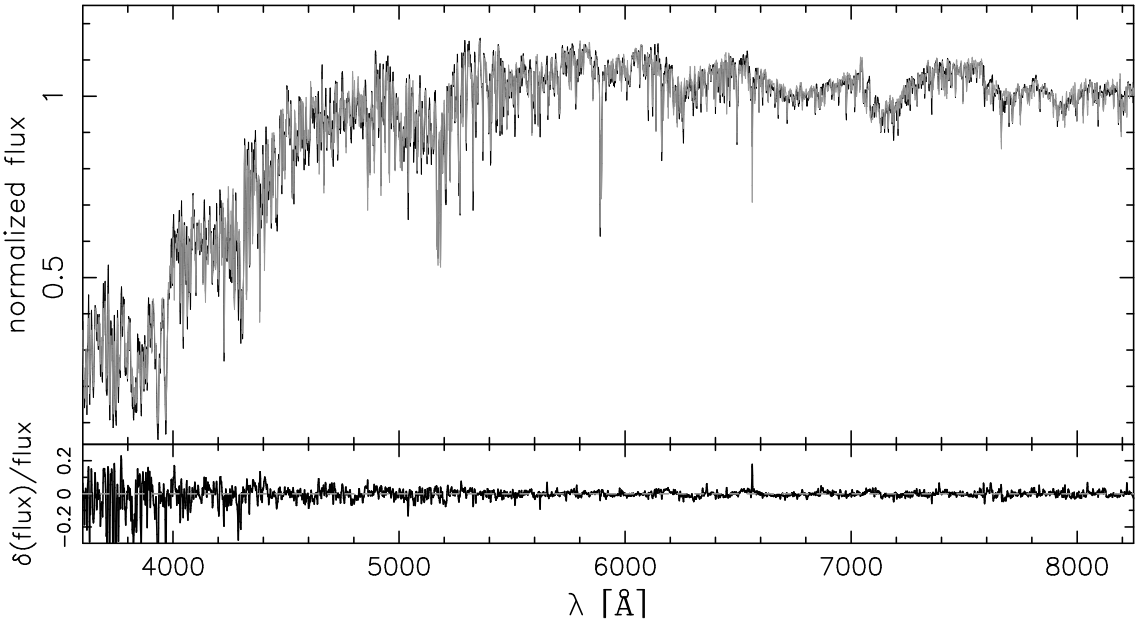

Figure D1. *(Top)* Comparison of one of our simplified, synthetic, SSPs, with solar abundances, to a MILES extended SSP, for an age of 12.5 Gyr, and solar metallicity. The models have been continuum-matched, using a polynomial fitting of order twenty. Both the synthetic and MIUSCAT SSPs correspond to a Kroupa IMF. *(Bottom)* relative residuals, between the synthetic and MILES SSPs.

422, 33
Faber, S.M., French, H.B., 1980, ApJ, 235, 405
Falcón-Barroso, J., Sánchez-Blázquez, P., Vazdekis, A., Ricciardelli, E., Cardiel, N., Cenarro, A. J., Gorgas, J., Peletier, R. F., 2011, A&A, 532, 95
Ferreras, I., Saha, P., Williams, L. L. R., 2005, ApJ, 623, 5
Ferreras, I., Saha, P., Burles, S., 2008, MNRAS, 383, 857
Ferreras, I., Saha, P., Leier, D., Courbin, F., Falco, E. E. 2010, MNRAS, 409, L30
Ferreras, I., La Barbera, F., de la Rosa, I. G., Vazdekis, A., de Carvalho, R. R., Falcón-Barroso, J., Ricciardelli, E., 2013, MNRAS, 429, L15 (FLD13)
Ferré-Mateu, A., Vazdekis, A., de la Rosa, I. G., 2013, MNRAS, in press (arXiv:1301.7066)
Gallazzi, A., et al. 2006, MNRAS, 370, 1106
González, J. J. 1993, Ph.D. thesis, Univ. California
Goudfrooij, P., Kruijssen, J.M.D., 2013, ApJ, 762, 107
Graham, A. W., Guzmán, R., 2003, AJ, 125, 2936
Gustafsson, B., Edvardsson, B., Eriksson, K., Jørgensen, U. G., Nordlund, Å., 2008, A&A, 486, 951
Hardy, E., Couture, J., 1988, ApJ, 325, 29
Hopkins, P., 2013, arXiv:1204.2835
Johansson, J., Thomas, D., Maraston, C., 2012, MNRAS, 421, 1908
Kroupa, P., 2001, MNRAS, 322, 231
Kroupa, P., Weidner, C. 2003, ApJ, 598, 1076
Kurucz, R. L., 1970, SAOR, 309
Kurucz, R. L., Avrett, E. H., 1981, SAOR, 391
Kurucz, R.L., 1992, RMxAA, 23, 45
La Barbera, F., de Carvalho, R. R., de la Rosa, I.G., Lopes, P.A.A., Kohl-Moreira, J.L., Capelato, H.V., 2010a, MNRAS, 408, 1313 (Paper I)
La Barbera, F., de Carvalho, R.R., de la Rosa, I.G., Lopes, P.A.A., 2010, MNRAS, 408, 1335 (Paper II)
La Barbera, F., de Carvalho, R. R., de la Rosa, I.G., Gal, R. R., Swindle, R., Lopes, P.A.A., 2010c, AJ, 140, 1528 (Paper IV)
Larson, R. B., 2005, MNRAS, 359, 211
Lawrence, A., Warren, S.J., Almaini, O., et al. 2007, MNRAS, 379, 1599
Peletier, R.F. et al. 1990, A&A, 233, 62
Prochaska, L. C., Rose, J. A., Schiavon, R. P., 2005, AJ, 130, 2666
Ricciardelli, E., Vazdekis, A., Cenarro, A. J., Falcón-Barroso, J., 2012, MNRAS, 424, 172 (MIUSCAT-II)
Rogers B., Ferreras I., Peletier, R., Silk, J., 2010, MNRAS, 402, 447
Salpeter, E. E. 1955, ApJ, 121, 161
Sánchez-Blázquez, P. et al. 2006, MNRAS, 371, 703
Schiavon, R., Barbuy, B., Rossi, S. C. F., Milone, A., 1997, ApJ, 479, 902
Schiavon, R., Barbuy, B., Rossi, S. C. F., Milone, A., 1997, ApJ, 479, 902
Schiavon, R.P., Faber, S.M., Rose, J. A., Castilho, B. V., 2002, ApJ, 580, 873
Schiavon, R., Caldwell, N., Rose, J. A., 2004, AJ, 127, 1513
Serven, J., Worthey, G., Briley, M. M., 2005, ApJ, 627, 754
Serven, J., Worthey, G., 2010, AJ, 140, 152
Serra, P., Trager, S. C., 2007, MNRAS, 374, 769
Smith, R. J., Lucey, J. R., Carter, D., 2012, MNRAS, 426, 2994
Spiniello, C., Trager, S. C., Koopmans, L. V. E., Chen, Y. P., 2012, ApJ, 753, 32
Spinrad, H., 1962, ApJ, 135, 715
Swindle, R., Gal, R. R., La Barbera, F., de Carvalho, R. R., 2011, AJ, 142, 118S (Paper V)
Thomas D., Maraston C., Bender R., 2003, MNRAS, 339, 897
Thomas D., Maraston C., Bender R., 2003, MNRAS, 343, 279

Thomas D., Maraston C., Korn A., 2004, MNRAS, 351, L19
Thomas, D., et al. 2005, ApJ, 621, 673
Thomas D., Davies R.L., 2006, MNRAS, 366, 510
Thomas, D., Johansson, J., Maraston, C., 2011, MNRAS, 412, 2199
Thomas, D., Maraston, C., Johansson, J., 2011, MNRAS, 412, 2183
Thomas, J., et al., 2011, MNRAS, 415, 545
Trager, S. C., Worthey, G., Faber, S. M., Burstein, D., González, J. J., 1998, ApJS, 116, 1
Tortora, C., La Barbera, F., Napolitano, N. R., de Carvalho, R. R., Romanowsky, A. J., 2012, MNRAS, 425, 577 (Spider V)
Tortora, C., Romanowsky, A.J., Napolitano, N., 2013, ApJ, in press ($arXiv1207.4475T$)
Trager, S. C., Faber, S. M., Worthey, G., González, J. J. 2000, AJ, 120, 165
Treu, T., Auger, M.W., Koopmans, L.V.E., Gavazzi, R., Marshall, P.J., Bolton, A.S., 2010, ApJ, 709, 1195
Trevisan, M., Ferreras, I., de la Rosa, I. G., La Barbera, F., de Carvalho, R. R. 2012, ApJ, 752, L27
van Dokkum, P.G., Conroy, C., 2010, Nature, 468, 940
van Dokkum, P.G., Conroy, C., 2011, ApJ, 735, 13
Vazdekis, A., Casuso, E., Peletier, R.F., Beckman, J.E., 1996, ApJS, 106, 307
Vazdekis, A., Peletier, R.F., Beckman, J.E., Casuso, E., 1997, ApJS, 111, 203
Vazdekis, A., Salaris, M., Arimoto, N., Rose, J.A., 2001, ApJ, 549, 274
Vazdekis, A., Cenarro, A.J., Gorgas, J., Cardiel, N., Peletier, R.F., 2003, MNRAS, 340, 1317
Vazdekis, A., Sánchez-Blázquez, P., Falcón-Barroso, J., et al. 2010, MNRAS, 404, 1639
Vazdekis, A., Ricciardelli, E., Cenarro, A.J., Rivero-González, J.G., Díaz-Garcá, L.A., Falcón-Barroso, J., 2012, MNRAS, 424, 157 (MIUSCAT-I)
Yamada, Y., Arimoto, N., Vazdekis, A., Peletier, R.F., 2006, ApJ, 637, 200
Warren, S. J., Hambly, N. C., Dye, S., et al. 2007, MNRAS, 375, 213
Wegner, G.A., Corsini, E.M., Thomas, J., Saglia, R.P., Bender, R., Pu, S.B., 2012, MNRAS, 144, 78
Wing, R.F., Ford, Jr., W.K., 1969, PASP, 81, 527
Worthey, G., Ingermann, B.A., Serven, J., 2011, ApJ, 729, 148
Worthey, G., 1998, PASP, 110, 888